



**HAL**  
open science

# Graphene produced by chemical vapor deposition : from control and understanding of atomic scale defects to production of macroscale functional devices

Dipankar Kalita

► **To cite this version:**

Dipankar Kalita. Graphene produced by chemical vapor deposition : from control and understanding of atomic scale defects to production of macroscale functional devices. Condensed Matter [cond-mat]. Université Grenoble Alpes, 2015. English. NNT : 2015GREAY098 . tel-01689796

**HAL Id: tel-01689796**

**<https://theses.hal.science/tel-01689796>**

Submitted on 22 Jan 2018

**HAL** is a multi-disciplinary open access archive for the deposit and dissemination of scientific research documents, whether they are published or not. The documents may come from teaching and research institutions in France or abroad, or from public or private research centers.

L'archive ouverte pluridisciplinaire **HAL**, est destinée au dépôt et à la diffusion de documents scientifiques de niveau recherche, publiés ou non, émanant des établissements d'enseignement et de recherche français ou étrangers, des laboratoires publics ou privés.

## THÈSE

Pour obtenir le grade de

### DOCTEUR DE L'UNIVERSITÉ DE GRENOBLE

Spécialité : **Nano-électronique et Nanotechnologies**

Arrêté ministériel : 7 août 2006

Présentée par

**Dipankar KALITA**

Thèse dirigée par **Vincent BOUCHIAT** et  
codirigée par **Nedjma BENDIAB**

préparée au sein du **Département Nanosciences de l'Institut Néel**  
dans **l'École Doctorale de Physique**

## **Graphene produced by Chemical Vapor Deposition: From control and understanding of atomic scale defects to production of macroscale functional devices**

## **Graphène synthétisé par Dépôt Chimique en phase Vapeur: Du contrôle et de la compréhension des défauts à l'échelle atomique jusqu'à la production de dispositifs fonctionnels macroscopiques**

Thèse soutenue publiquement le **25 Juin 2015**  
devant le jury composé de :

**Dr. Erik DUJARDIN**

Directeur de recherche à CEMES, Toulouse

Rapporteur.

**Prof. Eric ANGLARET**

Professeur à Laboratoire Charles Coulomb , Montpellier

Rapporteur.

**Prof. Catherine JOURNET**

Professeur à Université Claude Bernand , Villeurbanne

Examineur.

**Dr. Etienne BUSTARRET**

Directeur de recherche à L'institut Néel, CNRS-Grenoble

Examineur.

**Dr. Nedjma BENDIAB**

Maîtresse de Conférence à UJF, Grenoble

CoDirecteur de thèse.

**Dr. Vincent BOUCHIAT**

Directeur de recherche à l'Institut Néel, CNRS- Grenoble

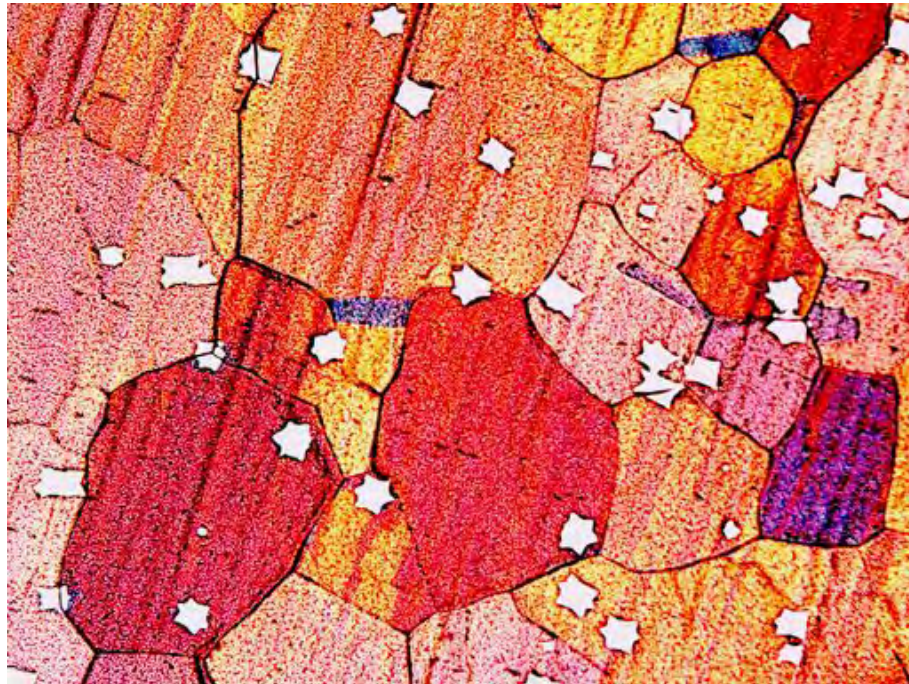
Directeur de thèse.





GRAPHENE PRODUCED BY CHEMICAL  
VAPOR DEPOSITION: FROM CONTROL AND  
UNDERSTANDING OF ATOMIC SCALE  
DEFECTS TO PRODUCTION OF  
MACROSCALE FUNCTIONAL DEVICES

DIPANKAR KALITA



Sacred white graphene crystals on colorful copper grains



## CONTENTS

---

Introduction in English	1
1 Growth of macroscale graphene using CVD method	3
2 Graphene-based heterostructure	4
3 Inducing defects in Graphene	9
1 ENHANCEMENT OF CVD GROWTH ON COPPER FOR OPTIMIZING CRYSTALLINITY AND SIZE	13
1.1 Graphene growth on copper foil and single crystal copper	15
1.2 Pristine graphene structure and vibrational properties	18
1.3 Macroscale polycrystalline graphene growth up to six inches	20
1.4 Growth of large graphene single crystals	23
1.5 Large single crystal growth mechanism	28
1.6 Conclusion	30
2 TRANSFER OF GRAPHENE FOR SUPPERLATTICES AND HETEROSTRUCTURES	31
2.1 Extracting graphene from the copper foil	33
2.2 Graphene stacks by multiple transfer method	34
2.2.1 Fabrication optimization for multilayer transfer	36
2.2.2 Detecting inter-layer interaction using Raman spectroscopy	38
2.2.3 Distinguishing single and poly crystalline graphene	44
2.3 Engineering strain with graphene	47
2.3.1 Strain in self-assembled network of ripples	50
2.3.2 Differentiating strain and doping	55
2.3.3 Dry electrode deposition	57
2.3.4 Other suspended devices	62
2.4 Graphene on insulators	62
2.4.1 Graphene on BN stack	63
2.4.2 Graphene on diamond anvil cells	64
2.4.3 Large area transfer	65
2.5 Graphene as active component	66
2.5.1 Graphene as transparent conducting electrode	66
2.5.2 Graphene as substrate for neuron growth	68
2.6 Graphene on flexible substrate	69
2.7 Comparison with other companies	70
2.8 Conclusion	71

3	CONTROLLING FORMATION OF DEFECTS AND DISCRIMINATING THEIR NATURE IN GRAPHENE BY OPTICAL PHONONS	73
3.1	Chemical control of defects density on graphene	76
3.2	Assessing defect density by Raman spectroscopy	77
3.2.1	Effect of high density of defects on optical phonons	89
3.2.2	Defect study using second-order Raman scattering	91
3.3	Introduction to charged defects	95
3.4	Creating charge defects by CVD growth	98
3.5	Detecting charged defects by Raman spectroscopy	101
3.5.1	Creating structural defects by electron bombardment	105
3.5.2	Wavelength dependence	106
3.5.3	Raman scattering by back-gate doping	107
3.6	Conclusion	108
	Conclusion and Perspectives	111
	Appendix 1: Theory of Raman spectroscopy in graphene	115
	References	123
	Acknowledgments	138

## SYNOPSIS OF THIS THESIS

---

Since the isolation of single sheet of graphite known as "Graphene" in 2004 by Novoselov and Geim [1] by exfoliating graphite using scotch tape, researchers around the world found its amazing properties [2–5]. Graphene has a honeycomb lattice structure of carbon atoms with an highest room temperature electronic mobility of  $120,000 \text{ cm}^2\text{V}^{-1}\text{s}^{-1}$  and near ballistic transport [6–9]. It exhibits exceptional mechanical properties with Young's modulus of 1 TPa and is almost transparent. Hence it has emerged as a strong candidate for application in electronics industry. [10–14]. Today graphene can be produced in large quantities by chemical exfoliation and Chemical Vapor Deposition (CVD) method which can then be transferred to make devices such as pores for DNA sequencing, conducting inks, energy storage and protection against corrosion of steel. [15]

### *questions addressed in this work*

Although highly pure graphene flakes can be exfoliated from graphite, it can not be used for applications due to its small size, irregular shape of flakes and low yield. Chemical Vapor Deposition method has emerged as the alternative to produce graphene in large quantities for various applications. In this method, graphene is grown on metallic surface such as Cu, Pt, Ir etc. Then the graphene can be separated from the metal and transferred to different substrates depending on the application. Previously in our group, we had shown that it was possible to grow perfectly monolayer graphene using a "Pulsed-CVD" technique with minimum defects [16]. However the scale of the graphene growth remained to few centimeters. The challenge was to increase the growth to the wafer scale. In such situations, most often, the solution is to increase the size of the CVD chamber so that a large area copper foil can be inserted. However larger CVD chamber would mean more energy consumption and costly production. Therefore is it possible to possible to grow wafer scale graphene without changing the research scale CVD reactor and with no addition extra energy? We note that the monolayer graphene is poly-crystalline in nature with tens of micrometer size domains whose boundaries increase its sheet resistance. Therefore researchers have tried to grow larger single crystal graphene in millimeter scale but with contrasting methods. In ref [17], Zhou *et al* allowed the inactive  $\text{Cu}_2\text{O}$  to remain on the surface of copper which prevented the precursor gas to come in contact with copper to form nucleation centers. In contrast, Gan *et al*, demonstrated that the nano particles of oxide formed the nucleation centers for graphene growth [18]. Can we confirm one of the theories and give insights to further illustrate the growth mecha-



nism?

Though large area high graphene quality can be grown by CVD method, the graphene needs to be transferred from the metal surface to other substrates to take advantages of its electronic and optical properties. Various methods have been established to transfer graphene such as the liquid transfer method, which is very commonly used to prepare graphene based devices. Recently new interesting physics and applications have emerged for graphene-based heterostructure. Yet very few work has been done to make graphene bilayer stacks using CVD graphene due to difficulty in transferring second layer graphene. Is it possible to identify these problems and modify the liquid transfer method to make macroscopic graphene stacks? The intensity, frequency and FWHM of 2D phonon have been found to vary with rotation angle between two layers of naturally grown bilayer graphene. Is it possible to see the same variation in an artificially transferred bilayer graphene stack? And would the bilayer behave as two individual graphene layers or a single bilayer system? The properties of graphene show a dependency on the target substrate. A way is to keep its properties as intrinsic as possible and change them by a more controlled manner is by fully suspending graphene. Thus ultimate transfer corresponds to making suspended graphene in macroscopic area. Standard transfer methods allow fabricating graphene membranes with few micrometers while damaging the structure during lithography phase. Therefore can we invent a novel method of fabricating large area suspended graphene transistors in tens to hundreds of micrometer square graphene without using complicated fabrication tools? Graphene also has been expected to replace Indium Tin Oxide (ITO) and Au as a material for electrode since it is transparent, flexible and a good conductor. Therefore we attempt use graphene as replacement of Ni/Au electrodes in GaN quantum del LED. The question is what are the advantages of graphene electrode? Finally, using our know-how in transferring graphene, is it possible to transfer graphene on wafer scale substrates?

Graphene is a semi-metal with amazing properties but often these properties need to be modified for certain devices. Therefore it is of utmost importance to deeply understand the effect on its electronic, optical and vibrational properties when we tune parameters such as doping, strain or the structure by inducing defects. In the last part of this work, we will try to explore the possibility of tuning the graphene intrinsic properties by altering its intrinsic structure. Since the electrons and phonons are strongly coupled in graphene, we will use optical phonons as a probe of such fundamental modifications. The exposed surface of graphene allows us to manipulate its atomic structure in order to engineer its properties. Researchers have found that defects induced by different methods such as halogen plasma, electron beam radiation can modify  $sp^2$  honeycomb carbon structure of graphene to change its properties. However all these methods are costly and

restricted to high vacuum technology. Therefore is it possible to develop new methods of inducing defects using chemicals which can be used at much larger industrial scale? What kind of defects are induced by this method and how can we characterize them? In the chemically-induced defect creation method, the destruction of graphene lattice structure also leads to degradation of its unique intrinsic properties. By adsorbing charged defects onto graphene without forming bonds with its structure is another method to engineer its properties. Due to charged nature of the adsorbates, the electronic mobilities of electrons and holes can be separately manipulated. To study the effect of such defects, researchers have externally deposited ions on graphene and studied its electronic and optical properties. However is there another method of intrinsically doping graphene with charged particles? Usually the intensity of  $D'$  band due to charged defects is very low but can it be enhanced? And what is the effect of these defects on the transport properties?

In the following of this introduction, the main results of this thesis will be presented which will be further developed in details in each chapter

## 1 *growth of macroscale graphene using cvd method*

Chemical Vapor Deposition has become the preferred choice of growing graphene and transferring it to different substrates to study its physics and for various applications. However growth by standard method results in multilayer graphene patches due to surface contamination and point defects in metal foils. Therefore a novel method was developed in our group to grow monolayer graphene by "Pulsed-CVD" method. In this method, the carbon precursor gas ( $\text{CH}_4$ ) was injected into the growth chamber intermittently. The duration of injection ( $t_1$ ) and stop time ( $t_2$ ) was adjusted in such a way that multilayer patches were removed leaving only a monolayer graphene. [16]

Though monolayer graphene had become possible to grow, it was necessary to scale-up in order to increase graphene production. It could be done by increasing the size of the furnace or by increasing the area of copper foil inside the present chamber. In this work, we show how we managed to increase the area of copper foil by rolling it as shown in figure 0.1(a). The spacers are introduced in order to avoid surfaces touching each other. This way we managed to increase the area of CVD graphene from 40 to 300  $\text{cm}^2$  as shown in figure 0.1(c). The novelty of this approach is that energy needed to produce large area graphene is same as that of small one as we have not increased the volume of the chamber.

The monolayer graphene is polycrystalline in nature with micrometer size domains. During the growth, there are numerous nucleation sites where patches of graphene start

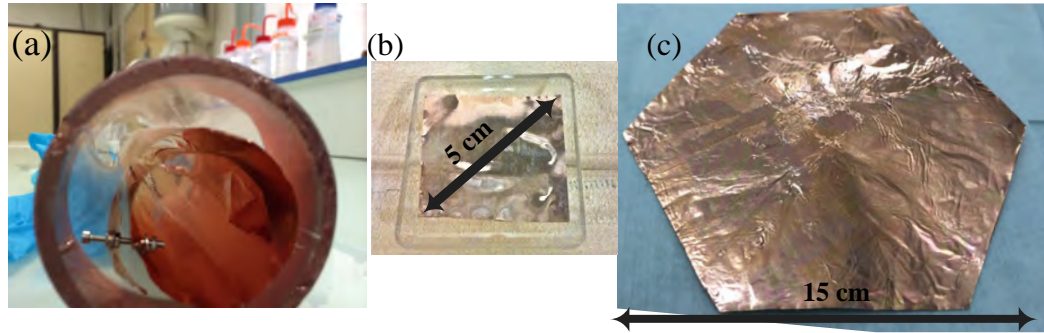


Figure 0.1: Macroscale continuous polycrystalline monolayer graphene. (a) Photo of copper foil in the form of spiral in a quartz tube with nuts and bolts which act as spacers to hold the structure at high temperature. Size of graphene grown on copper foil in (b) first generation (c) second (present) generation.

to grow. With the growth time, they percolate and form a single layer. The boundaries between two grains are made of pentagons and heptagons where the carbon-carbon bonds are strained. When such graphene is suspended, they break along the boundaries. Moreover it was demonstrated that the sheet resistance of the graphene increases if electrons are made to pass through increasing number of grain boundaries by Cummings *et al* in [19]. Hence it becomes necessary to understand the nucleation process in order to increase the size of individual grain. Besides the single crystal graphene would bring uniformity to the device properties.

In order to understand nucleation process, the role of thickness of  $\text{Cu}_2\text{O}$  layer that forms on copper surface and role of partial pressures are studied. We found that the nucleation density of graphene decreases as we increase the thickness of  $\text{Cu}_2\text{O}$  layer by heating the copper foil in ambient atmosphere. The oxide surface prevents the dissolution of carbon on copper surface which leads decrease in nucleation centers. By diluting the carbon precursor  $\text{CH}_4$  in Ar gas, decreasing the flow rate of  $\text{H}_2$  gas and increasing pressure of chamber, the nucleation density was further decreased. This allowed us to grow single crystal as large as  $300\ \mu\text{m}$  as shown figure 0.2(b).

Thus we managed to scale-up the growth of monolayer polycrystalline graphene upto wafer scale and increase the size of single crystal graphene to  $300\ \mu\text{m}$ .

## 2 graphene-based heterostructure

After growing graphene in copper foils, it needs to be transferred to different kinds of substrates to fabricate devices. Various methods have been developed to transfer

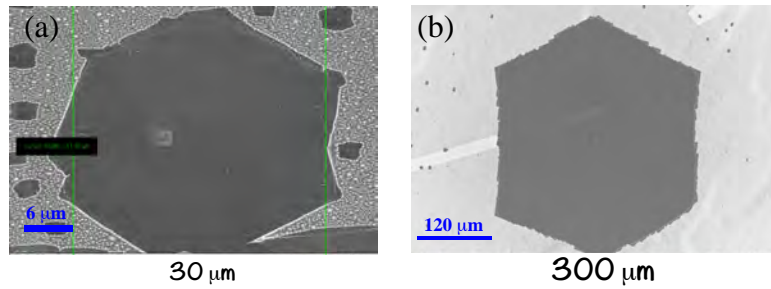


Figure 0.2: Large graphene single crystals. SEM images of graphene grown on Cu (a) at low pressure and pure  $\text{CH}_4$  (size  $30\ \mu\text{m}$ ) (b) at high pressure and diluted  $\text{CH}_4$ . (size  $300\ \mu\text{m}$ )

graphene such as liquid-assisted transfer, dry transfer with thermal tape, electrochemical separation of graphene from metal foil, roll-to-roll process for industrial application etc. We have optimized liquid transfer method to make our devices. Recently graphene heterostructures such as bilayer graphene has found its importance due to presence of tunable bandgap. With modifications to the liquid-assisted transfer method, we have been able to fabricate crossbars using two monolayer graphene ribbons as shown in figure 0.3(a). The method also has been used to make artificial bilayer of hexagonal and octagonal shaped graphene shown in figure 0.3(b).

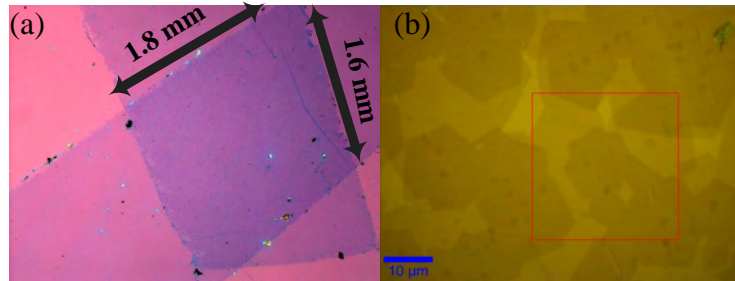


Figure 0.3: Artificial bilayer graphene. (a) Macroscopic graphene crossbar fabricated from monolayer graphene ribbons. (b) Two layers of hexagonal and octagonal crystals of graphene transferred onto each other.

Raman spectroscopy has been used to verify the interaction between the two layers of transferred graphene. Researchers have found that the electronic band structure of bilayer graphene changes depending on the rotational angle between the two layers. This in turn affects the electron-phonon coupling conditions. Since the electron and phonons are strongly coupled in graphene, intensity, position and FWHM of the Raman peaks

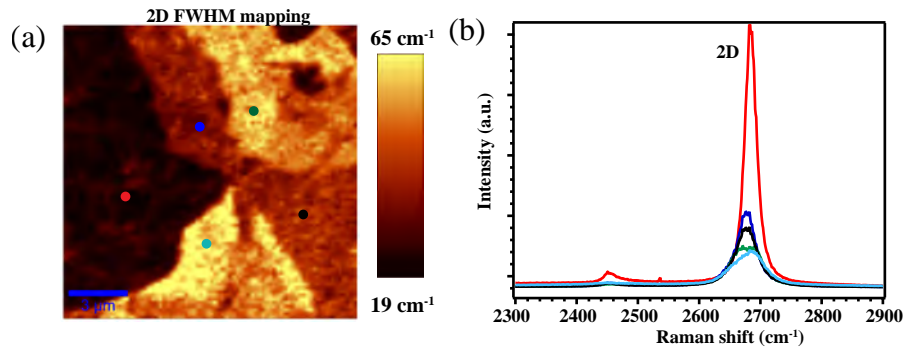


Figure 0.4: Raman characterization of bilayer graphene. (a) 2D FWHM mapping of bilayer graphene. (b) 2D Raman spectra of different grains of bilayer graphene as shown in (a).

of graphene are affected by the rotation angle. In the figure 0.4(a), we observe different grains in 2D FWHM mapping of bilayer depending on the rotation between graphene layers. The spectra corresponding to different grains are shown in figure 0.4(b). It can be observed that the shape, FWHM and intensity of 2D peak varies with grain. Such informations have been used to classify the angles of rotation in our bilayer graphene.

A direct application of this technique is to find the crystallinity of hexagonal and octagonal graphene crystals at macroscopic scale. When the hexagonal graphene crystals were transferred on top of each other, we found that the Raman signal from 2D intensity and FWHM remained homogenous in the bilayer region as shown in the figure 0.5(a) and (b) respectively. This proved the single crystallinity of hexagonal graphene. Thereafter octagonal graphene crystals were transferred on hexagonal graphene crystals to find the different grains and their orientation as shown in schematic in figure 0.5(b). It was observed that the octagonal crystals were polycrystalline in nature unlike the hexagonal crystals.

To take advantage of its intrinsic properties, graphene needs to be suspended. Such structures have the potential for being used as sensors. However the present day fabrication of suspended devices require electron beam to pass through graphene which affects its intrinsic properties. Moreover these suspended devices are found to be strained. In this subsection, we discuss a novel method of suspending graphene by transferring it on pillared substrates. We have found that as the distance between pillars become closer than a critical distance, graphene remains fully suspended over a macroscopic scale as shown in figure 0.6(a) and (b). Raman spectra from the different regions in (a) are shown in figure 0.6(c). It was found that the strain in fully suspended graphene was as low as 0.2%.

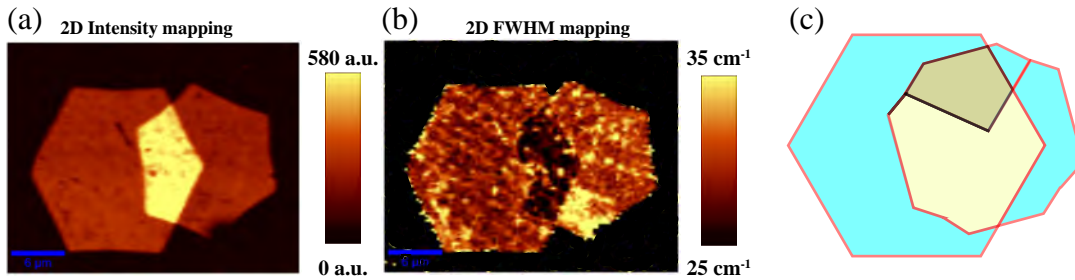


Figure 0.5: Raman mappings of stacked graphene crystals. (a) 2D intensity (b) 2D FWHM mapping of hexagonal single crystal graphene respectively. (c) Schematic showing hexagonal, octagonal shaped graphene crystals when they are transferred on top of each other. The blue color indicates Raman signal from single layer graphene while brown and orange indicate different Raman signal due to different rotation of the top and bottom layer caused by the polycrystalline octagonal shaped graphene.

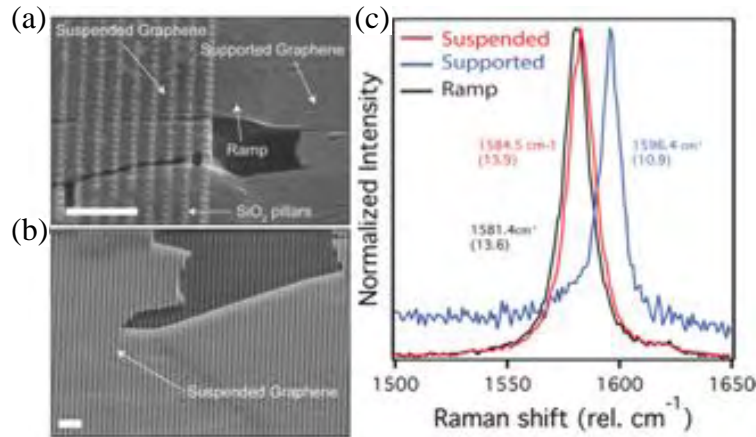


Figure 0.6: Fully suspended graphene fakir carpets. (a) and (b) SEM micrograph of fully suspended graphene on pillars with distance between pillars "a" = 250 nm (Scale bars represent 1  $\mu\text{m}$ ). In (a) we also observe supported graphene on flat  $\text{SiO}_2$ , ramp of graphene at the boundary and tears in graphene when it is suspended. (c) Raman spectra of graphene at suspended, supported and ramp portion in (a).

Since graphene is fully suspended on pillars, we cannot use classical lithography techniques as liquid resist would go below the graphene and remove it. Hence a novel dry lithography technique was developed using a transparent, flexible parylene stencil mask. Holes in the shape of electrodes were etched in the mask and aligned over specific graphene flake. Thereafter metals were shadow deposited which was followed by dry

lift-off of the mask as shown in figure 0.7(a). The electrodes deposited on the pillared surface are shown in figure 0.7(b).

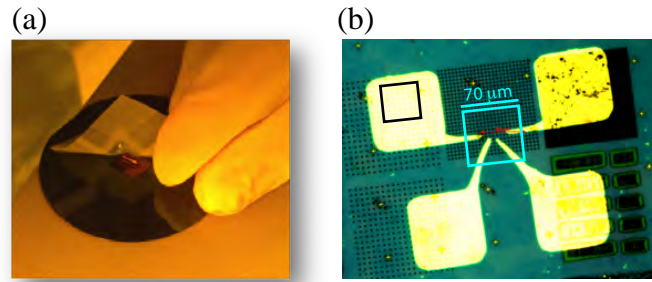


Figure 0.7: Parylene stencil mask. (a) Dry lift-off process after deposition of electrodes. (b) Optical image of four electrodes deposited over graphene on corrugated substrate.

Using our expertise in graphene transfer, we have used graphene as the transparent capping electrode in GaN quantum well LED. In this case, multiple layers of graphene were transferred to replace the Au electrodes. The Au electrodes are opaque and do not transfer charges over a large area. Since graphene is transparent, light is able to pass through it and at the same time illuminate a larger area. An example of such a device can be seen in figure 0.8(a).



Figure 0.8: Graphene for device applications. (a) Photo of a working GaN quantum well LED with graphene electrode. (b) Graphene transferred on 2, 3 and 4 inches Si/SiO<sub>2</sub> wafer. (c) Centimeter scale polymer-graphene transparent membrane.

The transfer technique was also scaled-up to deposit graphene in 2, 3 and 4 inch wafers as shown in figure 0.8(b) which may find application in the electronic industry. And finally graphene was transferred to flexible, transparent substrate as shown in figure 0.8(c): the process of fabrication is being patented.

## 3 inducing defects in graphene

Modifying structure of graphene and its properties is paramount in order to fabricate graphene-based devices such as super capacitors, spintronics. There are already developed methods to modify the  $sp^2$  carbon-carbon lattice structure to  $sp^3$  such as bonding halogens atoms using plasma, electron beam radiation and  $Ar^+$  ion bombardment. In this subsection, we show a chemical method of inducing defects in graphene. Very often chemicals such as  $Na_2(SO_4)_2$  are used for etching the copper foil before transferring graphene onto other substrates. However, we found that  $Na_2(SO_4)_2$  starts etching graphene once it comes in contact with it. Here we have developed a protocol in order to control the defects in graphene with etching time as shown in figure 0.9(a). It can be observed the area and intensity of D band, which represents the defects, initially increases with time and reaches a saturation after 14 hours of etching figure 0.9(b).

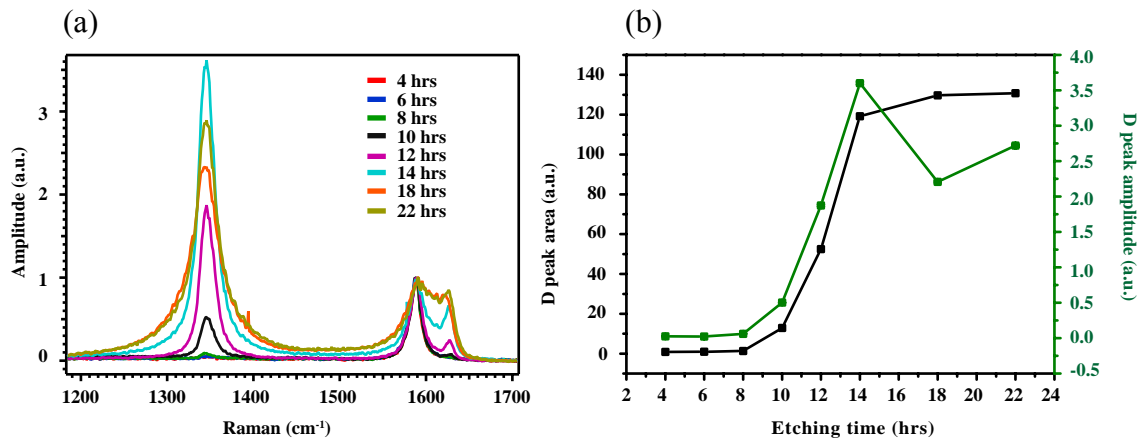


Figure 0.9: Chemical action on graphene. (a) Raman spectra of graphene after treatment with  $Na_2(SO_4)_2$ . (b) Evolution of area and amplitude of D peak with time of etching

Using the intensity ratio of D and G band ( $I_D/I_G$ ), we found that the defects induced by the chemical mechanism is close to substitution defects as shown in figure 0.10(a). But in our case, the TEM images before and after etching the graphene for 15 hours did not show any structural difference as shown in figure 0.10(b) besides we reached an unexpected saturation of intensity and area of D band. Based on these observations, we propose a mechanism of etching graphene by  $Na_2(SO_4)_2$ . Firstly the small molecules such as hydrogen are grafted on graphene surface which increases intensity of defect bands rapidly. This intensity is expected to decrease once it reaches its maximum value as further bonding of hydrogen atoms would destroy the lattice structure of graphene. However in our case, the hydrogen bonds reaches a saturation limit beyond which the



reactions does not have enough energy to graft more bonds. Therefore the intensity of hydrogen bonds remain constant and honeycomb lattice is not destroyed but the ratio of  $sp^3/sp^2$  increases.

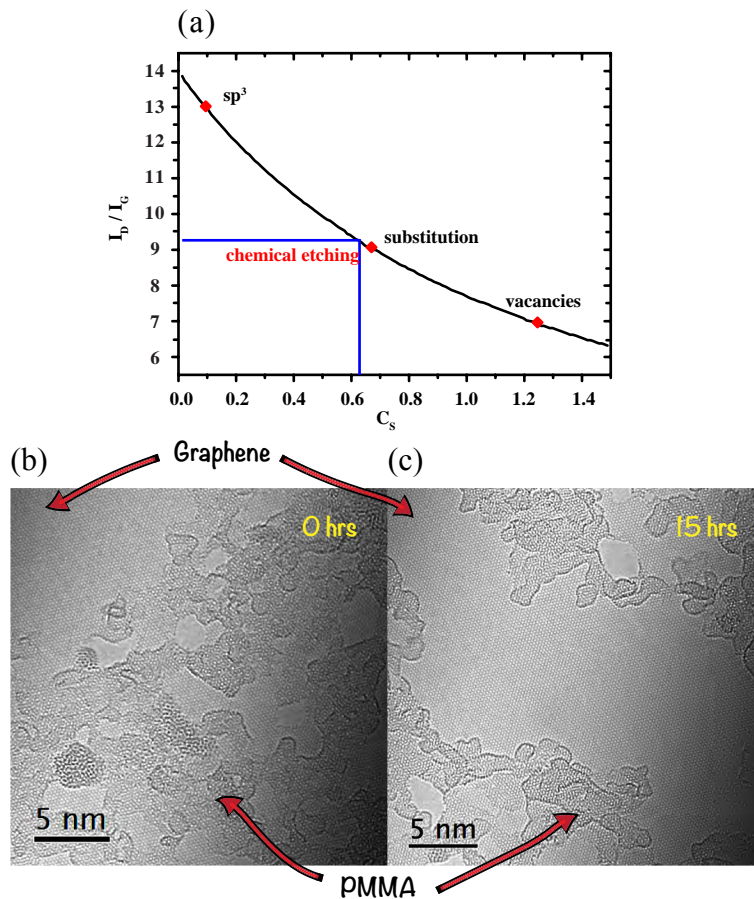


Figure 0.10: (a) Classification of defects created by etching process using  $I_D/I_G$ . TEM image of graphene after (b) 0 hr (c) 15 hr of etching.

We must note that inducing defects using chemical method destroys carbon-carbon  $sp^2$  lattice structure which leads to degradation of its unique intrinsic properties. However there is another method of manipulating properties of graphene by adsorbing charged defects onto graphene without forming bonds. Controlled external deposition of charged defects have shown to effect electronic properties of graphene. In this subsection we demonstrate a intrinsic method to fabricate the charged defects during the growth process. This is possible due to the surface contamination of the copper foil by Cr/CrO<sub>2</sub>.

Growth of graphene on such surface gives rise to previously unseen anomalously high intensity D' band which represents charged defects. The black curve in figure 0.11(a) shows the Raman spectrum from such graphene. If the layer of Cr/CrO<sub>2</sub> is removed by hydrogen annealing or is absent in uncoated copper foil, the D' band is absent. The effect of charged defects on the electronic property of graphene can be observed in figure 0.11(b) where the asymmetry in mobility between electrons and holes are visible.

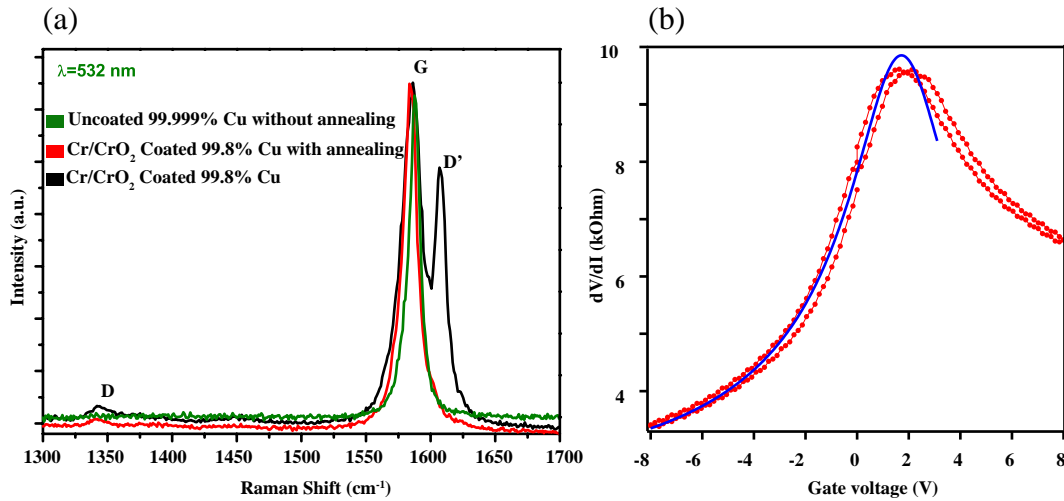


Figure 0.11: Properties of charged defects in graphene. (a) Comparison of Micro-Raman spectra of graphene grown on different copper foils. (b) Resistance measurement versus backgate voltage of charged induced graphene. The blue curve is a fit which gives the mobility of holes to be  $\approx 1500 \text{ cm}^2\text{V}^{-1}\text{s}^{-1}$  (Transport measurement by Mira BARAKET, postdoc, Institute Néel)

From these main results, the outline of this thesis will be the following.

Chapter 1 presents the contribution about the macro scale graphene production and enhancement of the crystallinity by CVD on copper. Chapter 2 focusses on graphene to perform tuning its properties such as strain, bandgap and mobility. In chapter 3, optical phonons are used as a highly sensitive probe to discriminate structural defects from charged defects.



## ENHANCEMENT OF CVD GROWTH ON COPPER FOR OPTIMIZING CRYSTALLINITY AND SIZE

---

Though stable monolayered crystals do not exist naturally, it was shown that it can be produced by exfoliating bulk graphite [1]. Graphite is made of stacks of atomically thin carbon monolayers bound together by a weak Van der Waals force. Therefore it is possible to mechanically separate the layers till a single layer remains. This was done mechanically by using scotch and finally depositing the last layers on flat solid substrate. Surprisingly the quality of graphene is very high with few defects but the efficiency of producing graphene using this technique is very low and hence its utility remained for research purposes only.

Therefore a new technique was developed to produce graphene in large quantities using "Chemical Vapor Deposition" CVD method. It is a process involving a vapor phase carbon source like  $\text{CH}_4$  that is decomposed to solid phase  $\text{sp}^2$  carbon i.e. graphene. This phase transformation takes place with the help of a catalytic surface. The carbon atoms from the gas precursor adsorbed onto the catalytic surface after being dissociated from the hydrogen atoms at high temperature. The carbon atoms are highly mobile on the surface of the catalytic surface at high temperature and unbound from the catalytic surface once they start to form  $\text{sp}^2$  bonds with other carbon atoms and nucleate to form energetically favorable honeycomb lattice structure.

The catalytic surface needed to dissolve the carbon is usually a metal surface. Solubility of carbon in the metal plays an important role in choosing the metal foil. A metal with higher solubility will not only adsorb carbon atoms on its surface but also diffuse them into its bulk material. The surface carbon atoms will nucleate to form graphene. At the same time the carbon atoms dissolved in the bulk material will segregate to the surface and nucleate to form the second/multiple layers of graphene.

Therefore a metal must be chosen such that carbon solubility is low enough so that the carbon atoms remain on the surface and do not diffuse into the bulk. As it can be observed in figure 1.1, the solubility of carbon can vary from  $10^{-4}$  to  $10^{-2}$  for different metals and copper seems to have the lowest solubility after  $1000^\circ\text{C}$ . This makes copper a good candidate to grow graphene. Indeed a lot of progress has been made in the growth of graphene since it was first demonstrated by Li *et al* [21]. Today it is possible to make 30 inches wide continuous graphene on copper layers and transfer them on flexible substrates using industrial roll-to-roll process [22]. The same method was extended by Sony corporation to make 100m long graphene on plastic [23].

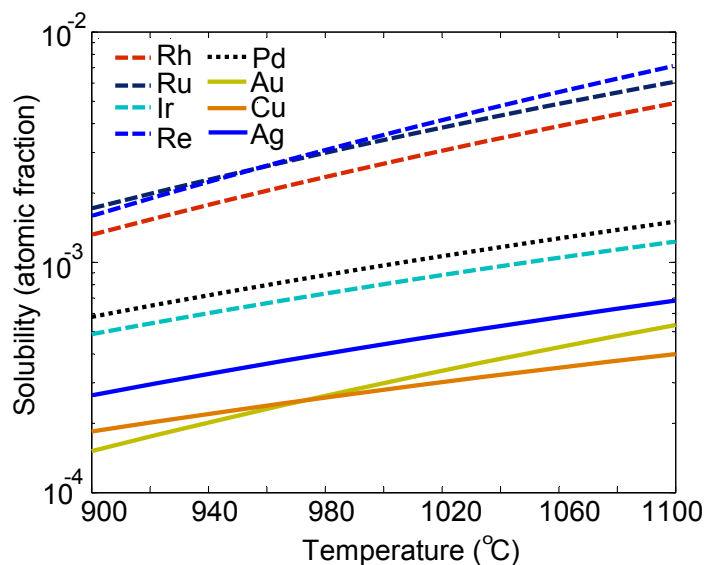


Figure 1.1: Carbon solubility curve of different metals with temperature. Copper has the lowest solubility after 1000°C. Adapted from [20]

However most of the graphene that is produced by standard CVD method on copper are not perfect and are plagued with two important problems as follows.

1. Firstly, graphene produced is not strictly monolayer and contains multilayer patches. This is because the copper foils which are generally used to grow graphene has lot of point defects in the manufacturing process which allows trapping of carbon atoms into its bulk material. These carbon atoms then segregate to form multilayers. This problem was addressed by Zheng Han during his PhD thesis and led to a variant of the main process that will be explained below. In this thesis, we will go beyond and show how monolayer graphene can be grown in large scale in a lab-scale CVD reactor without multilayer patches.
2. Secondly, the graphene grown by CVD method is not single crystal but results from an agglomeration of tens of micron-sized crystals percolating to form a mosaic-like polycrystalline monolayer graphene. The graphene grain boundaries are found to be detrimental to the electron transport [24]. Therefore it has become essential to understand the nucleation process in order to grow large crystal graphene. A study into the growth of large crystals is demonstrated in following subsections.

## 1.1 GRAPHENE GROWTH ON COPPER FOIL AND SINGLE CRYSTAL COPPER

Here we describe the growth process that was developed to obtain graphene on a copper catalytic surface. A schematic diagram of home-made CVD system is shown in figure 1.2(a). The precursor gasses used in the growth are Ar, CH<sub>4</sub> and H<sub>2</sub> which are injected into the quartz tube using a series of Mass Flow Controller (MFC). The variable speed pump is used to remove gas from the quartz tube before the growth and control the overall pressure during the growth process. The quartz tube can be heated up to 1100°C. The speed of the pumps, flow of gases and temperature of the oven are controlled by Labview software developed by Zheng Han during his PhD thesis.

An optical image of the quartz tube is shown in figure 1.2(b). The diameter of the tube is around 10 cm. A quartz plate with size 40 cm<sup>2</sup> with a copper foil is inserted into the heating zone of the tube. A typical copper foil of 5 cm square diagonal is used to grow graphene in it.

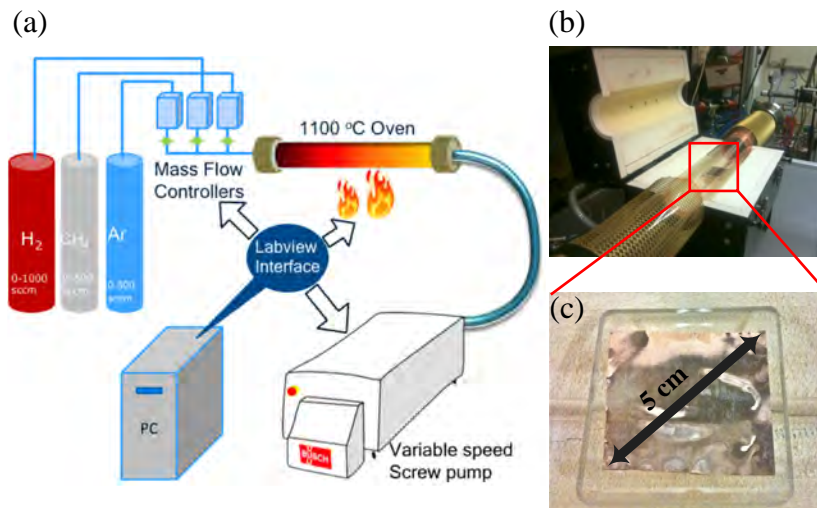


Figure 1.2: Graphene production using CVD technique. (a) Schematic of CVD graphene growth setup. (b) Photo of CVD machine. (c) Zoomed image of first generation quartz plate with copper foil. (Figures adopted from PhD thesis of Zheng HAN, Institut Néel)

A schematic of the standard process flow of graphene growth is shown in figure 1.3(a) with time scale. The temperature of the oven increases from room temperature (RT) to 1000°C during we inject 100 sccm (standard cubic centimeter) of Ar and 50 sccm of H<sub>2</sub> for 60 minutes which cleans most of surface contamination from copper foil. For the growth, 2 sccm of CH<sub>4</sub> is injected for a duration which depends on the intended coverage. Typically it takes 15 minutes for the cull coverage of the copper foil. After

the growth, the  $\text{CH}_4$  and  $\text{H}_2$  are immediately stopped and temperature is brought down to RT in 500 sccm of Ar environment. Table 1 gives the growth parameters of standard growth of graphene.

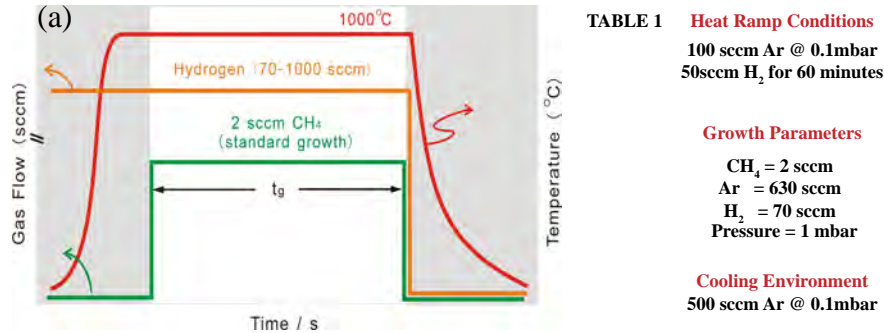


Figure 1.3: Conditions for standard growth of graphene. (a) Process flow of standard growth of graphene on copper explaining the flow of gases and temperature variation with time. Table 1 gives the growth parameters for standard growth. (Figures adopted from PhD thesis of Zheng HAN, Institut Néel)

Figure 1.4(a) shows a optical image of graphene after it has been transferred onto Si/SiO<sub>2</sub> substrate. Graphene is present everywhere while the darker patches are the multilayer graphene. They are mostly aligned along the foil scratches resulting from the lamination process. These patches are detrimental to the electron transport as explained by Han *et al* in ref [16]. In order to understand this phenomenon, electrodes were fabricated across a monolayer and multilayer patch as shown in figure 1.4(b). The multilayer graphene patch is pointed out by a black arrow. It can be observed in figure 1.4(c) that the field effect curve probing the multilayer patch is distorted and asymmetric due to scattering from the edges of multilayer graphene.

To remove the multilayer patches from graphene, a novel method was developed whereby the continuous injection of  $\text{CH}_4$  was replaced by intermittent injection of the precursor gas as mentioned in ref [16]. In this process,  $\text{CH}_4$  is injected at 5 sccm for  $t_1 = 10$  sec and stopped for  $t_2 = 50$  sec. During injection period, the carbon atoms get adsorbed on the surface as well as trapped into the point defects as shown in figure 1.5(b). But during the idle time  $t_2$ , the hydrogen etches all of the carbon atoms from the point defects since they are not bonded. During this time, not all of the carbon atoms from surface are removed as they are more stable due to  $\text{sp}^2$  bonding with each other though the edges are smoothed due to etching.

The result of the pulsed growth can be seen in the figure 1.6. In figure 1.6(a), graphene is grown using standard growth. The image has three contrast. The flower like shape is the monolayer graphene with a darker contrast showing the multilayer patch.

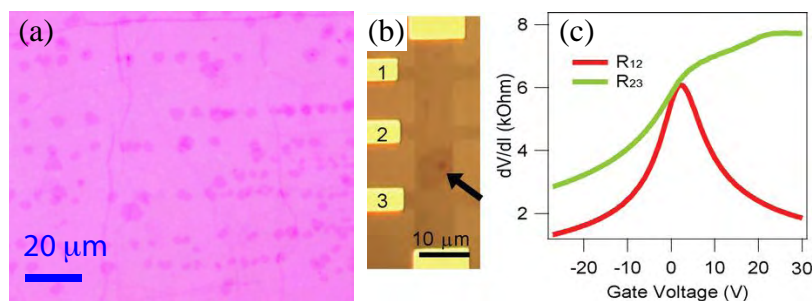


Figure 1.4: Standard CVD graphene and its transport properties. (a) Optical image of graphene after transferred on Si/SiO<sub>2</sub> substrate. The darker spots are multilayer patches. (b) Optical image of a Hall bar made from graphene. There is monolayer graphene between 1-2 electrodes and multilayer patch graphene between 2-3 electrodes. (c) Differential resistance measurement between 1-2 electrodes with monolayer and 2-3 electrodes with multilayer patches. (Figures adopted from PhD thesis of Zheng HAN, Institut Néel)

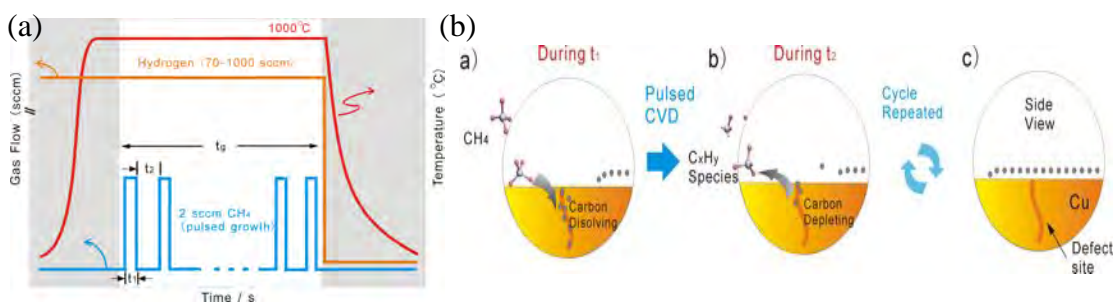


Figure 1.5: Pulsed growth of monolayer graphene. (a) Schematic of Pulsed growth explaining the flow of gasses and temperature variation with time. (b) Mechanism of monolayer graphene formation during pulsed growth. (Figures adopted from PhD thesis of Zheng HAN, Institut Néel)

In figure 1.6(b), there is no multilayer graphene at the center graphene grains which has been etched due to pulsed growth though their etches are rounded due to hydrogen activity. The individual patches percolate to form a monolayer graphene as they grow larger with growth time.

Till now we have described the growth of graphene by CVD method but we need to characterize its structure and quality. Detailed characterization is presented in the next section using various techniques.



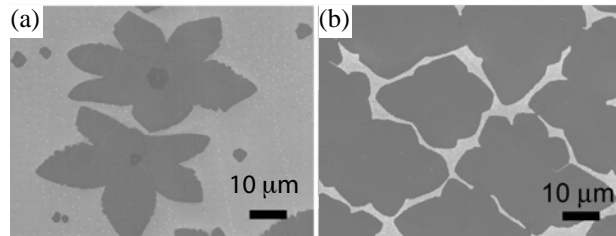


Figure 1.6: SEM image of (a) standard and (b) pulsed growth of flower shaped graphene flakes. Note: the more rounded shape for pulsed growth is due to hydrogen activity.

## 1.2 PRISTINE GRAPHENE STRUCTURE AND VIBRATIONAL PROPERTIES

In order to get a complete picture of our CVD graphene, we have used complementary techniques such as Raman spectroscopy, AFM, STM.

One of the most utilized method to check the quality of graphene in a fast and non-invasive way is by using Raman spectroscopy. In figure 1.7(a), we show a typical Raman spectrum of graphene on copper. The high intensity of G and 2D bands represent the high quality of graphene along with the negligible defect-assisted D band. The center and FWHM of G peak are  $1583.5$  and  $13 \text{ cm}^{-1}$  respectively while center and FWHM of 2D peak are  $2651$  and  $21.5 \text{ cm}^{-1}$  respectively. More details about Raman spectroscopy on graphene will be shown in annex where we give brief overview about the theory on Double Resonance (DR) Raman spectroscopy. Intuitively, Raman cross-section from one layer of atoms should be very low compared to reflected/transmitted light from it. However the resonance conditions in graphene are always fulfilled for any wavelength due to its unique electronic band structure. This effect enhances the intensity of graphene Raman peaks, hence we are able to observe even the second order peaks such as 2D in graphene despite being a single layer of carbon atoms.

Figure 1.7(c) shows the Atomic Force Microscopy (AFM) image of graphene grown on copper foil immediately after the growth. The lines across the graphene are atomic copper steps on which graphene has grown conformally. The fact that these lines are visible shows a clean surface on graphene after the growth.

Another way to observe the quality of graphene at atomic resolution is by scanning individual carbon atoms for presence of defects. This is done by Scanning Tunneling Microscope (STM). This technique has been used to atomically map the honeycomb  $sp^2$  structure of graphene [24]. We had performed a standard growth of graphene on Cu(100) single crystal. Cu(100) has square lattice structure ( $a_{\text{Cu}} = 2.56 \text{ \AA}$ ) and is represented by red balls in figure 1.8(a) while graphene with honeycomb lattice structure ( $a_{\text{Gr}} = 2.46 \text{ \AA}$ ) is represented by black balls. Since their lattice constants ( $a$ ) do not match, they give rise

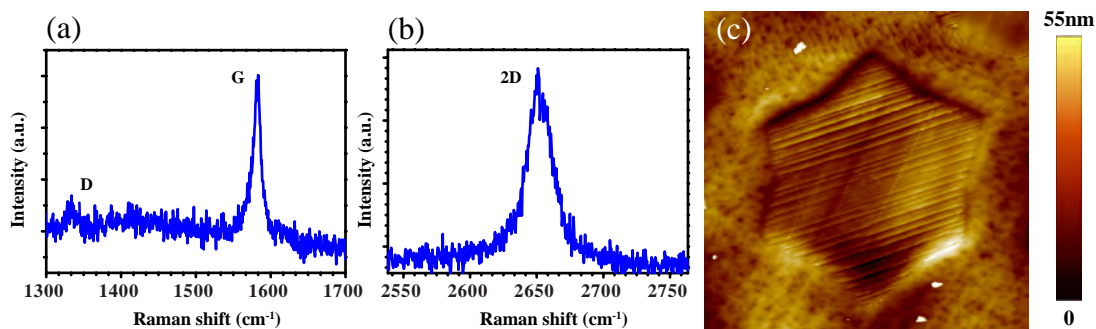


Figure 1.7: Characterization of graphene. Typical Raman spectrum of graphene on copper (a) G peak (b) 2D peak. (c) AFM image of graphene on copper just after growth. Copper terraces are clearly visible below the graphene flakes. (Figure by Laëticia MARTY)

to a moiré pattern due to 2-D spatial interference between the periodicity of the stacked crystals. A STM image of monolayer graphene on Cu(100) can be seen in figure 1.8(b). In this case the moiré pattern that arises shows 1-D lines with a pitch of around 1.2 nm with a preferential direction of  $5-7^\circ$ . The inset shows the zoomed image of the moiré pattern and also the atomic resolution of honeycomb carbon structure of the graphene.

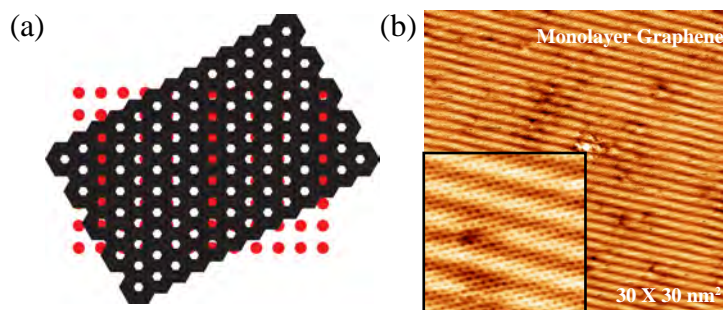


Figure 1.8: 2-D spatial interference of graphene on Cu(100). (a) Schematic of graphene (black balls) grown on Cu(100) (red balls) surface of cubic symmetry giving rise to 1-D moiré patterns. (b) STM image of graphene on Cu(100). The lines are moiré patterns with a pitch of 1.2 nm and angle of  $5-7^\circ$ . (Image courtesy from collaborators: Vladimir CERCHEZ, Jean-Yves VEUILLEN, Pierre MALLET, Institut Néel)

The standard growth of graphene produced multilayer patches which are pointed by green arrows in the SEM image in figure 1.9(a). They can also be detected by STM where we can distinguish between monolayer and bilayer graphene at nano scale as shown in figure 1.9(b). A zoomed image on the bilayer reveals the moiré pattern in the form of

triangular lattice with a pitch of 2.1 nm. This value was found to correspond to an angle of  $6.5^\circ$  between the two layers of graphene. The inset in (b) shows the atomic resolution of the moiré along with the honeycomb structure of top graphene layer.

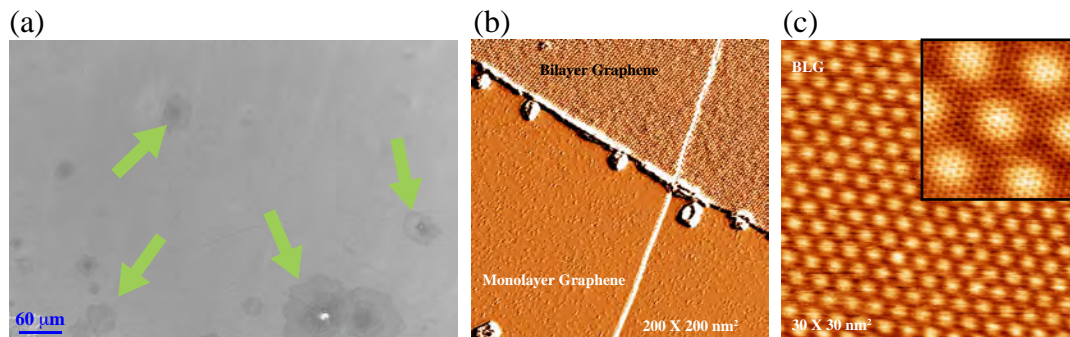


Figure 1.9: 2-D spatial interference of bilayer graphene (a) SEM image of standard growth of graphene on Cu(100). The green arrows point towards multilayer patches. (b) STM image of a boundary between monolayer and bilayer graphene. (c) Zoomed STM image of bilayer graphene showing the triangular lattice moiré pattern. Inset shows the atomically resolved moiré pattern of bilayer graphene. The atomic honeycomb structure of top layer of graphene is also visible. (Image courtesy from collaborators: Vladimir CERCHEZ, Jean-Yves VEUILLEN, Pierre MALLET, Institut Néel)

From the above characterizations of CVD graphene, we can claim that the quality of graphene is high due to the negligible presence of defects in the lattice structure from the atomic to macroscopic scale. Defects could be present at larger scale which is not possible to scan using STM. However such defects can be detected using Raman spectroscopy. In the last chapter, we show how different types of defects can be induced and detected using Raman spectroscopy.

Next section addresses whether it is possible to upscale the growth of this high quality graphene.

### 1.3 MACROSCALE POLYCRYSTALLINE GRAPHENE GROWTH UP TO SIX INCHES

Although we were able to produce continuous growth of monolayer graphene in the first generation, the challenge was to produce it in largest area possible in a research scale CVD setup. One way to scale-up growth is to increase the area of the CVD chamber. However it is costly proposition and energy needed to reach  $1000^\circ\text{C}$  in larger chamber is much more. We chose a different route to achieve the target. Though the diameter of the quartz tube where the copper foil is inserted is restricted to 10 cm, we found that the copper foil need not be flat, provided no sharp fold is created that might lead to tearing

of graphene during unfolding. As it can be seen in figure 1.10(a), the copper foil can also be rolled. This way, we are able to increase the width of the foil on which the graphene can be grown from few centimeters to 20 cm X 20 cm. The width being defined by the oven temperature homogeneity. Although the melting point of copper is around  $1085^{\circ}\text{C}$ , it is found that the copper foil easily sticks to each other at around  $1000^{\circ}\text{C}$ , which is prevented by the nuts and bolts attached to foil which prevents the foil to roll and fall on each other. This method also enables us to unroll the foil easily after the growth. The length of the foil is kept at 20 cm as seen in figure 1.10(b).

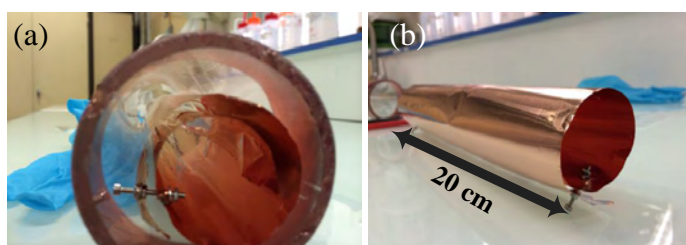


Figure 1.10: Large area graphene production. (a) Copper foil in the form of spiral in a quartz tube with nuts and bolts which act as spacers to hold the structure at high temperature. (b) Side-view of copper foil with length of 20 cm.

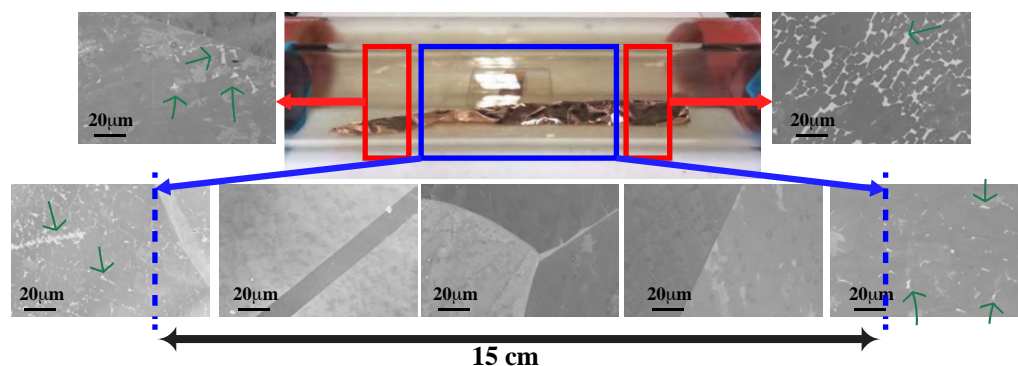


Figure 1.11: SEM mapping showing graphene homogeneity. At the center is the optical image of the CVD oven with a rectangular copper foil at the bottom. The blue square indicates the width of heating region where the temperature is maintained at maximum but the temperature falls off exponentially at the red zones. The graphene corresponding to the blue zone (within the blue dashed lines) are continuous while the graphene corresponding to red zone is discontinuous. Within the blue zone, different contrast are visible in SEM images due to different grains of copper. The green arrows point towards discontinuous graphene

In our CVD system, the width of heating zone is restricted to 12 cm in length. At this zone, growth of graphene is expected to be continuous due to maximum temperature but outside this zone the temperature falls off exponentially at the red zones. However the continuity of the graphene growth can be increased by increasing the growth temperature to  $1030^{\circ}\text{C}$ , thereby increasing the temperature of the copper foil outside in the red zones. Besides we also increased the time of growth. So the time injection of  $\text{CH}_4$  was increased to 1 hr compared to 15 mins for short copper foil. It can be seen in figure 1.11 the width of heating region is marked by blue rectangle. The SEM images of graphene corresponding to this zone is shown below it. Within the blue dashed lines, the graphene is continuous. The different contrast in these SEM images are different copper grains below the graphene. Outside this zone, marked by the red rectangles, graphene is not fully continuous. The absence of graphene is pointed out by green arrows.

This is a novel way to produce second generation of large area of graphene ( $300\text{ cm}^2$ ) in the CVD chamber since the amount of energy used remains same as that to produce small area. As it can be seen in figure 2.34, the continuous graphene grown on copper has increased from first to second generation. Such large area of graphene could be useful for industrial application if it is transferable to different substrates which is demonstrated in chapter 2.

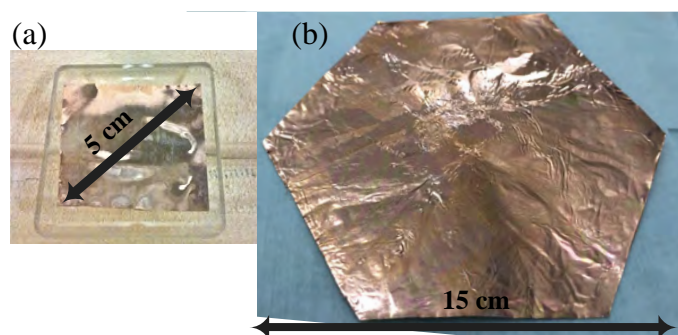


Figure 1.12: Photo of graphene grown on copper foil in (a) First generation. (b) Second generation.

This section focusses on the macroscopic structure of CVD graphene. However the physical properties arise from the microscopic scale structure which is discussed in the next section.

## 1.4 GROWTH OF LARGE GRAPHENE SINGLE CRYSTALS

The main advantage of continuous polycrystalline graphene is that we can grow it at any desired area, which is suitable for various applications. However two main limitations come from its intrinsic structure which derives from its formation. Figure 1.13 shows the process of formation of the continuous graphene. In figure 1.13(a), the graphene is not continuous due to short duration of precursor gas injection. However with increasing time of injection, the individual flakes grow bigger until they start to touch each other as shown in figure 1.13(b). If the growth time is long enough then the flakes percolate to form continuous graphene as shown in figure 1.13(c).

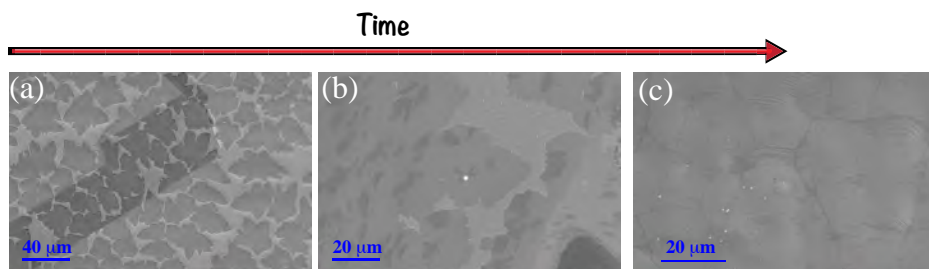


Figure 1.13: Evolution of mosaic monolayer graphene growth. (a) and (b) SEM images of flower shaped graphene percolating with time on copper with increasing time of precursor injection. (c) SEM image of continuous graphene on copper

The first problem of such continuous growth of graphene is that the boundaries that connect different grains are mechanically weaker. The boundaries are formed of strained pentagons and heptagons of carbon atoms in order for different orientation of grains to form a continuous graphene [25]. Such continuous graphene is suspended over pillars as shown in figure 1.14(a) but due to strain the graphene is torn along the boundaries.

It is also demonstrated in ref [19] that the boundaries are detrimental to the electron transport. In figure 1.14(b), an experiment is conducted by Cummings *et al* with graphene of variable domain sizes in which the resistance is measured by four probes measurements. It is found that the sheet resistance of graphene decreases if the electrons cross through lesser number of graphene boundaries as shown in figure 1.14(c). Hence it becomes imperative to grow graphene crystals with large domain size in order to fabricate devices such as FETs with uniform behaviour.

From figure 1.13(a) and (c), we can observe that the nucleation density of graphene plays an important role in the grain size of the graphene. If the density is high, the nucleation sites are close to each other. Graphene starts to grow from these sites till they touch each other. At this point graphene is continuous and covers the full surface

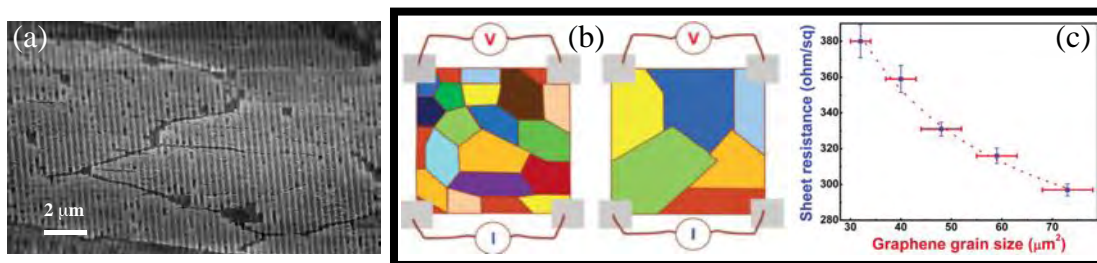


Figure 1.14: Limitations of polycrystalline graphene. (a) SEM image of polycrystalline graphene suspended over pillars. Graphene is torn due to stress at the boundaries between grains. (b) Schematic of sheet resistance measurements of graphene with small and large grain sizes. (c) Measurement of sheet resistance of graphene with different grain size. ((b) and (c) adapted from ref [19])

of copper foil which prevents further catalysis of precursor gas. Therefore the key to obtaining large grains/crystals of graphene is to decrease the nucleation density.

Researchers have tried to decrease the nucleation density by annealing for a (3h) long duration at atmospheric temperature [26], electropolishing the surface [27], melting copper foil and recrystallizing it [28] or even starting from single crystal copper [29]. Lee *et al* showed that macroscopic single crystals of graphene can be grown over Germanium single crystals [30]. Due to the unidirectional orientation of nucleation centers of graphene on single crystal of Germanium, a wafer scale single crystal graphene was obtained figure 1.15(a). The single crystal of graphene was also transferrable to other substrates as shown in figure 1.15(b).

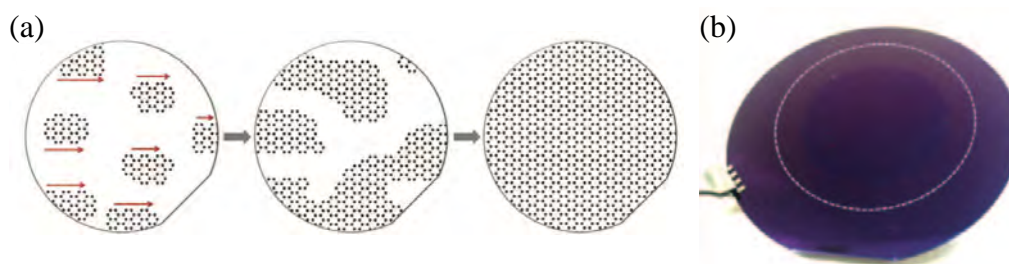


Figure 1.15: 4 inch wafer-scale single crystal growth of graphene on Germanium. (a) Schematic of unidirectional nucleation and percolation process of graphene on Germanium. (b) Photograph of single crystal graphene transferred onto SiO<sub>2</sub>/Si wafer. (figures adapted from ref [30])

In ref [17], they allowed the inactive  $\text{Cu}_2\text{O}$  to remain on the surface of copper which prevented the precursor gas to come in contact with copper and form nucleation centers. This was done by increasing the temperature from RT to  $1070^\circ\text{C}$  of growth chamber in non-reducing gas such as Ar as shown in figure 1.16(a). There is a initial flow of hydrogen at much lower temperature to clean the surface from dust particles but it does not affect the  $\text{Cu}_2\text{O}$ . In figure 1.16(b), we can observe single crystal graphene with darker contrast which are in the order of few millimeters.

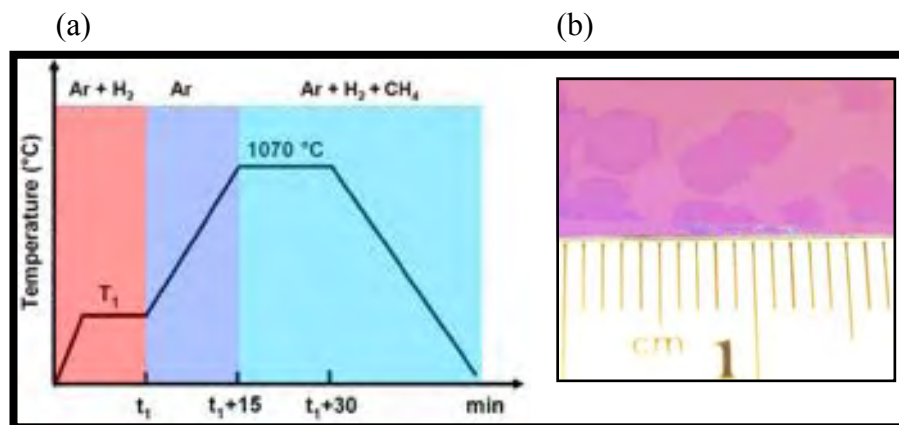


Figure 1.16: Millimeter size single crystal growth. (a) Schematic of growth recipe for large single crystal graphene and (b) photograph of single crystal graphene grains which can be seen by bare eyes. (figures adapted from ref [17])

Though different and sometimes contrasting mechanisms have been proposed to grow large crystals of graphene, we investigated the growth mechanism. In order to decrease the nucleation density, we passivated the copper surface by increasing the thickness of the  $\text{Cu}_2\text{O}$  layer by heating the copper foil at ambient atmosphere. As shown in figure 1.17, copper foil heated to different temperature gives rise to different colors of  $\text{Cu}_2\text{O}$  correspond to different thickness of the oxide layer as shown in the schematics below.

The effect on domain size due to increasing thickness of  $\text{Cu}_2\text{O}$  layer on the copper can be seen in figure 1.18. The single crystals of graphene with 30, 40 and 50  $\mu\text{m}$  size corresponds to  $\text{Cu}_2\text{O}$  layer pre-annealed at  $100^\circ\text{C}$ ,  $200^\circ\text{C}$  and  $300^\circ\text{C}$ . This clearly shows that with increasing thickness the nucleation density decreases which allows for larger single crystal growth. The parameters for growth are shown below the SEM images. All the copper foils were inserted at the same time into the CVD chamber and temperature was raised from RT up to  $1020^\circ\text{C}$  in the presence of 100 sccm of Ar at 0.1 mbar during 90 minutes. 4 sccm of pure  $\text{CH}_4$  was injected for a period of 7 minutes in presence of



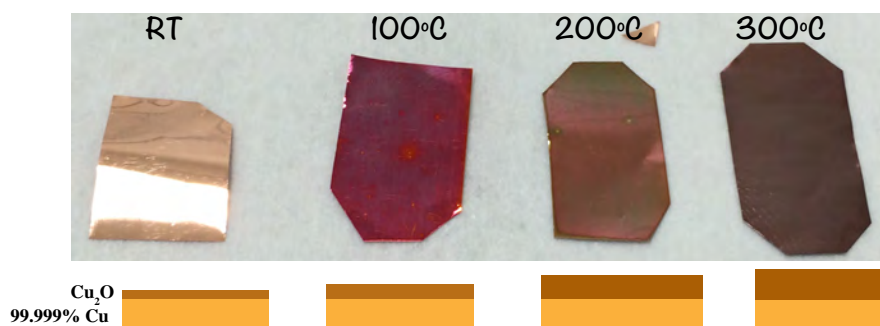


Figure 1.17: Photograph of copper foil pre-annealed hard baked to different temperature in ambient atmosphere. Below are schematics showing corresponding relative thickness of  $\text{Cu}_2\text{O}$  layer which gives rise to different colors.

500 sccm of Ar and 1000 sccm of  $\text{H}_2$ . The total pressure was 10 mbar and corresponding partial pressure are mentioned in the table 1.

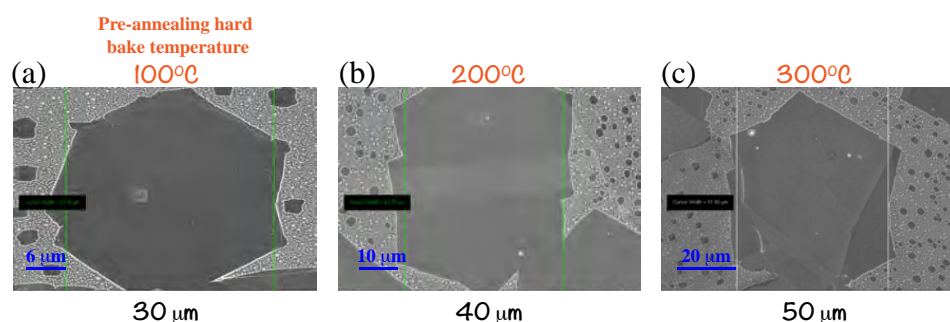


TABLE 2

**Ramp heat conditions**

100 sccm Ar @ 0.1mbar  
RT to 1020°C in 90 minutes

**Growth Parameters**

$\text{CH}_4 = 4$  sccm  
Ar = 500 sccm  
 $\text{H}_2 = 1000$  sccm  
Total Pressure = 10 mbar

**Partial Pressure**

$\text{CH}_4 = 0.026$  mbar  
Ar = 3.32 mbar  
 $\text{H}_2 = 6.64$  mbar  
10 mbar

Figure 1.18: Effect of  $\text{Cu}_2\text{O}$  layer on graphene growth. SEM images of single crystal graphene grown on copper pre-annealed at (a) 100°C, (b) 200°C and (c) 300°C at ambient atmosphere. The size of crystals are shown below the SEM images. Table 2 gives the growth parameters. "Ramp heat conditions" is the atmosphere in CVD chamber during increasing temperature from RT to 1020°C.

Though some effect of the thickness of  $\text{Cu}_2\text{O}$  layer on the final graphene crystal size was observed in figure 1.18, the size of the crystals were still limited to few tens of  $\mu\text{m}$ .

A similar growth at 20 mbar is shown in the figure 1.19(a). The maximum size of crystal was around 160  $\mu\text{m}$ . In order to further decrease the nucleation density, the partial pressure of  $\text{H}_2$  was reduced. Decreasing partial pressure of  $\text{H}_2$  leads to slower etching of  $\text{Cu}_2\text{O}$  layer on copper resulting in fewer nucleation sites.

Here we used 100 sccm of diluted  $\text{CH}_4$  (500 ppm in Ar) with 100 sccm of Ar and 150 sccm of  $\text{H}_2$ . This way we have altered the ratio of  $\text{H}_2/\text{Ar}$  from 2 to 0.75 and brought down the partial pressure of  $\text{H}_2$  as shown in table 3 and 4. Another factor that plays a role in nucleation density is the ratio of  $\text{H}_2/\text{CH}_4$  as demonstrated by Zhou (et al) in ref [17]. They found that higher the ratio, lower is the nucleation density and the rate of growth. We followed a similar procedure and increased the ratio of  $\text{H}_2/\text{CH}_4$  to 3300 which made it possible to grow crystal as large as 300  $\mu\text{m}$ . The time taken is much higher (90 minutes), as the amount of carbon precursor injected has decreased due to dilution in Ar. We note that the size of the crystals can be increased to millimeter level with increasing growth time.

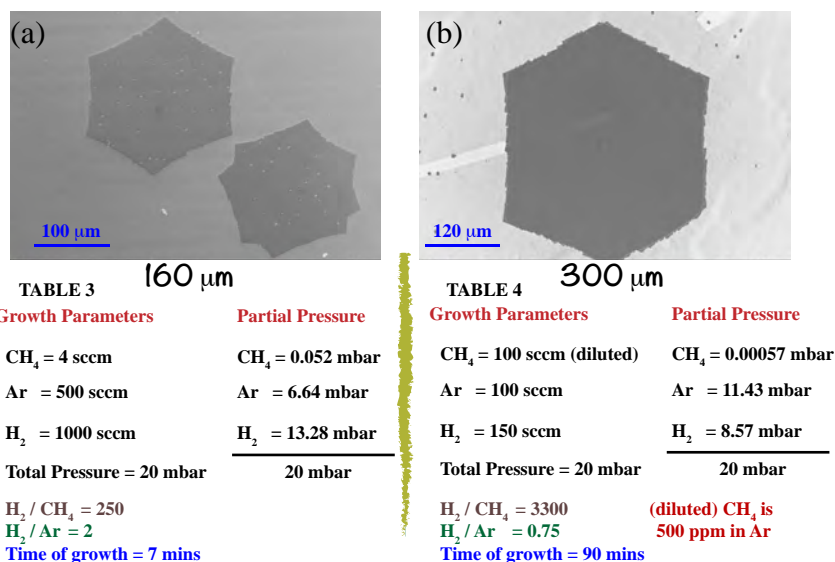


Figure 1.19: Effect of partial pressures of gasses on graphene growth. (a) and (b) Single crystal graphene grown on copper according to parameters in Table 2 and Table 3 respectively. In both the cases the "ramp heat conditions" was same as figure 1.18

The average size of crystals due to variation of oxide thickness can be seen in figure 1.20(a). Here we notice the average size of crystals increases from 39 to 50  $\mu\text{m}$  with an increasing oxide thickness. However by increasing the pressure of the CVD chamber, the average crystal size can be increased significantly upto 165  $\mu\text{m}$ . Further dilution of

CH<sub>4</sub> and H<sub>2</sub> in Argon gas allows us to grow larger average size crystals of around 344  $\mu\text{m}$  as shown in figure 1.20(b).

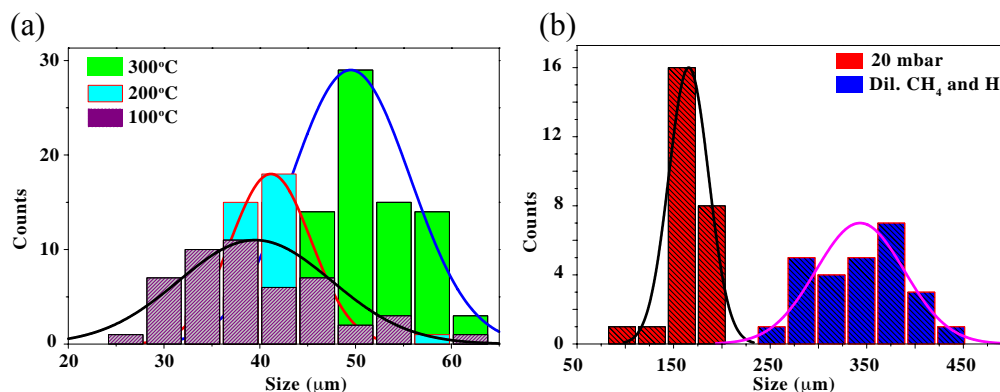


Figure 1.20: Statistics of crystal size due to different growth conditions. (a) Effect of oxide thickness: dark red (Pre-annealed at 100°C), mean size = 39  $\mu\text{m}$ , blue (Pre-annealed at 200°C), mean size = 41  $\mu\text{m}$ , green (Pre-annealed at 300°C), mean size = 50  $\mu\text{m}$ . (b) Effect due to pressure (20 mbar), mean size = 165  $\mu\text{m}$  (red) and dilution of CH<sub>4</sub> and H<sub>2</sub>, mean size = 344  $\mu\text{m}$  in Argon gas (blue) at 20 mbar.

In this section, we have demonstrated a method to grow large single crystals and the different parameters that play a role in the nucleation density. However we need to understand the growth mechanism better.

### 1.5 LARGE SINGLE CRYSTAL GROWTH MECHANISM

In the previous section, we have seen that the copper surface preparation is crucial to perform the growth of large single crystals. In this section we propose a mechanism to explain the growth process as described on figure 1.21. In the first case, when the amount of hydrogen (blue balls) is high, the size of the crystals is restricted to 160  $\mu\text{m}$  crystal. The hydrogen is able to etch through the inactive Cu<sub>2</sub>O layer, allowing the CH<sub>4</sub> (black balls) to reach the copper surface. Carbon is adsorbed in these sites and ultimately form the nucleation centers for single crystals. In figure 1.21(b), the amount of hydrogen has decreased while the Ar (green balls) has increased inhibiting etching of Cu<sub>2</sub>O layer. At the same time, we also use diluted CH<sub>4</sub> in Ar which decreases the amount of carbon atoms. By increasing the Ar gas, we reduce the amount of carbon adsorbing on copper surface which decreases nucleation sites and lowers growth kinetics. Higher ratio hydrogen to CH<sub>4</sub> (H<sub>2</sub>/Ar = 3300) also plays a role in lowering nucleation

density by removing the unstable nucleation centers from copper surface by etching the carbon atoms. Besides it also slows the the growth process which facilitates single crystal formation as shown in figure 1.19(b) while a fast growth process gives hexagonal and octagonal shaped crystals. It will be shown later in the chapter 2 that the octagonal shaped crystal is not a single crystal.

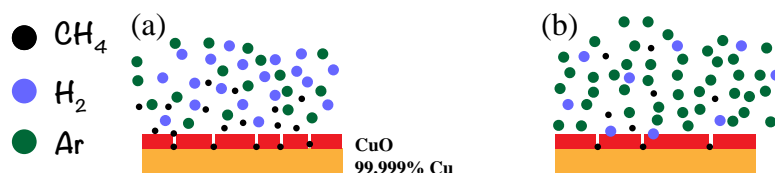


Figure 1.21: Mechanism to grow large single crystal graphene. (a) and (b) are schematic to explain the growth of graphene as shown in figure 1.19(a) and (b) respectively

Figure 1.22 shows the change in nucleation density with different parameters. By increasing the thickness of  $\text{Cu}_2\text{O}$  layer on top of copper surface, the nucleation density decreased from 37,000 to 5700 per  $\text{cm}^2$  as shown. Increasing the pressure on the CVD growth chamber while keeping all the parameters same, nucleation density was decreased to 1025 per  $\text{cm}^2$ . The density was be further reduced by playing with the partial pressures of  $\text{H}_2$ , Ar and  $\text{CH}_4$  gasses to 83 per  $\text{cm}^2$ . At such low nucleation density, it is possible to grow single crystals as large as 500  $\mu\text{m}$ .

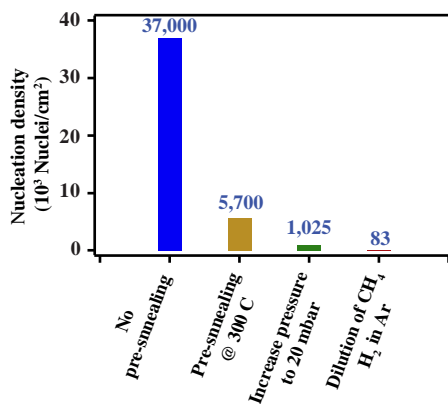


Figure 1.22: Mechanism to decrease density of nucleation with different parameters of growth. With the cumulative introduction of each parameter in the x-axis, the nucleation density of graphene can be decreased.

## 1.6 CONCLUSION

In this chapter, we introduced the standard growth of growing graphene using chemical vapor deposition (CVD) method and made two distinct major improvements to the classical method of CVD growth pioneered by Ruoff *et al* in 2009 [21]. Firstly the size of the mosaic polycrystalline monolayer graphene was increased to  $20 \times 20 \text{ cm}^2$  while keeping the advantages of the pulsed growth. This was achieved in a research scale CVD chamber where a large area growth was performed without needing extra energy. The high quality of graphene was established using SEM, Raman spectroscopy, AFM and STM.

Secondly we have been able to reach the state-of-art in growing large single crystal graphene and gave insights into its growth mechanism. We found that by increasing the thickness of  $\text{Cu}_2\text{O}$  layer on top of copper surface prevented catalysis of  $\text{CH}_4$  on copper surface which decreased the nucleation density of graphene. The density was be further reduced by increasing the pressure of CVD chamber and playing with the partial pressures of  $\text{H}_2$ , Ar and  $\text{CH}_4$  gasses to 83 per  $\text{cm}^2$ . This way we managed to grow graphene single crystals as large as  $300 \text{ }\mu\text{m}$ .

In this chapter we have shown how large area monolayer and micron-size single crystal graphene can be grown using chemical vapor deposition (CVD) method. Scanning tunneling microscopy (STM) and Raman spectroscopy images show the high quality graphene at a nano and macro scale level. However, in order to take advantage of the amazing properties of graphene, it needs to be transferred to different substrates. Different transfer techniques have been developed worldwide which will be presented in the next chapter. I have focussed on optimizing the transfer to target large scale wafers, smart substrates and artificial stacks.

## TRANSFER OF GRAPHENE FOR SUPPERLATTICES AND HETEROSTRUCTURES

Since the interaction of graphene grown on Cu is weak, it is a priori possible to transfer it on any kind of substrate, providing an appropriate transfer technique. One of the first methods developed was liquid-assisted transfer method by Xuesong *et al* [21]. The method involves spin-coating a polymer layer on graphene and etching the metallic layer which is then transferred to other substrates. The method will be described in details later. Variations of this method have been developed to transfer graphene such as roll-to-roll method compatible with industrial throughput was developed by Sukang *et al* where graphene was transferred onto plastic substrate (figure 2.1(a)). The liquid transfer method involves etching of copper foil which add to the cost of graphene production [22]. Therefore Gao *et al* developed a hydrogen bubbling method which does not involve dissolving of copper so it can be reused for growth [31]. Here hydrogen bubbles are created between graphene and metal foil using electrolysis as shown in figure 2.1(b) and promote delamination of graphene from copper.

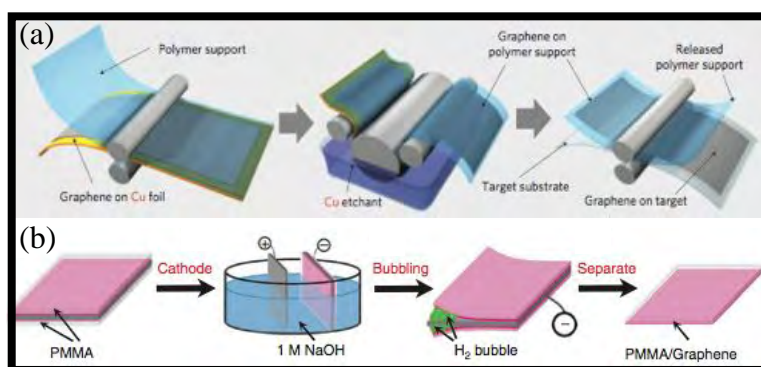


Figure 2.1: Wet graphene transfer methods: (a) Schematic of roll-to-roll process of graphene transfer. Process involves polymer adhesion on graphene, removal of copper using etching and dry transfer printing onto substrate [22]. (b) PMMA is applied to Pt + graphene which acts as cathode during the charge transfer. This creates hydrogen bubbles between the graphene and the Pt plate which facilitates the removal of graphene + PMMA from substrate. This is then transferred to target substrate [31].

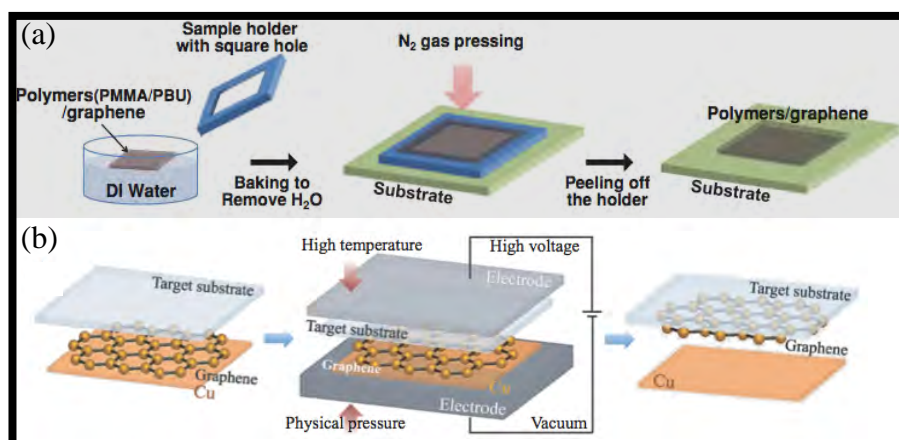


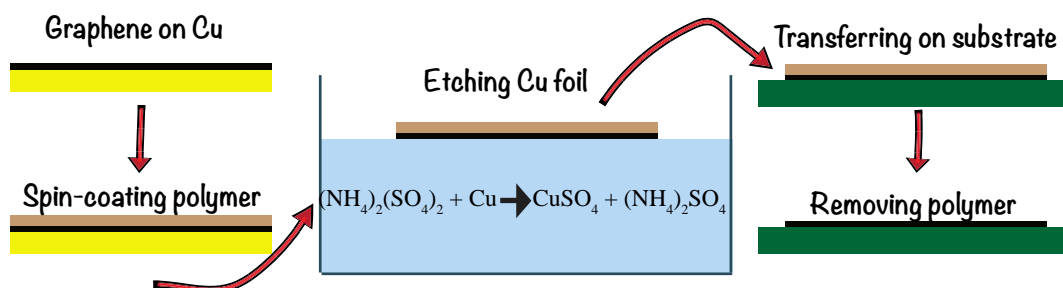
Figure 2.2: Dry graphene transfer methods (a) The graphene + PMMA is transferred to a holder and baked to remove water. Thereafter it is transferred to substrate and pressed against it by blowing nitrogen gas [32]. (b) The target substrate is pressed against graphene + Cu with high pressure and a high voltage is applied across it. This facilitates the transfer [33].

Many times liquid molecules may be trapped in wet transfer methods so partial dry transfer by blowing away the molecules was developed in ref [32]. As shown in figure 2.2(a), graphene is first transferred to a holder which is dried before transferring to another substrate. In many cases there are presence of wrinkles during the transfer process. Some of these wrinkles can be removed by diluting the polymer (PMMA) supporting layer with ethyl lactate [34]. Another completely dry direct method involves PMMA-free direct transfer from copper foil to any substrate using high pressure and high temperature shown in figure 2.2(b). This method does not involve liquid but the transfer is not conformal to the substrate [33].

In this work, we have fabricated different graphene-based devices by liquid-assisted transfer method which is known for high success rate and its versatility to any target substrates. The question addressed in the following is how far can we optimize this technique in order to fabricate ever more advanced graphene structures while keeping its properties intact? The detailed process is mentioned in section 2.1. Thereafter we utilize this method to fabricate hetero-structures of graphene such as bilayer graphene (BLG) in section 2.2. The transfer technique was modified to suspend graphene in large area in section 2.3 and to various insulating substrates as shown in section 2.4. In section 2.5, graphene has been used as a active component for various devices. Finally we demonstrate a new method to transfer graphene in flexible substrates in section 2.6.

## 2.1 EXTRACTING GRAPHENE FROM THE COPPER FOIL

Copper etching has been known for long time in microelectronics. Therefore it appears natural to apply similar protocols for copper etching to release graphene from its catalytic substrate. In this section, we present in details the wet transfer method that we used throughout this thesis, which has been adapted from [21]. A schematic of the transfer method of graphene on various substrates is shown in figure 2.3(a).



cf

Figure 2.3: Process flow of graphene wet transfer involving copper foil as a sacrificial layer: PMMA is spin-coated on Graphene/Cu foil which is etched in  $(\text{NH}_4)_2(\text{SO}_4)_2$  to remove copper. Then it is transferred on  $\text{SiO}_2$  wafer after repeated washing in de-ionized water. PMMA is removed using acetone and the sample is dried by blowing nitrogen.

1. Graphene is grown using CVD method on copper foil. 4% Poly(methyl methacrylate) (PMMA) is spin-coated onto graphene such that the thickness is around few micrometers.
2. Thereafter the copper foil is etched in  $(\text{NH}_4)_2(\text{SO}_4)_2$  until the copper is no more visible. The time of etching and selection of etchant is important which is discussed in Chapter 3.
3. In order to remove any kind of ions adsorbed onto graphene, the PMMA+graphene is washed several times in de-ionized water (DI) baths.
4. Thereafter the PMMA+graphene is fished onto the target substrate and left to dry naturally at room temperature.
5. This is then heated at around  $120^\circ\text{C}$  for graphene to promote adhesion to substrate and remove any trapped water molecules.



All different graphene-based structures studied in this thesis have been fabricated according to this process or to similar processes that have been optimized for specific applications. I will present the implementations of this technique in the following and highlight the possibilities it opens. First promising implementation of graphene transfer is the realization of artificial stacks.

## 2.2 GRAPHENE STACKS BY MULTIPLE TRANSFER METHOD

One of the drawback of graphene has been its absence of bandgap in its electronic structure which prohibits its use in electronics industry. However it has been found that the bandgap exists in bilayer graphene and it can be tuned depending on the rotation angle between the twisting layers of graphene [35, 36]. In figure 2.4(a) and (b) are the two electronic band structures of twisted bilayer graphene with  $13.17^\circ$  and  $10.8^\circ$  of rotation between graphene layers respectively. This bandgap exists at the M point and decreases as the rotational angle between the two layers of graphene decreases [37]. (At smaller angles, this energy gap can be less than the laser energy used for probing the phonons.) Due to the rotation, the Dirac cones move in the momentum space which causes the overlapping band structure, marked by green arrows in figure 2.4(c). The presence of this overlapping band causes the density of states (DOS) for bilayer graphene to have Van Hove singularities (red curve). It is absent if the two layers are not interacting in double layer graphene [38] and has linear DOS (blue curve) as shown in figure 2.4(d). These Van Hove singularities can be directly probed using scanning tunneling microscopy (STM) in twisted bilayer graphene [39].

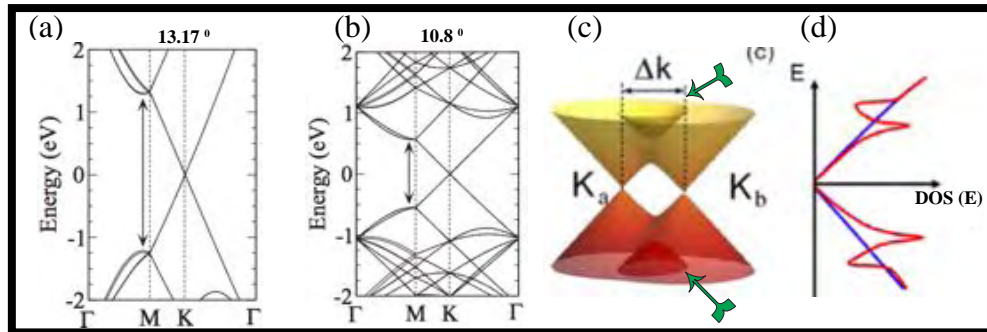


Figure 2.4: Bilayer graphene electronic properties. (a) and (b) Band structure of bilayer graphene with  $13.17^\circ$  and  $10.8^\circ$  between the graphene layers [37] (c) Energy dispersion relation at the vicinities of two Dirac cones. Due to band-overlap between two Dirac cones Van Hove singularities are induced marked by green arrows. (d) Density of states (DOS) of bilayer when two layers are interacting (red) and non-interacting (blue) curves [38].

Since electrons and phonons are strongly coupled in graphene, the modification of band structure affects the phonon intensity, frequency and FWHM. This can be observed in the figure 2.5(a). Here the naturally grown multilayer graphene flake was transferred on TEM grid and rotation angle of the bilayer graphene was determined using electron diffraction as shown in false colored image. The Raman spectroscopy was recorded corresponding to the specific places and plotted [40]. It can be observed that the different rotation angles give rise to specific Raman spectrum which will be shown in more details later in the chapter.

The optical phonons are also sensitive to increasing number of graphene layers and laser energy. In figure 2.5(b), 2D Raman spectra, probed by laser wavelengths 514 nm and 633 nm, for different number of layers of graphene can be observed [41]. The shape of the 2D phonon can be used to count the number of layers when the different layers are interacting with each other. Non-interacting graphene layers would simply multiply the intensity of 2D phonon with number of layers without changing its shape. Bilayer graphene systems have different interlayer distance, stacking faults and rotational mismatch which result in different optical, electronic and mechanical behavior. Due to such tunable parameters, these systems have found application in thermoelectric devices [42], photodetectors [43], tunable plasmonic devices [44], field effect transistors [45].

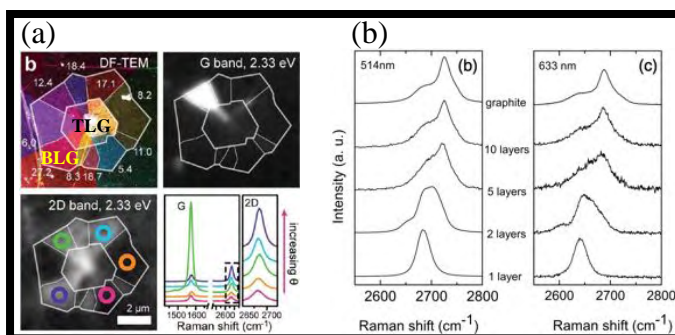


Figure 2.5: Raman spectroscopy of rotated bilayer graphene (a) False colored image of naturally grown bilayer (BLG) and trilayer (TLG) graphene. The intensity mapping of the G and 2D band is shown. The spectra corresponding to different regions of rotated bilayer graphene can be observed [40]. (b) 2D Raman spectra of different layers of graphene with 514 nm and 633 nm laser [41].

Though there are lot of possibility of science and useful applications to be discovered in bilayer graphene systems, there is no proper method to fabricate them. In the following section we provide a methodology to fabricate such devices and probe the interaction between stacked layers using optical phonon Raman spectroscopy.

### 2.2.1 Fabrication optimization for multilayer transfer

We have realized artificial stacks of graphene by using the liquid transfer technique to perform layer by layer deposition. Starting from monolayer graphene on copper, we have transferred graphene on a substrate one by one with macroscopic alignment to ensure superimposition of the layers.

Figure 2.6(a) shows schematic of artificially transferred graphene crossbar. Optical image of monolayer graphene ribbons transferred to form a crossbar is shown in figure 2.6(b). Unlike in ref [46], the crossbars is made without costly alignment tools and is fabricated from CVD graphene. Similarly double transfer of hexagonal and octagonal shaped graphene was fabricated as seen in figure 2.6(c).

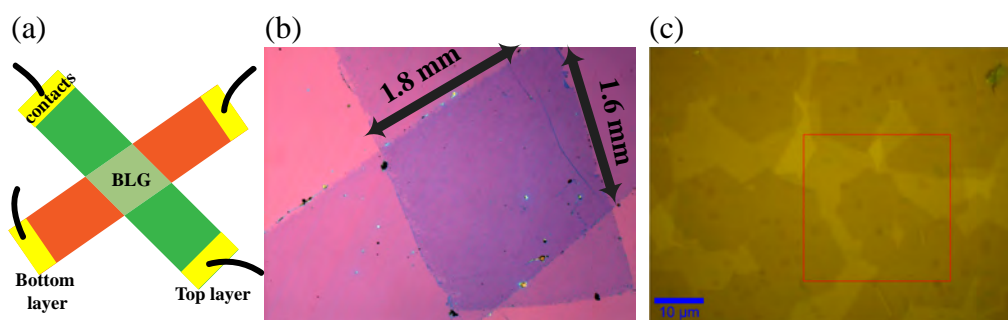


Figure 2.6: Artificial bilayer graphene. (a) Schematic of crossbar. (b) Macroscopic graphene crossbar fabricated from monolayer graphene ribbons. (c) Two layers of hexagonal and octagonal crystal graphene transferred onto each other as visible by the contrast change. Red square shows the region where Raman mapping was done shown later.

Although transferring a single layer of graphene onto different substrates has been mastered by various groups, transferring the second graphene has been problematic for various reasons. A typical failure in first attempt is shown in the optical image in figure 2.7(a), where the second strip of graphene was attempted to transfer. The red boundary shows the first strip and black boundary shows the second strip. Two problems that arise are

1. After the first strip of graphene is transferred, the substrate becomes hydrophobic with no possibility to make new oxygen plasma nor acidic treatment. As the sample is lowered into DI water to fish the second strip, the water molecules start dewetting from the sample rapidly. This phenomenon removes the first strip of graphene due to strong surface tension.

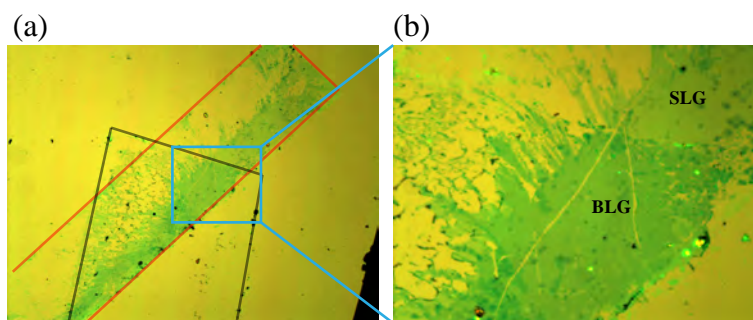


Figure 2.7: Problems related to first attempt of sequential transfer (a) Red border shows the position of first graphene ribbon and black border shows the second graphene ribbon. (b) A zoomed view of blue box in (a) to show the two layers of graphene.

2. The second strip scarcely sticks to  $\text{SiO}_2$  substrate as the surface is hydrophobic: it cannot be turned to hydrophilic again with oxygen plasma as that would remove the first graphene. From the contrast in figure 2.7(a) and (b), it has partially stuck only to first layer of graphene while the other parts are missing.

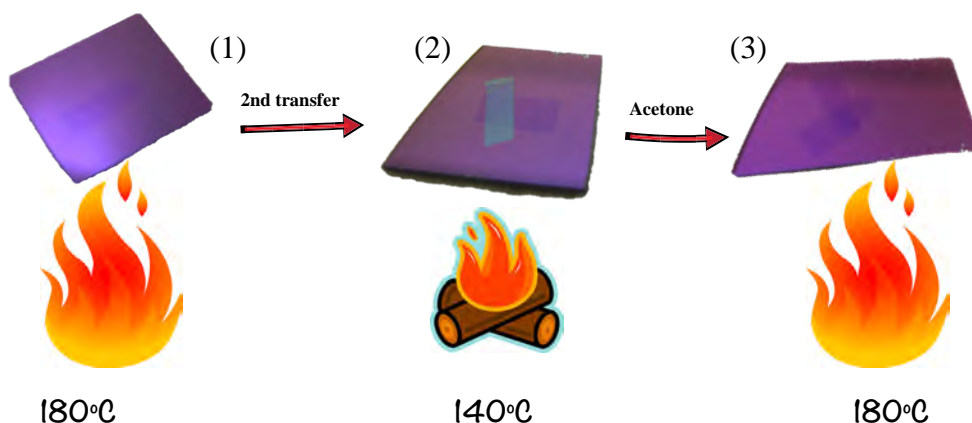


Figure 2.8: Process involving hard baking during transfer. (1) single graphene ribbon heated to  $180^\circ\text{C}$ . (2) second graphene is transferred with PMMA and heated to  $120^\circ\text{C}$  after drying. (3) Graphene crossbar is heated to  $180^\circ\text{C}$  after removal of PMMA from second ribbon

Figure 2.8 shows how to solve the above two problems in order to create bilayer graphene efficiently.

1. The first step involves slowly heating the graphene on SiO<sub>2</sub> after the first transfer to 180°C in clean room atmosphere. This helps molecules trapped between graphene and substrate to desorb so that graphene sticks much better on surface and remain unaffected by surface tension of DI water.
2. Transferring the second layer of graphene+PMMA onto the first layer. Drying the DI water and slowly heating the sample to till 140°C.
3. After the PMMA has been removed by acetone it is important to make sure the second layer sticks to first one, so another slow heat treatment is needed till temperature is increased to 180°C. The last image shows optical image of graphene crossbar. The region of overlap shows slightly darker region due to two layers of graphene.

Managing the realization of a double layer stack does not imply that this artificial structure is equivalent to an intrinsic bilayer. Many aspects come into play: interlayer pollution, rotation angle between the layers, uniformity of the stack. In the next subsection, we characterize the interlayer coupling obtained in our systems and show that the 2D phonon is the most sensitive to rotation between two layers of graphene.

### 2.2.2 *Detecting inter-layer interaction using Raman spectroscopy*

After the graphene ribbons were transferred to form bilayer stacks, one of the important question that arises is whether these artificial stacks are interacting with each other like the naturally grown bilayers. A powerful tool to probe this interaction is by using inelastic scattering of light such as Raman spectroscopy. It has been demonstrated that the phonon frequency, FWHM and shape is sensitive to the number of layers and rotational angle between the layers ref [38,40].

Figure 2.9(a) shows the optical image of the single and bilayer graphene which is fabricated by transferring multilayer CVD graphene grown by standard method. The top of the image with darker contrast is the bilayer layer graphene which is transferred on single layer graphene seen in lighter contrast. The naturally grown bilayer (NBLG) graphene patches can also be seen in the image which are marked by green arrows. A wrinkle present in single layer graphene that extends to the double layer region is shown by blue arrow. Figure 2.9(b), (c) and (d) show the G peak frequency, FWHM and intensity Raman mapping respectively. The frequency and FWHM mappings show two different regions which represent the bilayer and single layer. However, the intensity mapping shows three different regions: one single layer region and two different regions in bilayer graphene. BLG-1 region has very high intensity of G peak but has same frequency and FWHM as that of BLG-2 region which has lower intensity of G peak.

The anomalously high intensity G peak in BLG-1 region is present because the laser energy (2.33 eV for 532 nm) matches the bandgap created by the Van Hove singularities due to interaction of the two graphene layers as shown in figure 2.4. The resonance effect increases the population of electron-hole pairs that interact with phonons causing the high intensity of G peak ref [38]. According to ref [40], for 532 nm laser to fulfill resonance condition, the rotation angle between the graphene layers should be around 13.4 degrees.

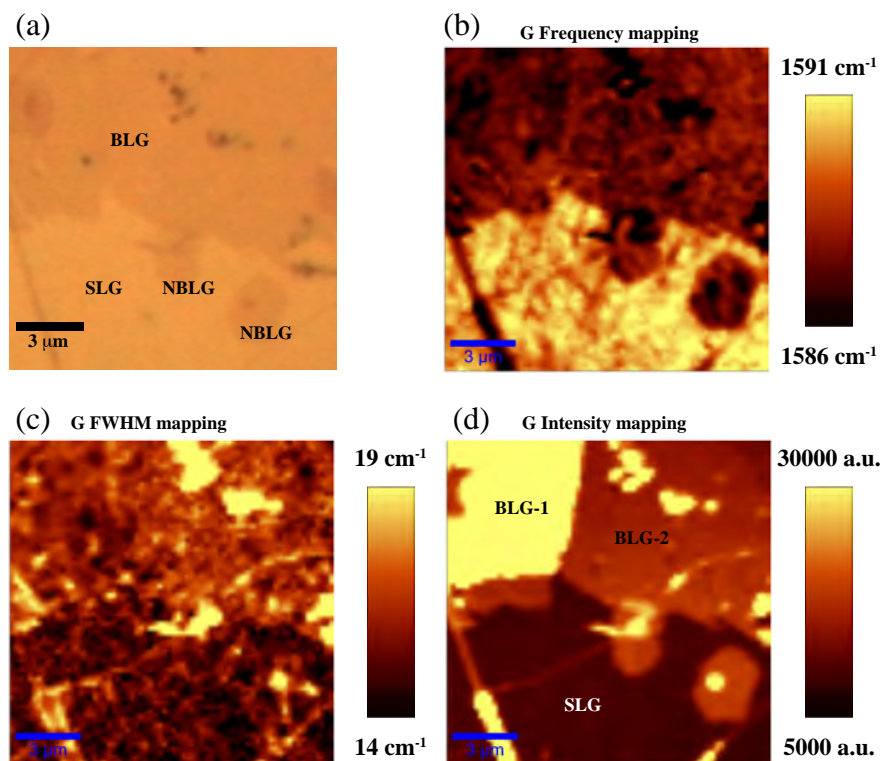


Figure 2.9: Raman G phonon characterization of transferred bilayer. (a) Optical image of artificially transferred bilayer graphene using standard CVD graphene with multilayer patches. Green arrows point towards naturally grown bilayer graphene patches and blue arrow points to wrinkle. (b), (c) and (d) are G frequency, G FWHM and G intensity Raman mapping respectively. Laser wavelength is 532 nm. (Crossbar fabricated by Shelender KUMAR, Master student, Institut Néel)

Similarly the 2D FWHM, frequency and intensity Raman mappings also show two distinct regions in the bilayer region while the monolayer region shows no variation as shown in figure 2.10 (a), (b) and (c) respectively. Figure 2.10(d) shows the Raman spectra of different parts of the crossbar. It can be seen that the intensity of SiO<sub>2</sub> peaks at 520.7

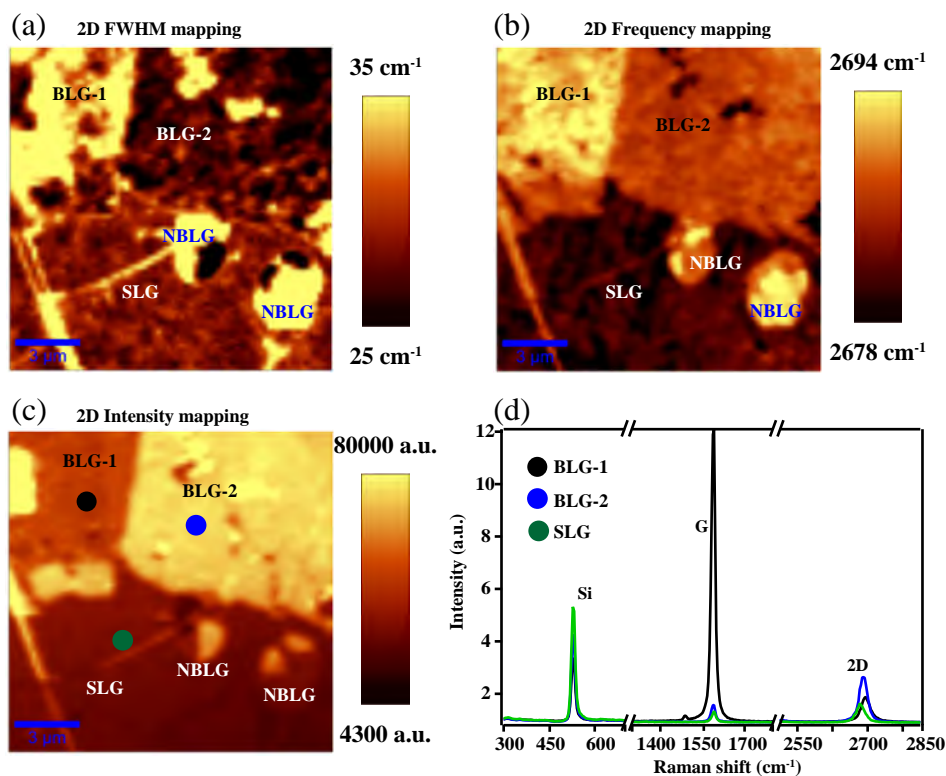


Figure 2.10: Raman 2D phonon characterization of transferred bilayer. (a), (b) and (c) are 2D FWHM, 2D frequency and 2D intensity Raman mapping of figure 2.9(a) respectively. Green arrows point towards naturally grown bilayer graphene patches and blue arrow points to wrinkle. (d) shows the Raman spectra from three different regions in (c). Black and blue spectra are from BLG-1 and BLG-1 regions respectively in bilayer graphene while green spectrum is from single layer graphene. Laser wavelength is 532 nm. (Crossbar fabricated by Shelender KUMAR, Master student, Institut Néel)

cm<sup>-1</sup> are almost equal for the three spectra taken at three different spots. This implies that there is no problem of defocussing of the optics during the measurements. On the other hand, the G peak from black spot is unusually high, even higher than SiO<sub>2</sub> but the other two peaks do not show much variation. On the other hand, 2D mode shows a lot of variation from the three different spots.

Since the crossbar was made from graphene with multilayer patches, the naturally grown bilayers are also visible in Raman mappings. They are marked as NBLG in figure 2.10. Within these bilayers there are also domains where the FWHM, frequency and intensity of 2D peak are varying as shown in figure 2.10(a), (b) and (c) respectively.

Again these variations are due to different rotational angles between graphene layers in naturally grown bilayers.

The graphene used to make the crossbar is polycrystalline in nature. So when they are stacked on top of each other, the Raman signal generated from random orientation between the layers are distinct. Therefore although they are optically similar, Raman mappings can be used to reveal the different domains. Also the Raman signal generated is similar to artificially transferred graphene which proves that our artificially created bilayer graphene has minimum contamination trapped between layers and is another proof of their interaction with each other. One advantage of artificially transferred bilayers is that we can have access to any rotation angle between the layers. Such angle is still yet random and we have no control over it. It should be possible in principle to adjust the rotation angle when using single crystal graphene for which crystallographic directions can be inferred from the crystal shape.

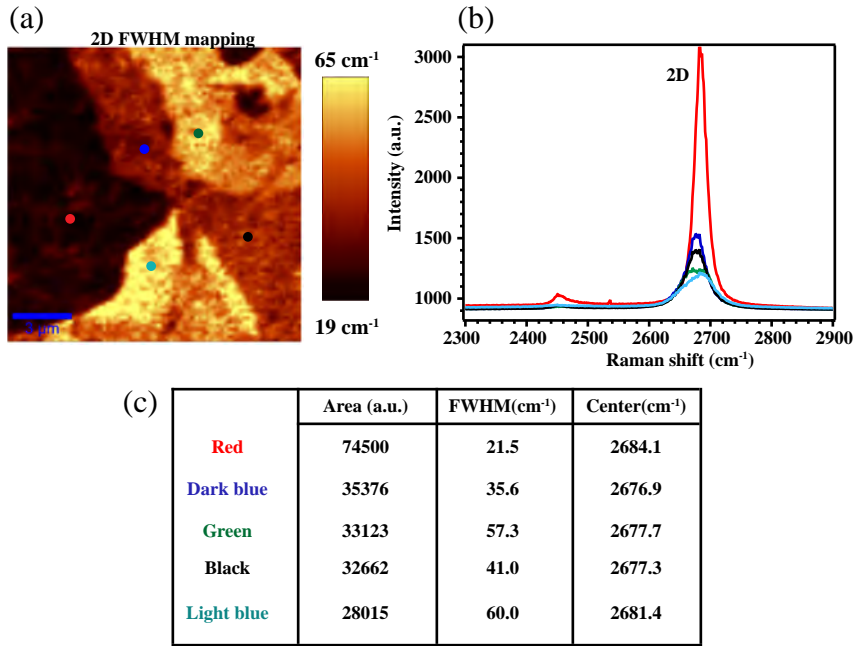


Figure 2.11: Raman 2D phonon Raman analysis of rotated bilayer graphene. (a) 2D FWHM mapping of bilayer graphene. (b) Raman spectra of different grains of bilayer graphene shown in (a). (c) Table showing Lorentzian fitting parameters from Raman spectra in (b).

In figure 2.11(a), we show a 2D Raman mapping of a region with different contrast which we attribute to different grains in bilayer graphene. The Raman 2D spectra from



different regions are shown in the figure 2.11(b) and figure 2.11(c) show the table with lorentzian values of area, FWHM and center of the 2D peaks.

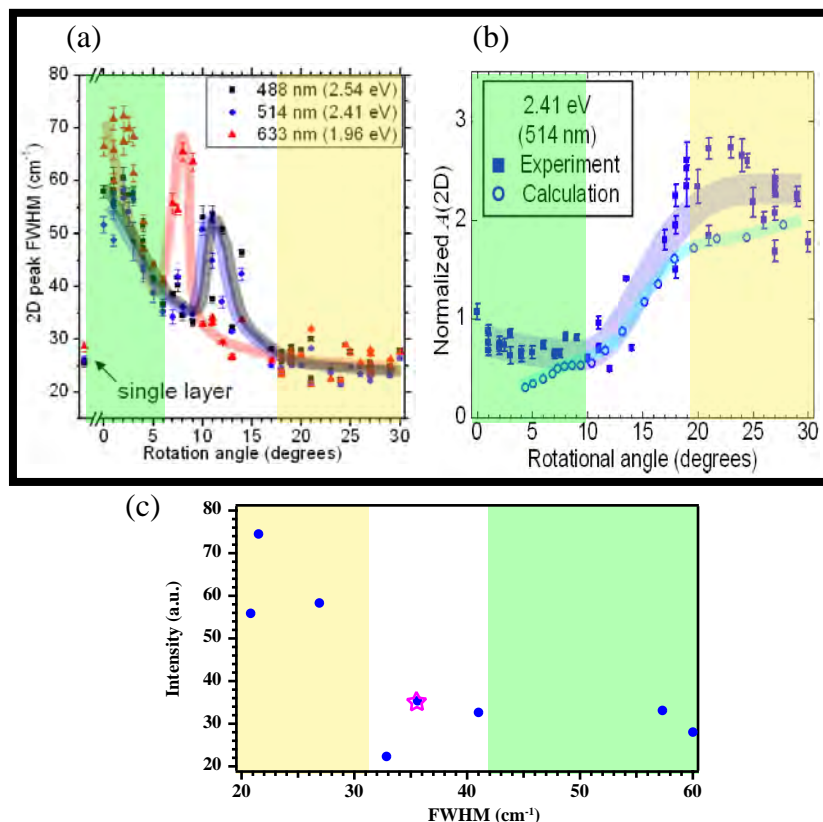


Figure 2.12: Classification of rotated bilayer graphene using 2D mode. (a) and (b) experimental and calculated values of 2D FWHM and normalized area of bilayer graphene with rotation angle between two layers with different laser wavelengths. (figures adopted from [38]). (c) Intensity vs. FWHM of graphene bilayer from our experiments. The green region represents high normalized area with low FWHM which is the reverse of yellow regions. In the white region, FWHM and position undergoes large variation which makes it difficult to classify the rotation of graphene layers due to matching of electronic bandgap with the laser energy. However angle is determined for the pink star highlighted point which is described in the text.

The values of intensity and FWHM have been used to classify the rotation angle between the graphene layers. In ref [38], the rotation angles were measured using Transmission Electron Microscopy (TEM) and Raman spectra were taken on the given spots. Figure 2.12(a) and (b) show two graphs of calculated and experimental values of 2D peak

FWHM and normalized intensity with rotational angle between graphene layers. From these plots, it can be observed that for small angles, FWHM can be as high as  $60 \text{ cm}^{-1}$  but its normalized intensity is low (green area). For high angle of rotation it is the reverse (yellow area). Since, in our case, it is not possible to measure the rotation angle between graphene layer using TEM, we have plotted intensity vs. FWHM of 2D peak from our Raman measurements in figure 2.12(c). The data has been classified in three regions. The green region shows high normalized area with low FWHM while yellow region shows the reverse. In the white region, the FWHM and intensity of 2D peak undergo a lot of variation because the laser energy is close to the energy bandgap created by Van Hove singularities in the bilayer system which makes it difficult to classify. Hence we have qualitatively use information from Raman spectroscopy to distinguish regions of high and low angle of rotation in our graphene bilayer system.

Carazo *et al* had introduced another way of identifying the rotation of the graphene layers by identifying a new peak ( $R'$  peak) in ref [47]. Bilayer graphene is expected to have a periodic potential of the superlattice originating from the 2-dimensional interaction of the two layers. This periodic potential transfers momentum to the photoexcited electrons which are scattered to create a phonon. Figure 2.13(a) shows AFM image of exfoliated graphene that has accidentally folded at certain angle to form bilayer region. The corresponding Raman spectra in figure 2.13(b) show presence of the  $R'$  peak existing near the G peak whose intensity varies with wavelength of laser. It is calculated that the position of the  $R'$  peak is not fixed but changes with rotation of the graphene layers as shown in figure 2.13(c). The  $R'$  peak is also visible in data of ref [38, 40] but was not mentioned then.

We recall that in figure 2.11(a) we were able to differentiate between different grains of bilayer graphene using 2D FWHM Raman mapping. The same 2D FWHM mapping figure 2.11(a) is shown in figure 2.14(a). This time we also map the  $R'$  peak in the same region as shown in figure 2.14(c) and we observe that it corresponds to region from where the dark blue spectrum was taken. From the position of  $R'$  peak we can now estimate the rotation angle between the two graphene layers. The position of  $R'$  peak is found to be  $1623 \text{ cm}^{-1}$  which corresponds to a rotation angle of  $\approx 5.7^\circ$ . The table gives the lorentzian parameters of the spectra from figure 2.14(c). It is shown as pink star mark in figure 2.12(b).

Thus we are able to roughly estimate rotation angle between two graphene layers using the intensity and FWHM of 2D band and also by using position of  $R'$  peak. This would not have been possible if the transfer process would not have been clean and two artificially transferred graphene would not have interacted. The technology to create artificial bilayers opens a new way to obtain any relative rotation angle between graphene layers. The method can be extended to any number of layers to create 2-dimensional stacked heterostructures.

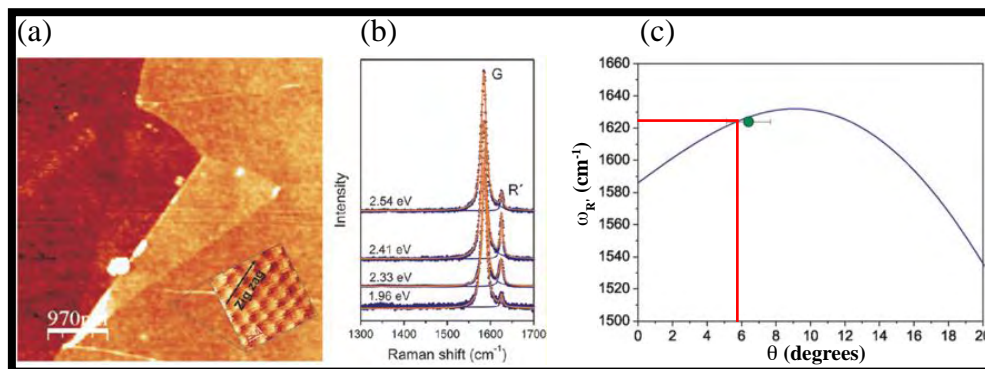


Figure 2.13: Raman R' peak as probe for rotational angle. (a) AFM image of graphene folding to form bilayer graphene. (b) Raman spectra of bilayer region in (a). (c) Variation of R' peak with the rotation between the two layers of graphene. The horizontal red line shows the position of R' peak for our graphene bilayer while vertical line gives the corresponding mis-orientation between them. (Figure adapted from [47]).

The information obtained from Raman spectroscopy of bilayer graphene provides insights into the stack from the structure of each layer. In the next subsection we will see how the graphene stack can be used as a revealing agent to probe the nature of CVD grown graphene.

### 2.2.3 Distinguishing single and poly crystalline graphene

From the previous sub-section we know that the transfer process allows the two graphene layers to interact with each other and Raman spectroscopy is an efficient tool to measure the interaction and estimate different grain of rotation in a bilayer graphene. Here we will use these informations to verify the crystallinity of the hexagonal and octagonal shaped graphene grown our CVD machine as mentioned in the Chapter 1.

One of ways to determine the crystallinity of the hexagonal shaped graphene is by using Scanning Tunneling Microscopy (STM). In this method, it is possible to scan individual atoms and check its arrangement in space. However it is almost impossible to scan crystals as big as 20 micrometers and bigger.

Raman spectroscopy mapping provides us with a tool to identify the presence of grains at larger scale when hexagonal shaped graphene is transferred on top of each other. Such a Raman mapping can be seen in figure 2.15 where (a) (b) and (c) show the 2D intensity, FWHM and frequency mapping of the bilayer region. In these figures, the bilayer region does not show any variation of 2D intensity, FWHM and frequency. This is because

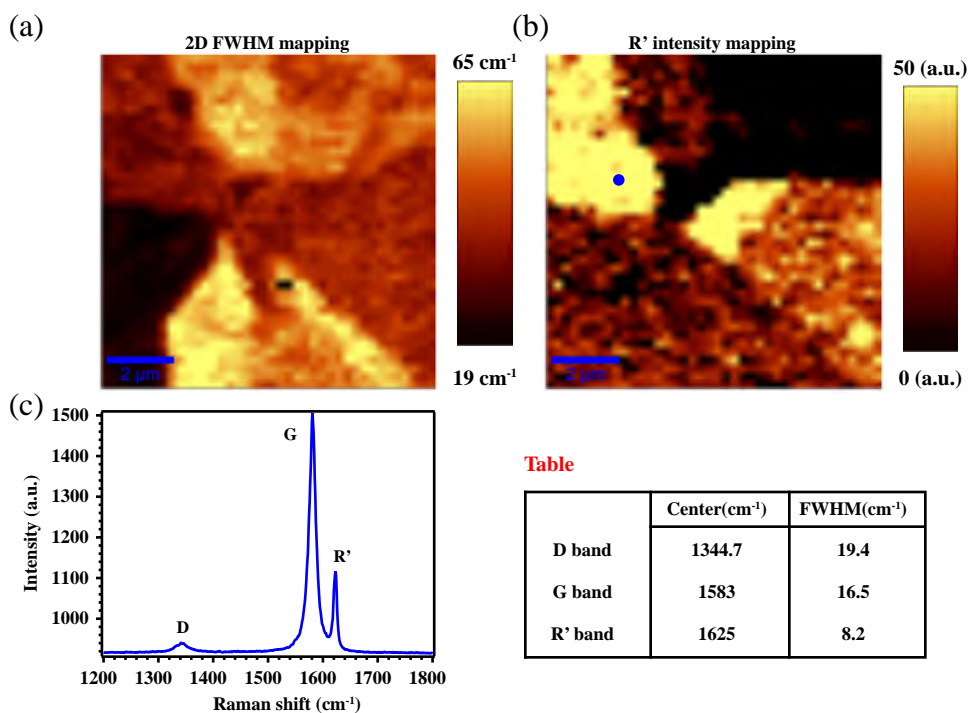


Figure 2.14: Raman R' peak analysis of rotated bilayer graphene. (a) 2D FWHM mapping of bilayer graphene (same as figure 2.11(a)). R' intensity mapping of the same area as (a). (c) Raman spectra of blue region in (b) with the lorentzian fitting parameters shown in the table.

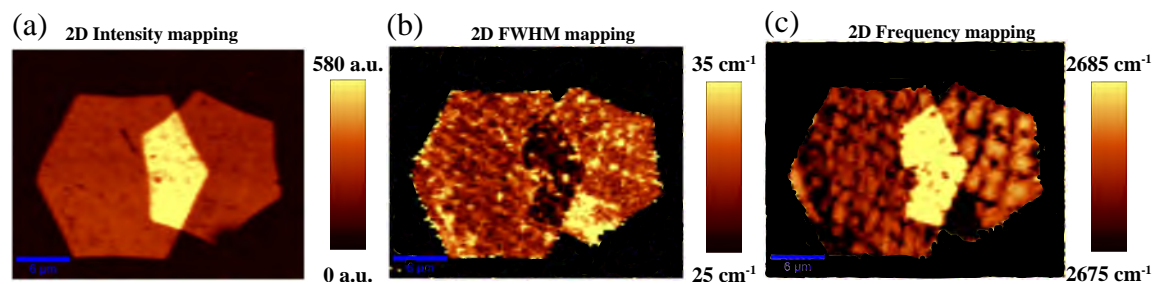


Figure 2.15: Probing crystallinity of hexagonal graphene. (a) 2D intensity (b) 2D FWHM and (c) 2D frequency mapping of hexagonal single crystal graphene.

when they are transferred on top of each other, they form only one of type rotation

angle, hence no variation in 2D spectrum. From these observations, we can infer that both the individual hexagonal graphene flake is mono-crystalline in nature.

During the growth of single crystal graphene, there are also crystals that have more than 6 sides as can be seen in figure 2.6(c). There are speculation as whether they are also single crystals like the hexagonal crystals. In figure 2.16(a), we have the G peak intensity mapping of the red square marked in figure 2.6(c). This mapping clearly shows the difference between the single layer (lower intensity) and bilayer graphene (higher intensity).

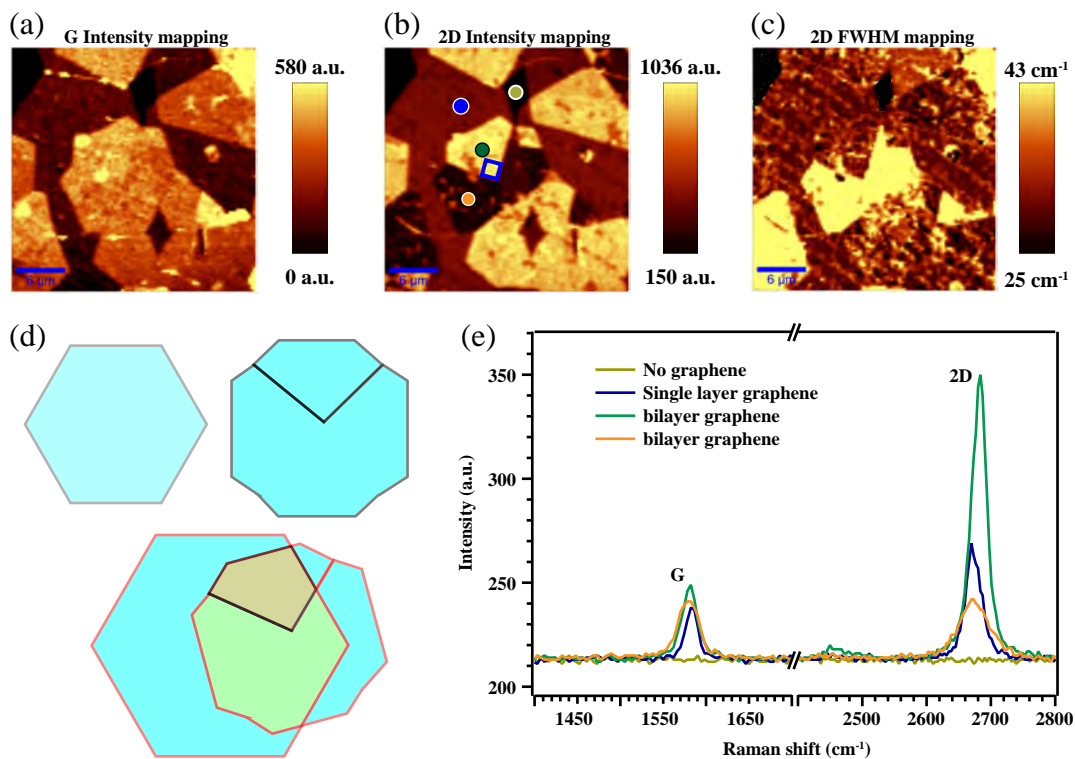


Figure 2.16: Probing crystallinity and grain boundaries of octagonal graphene. (a) G intensity, (b) 2D intensity and (c) 2D FWHM mapping of hexagonal/ octagonal graphene transferred onto each other shown by red square in figure 2.6(c). (d) Schematic showing Raman contrast of individual hexagonal, octagonal shaped graphene and when transferred on each other. The blue color indicates Raman signal from single layer graphene while brown and green indicate different Raman signal due to different rotation of the top and bottom layer caused by the polycrystalline octagonal shaped graphene. (e) Raman spectra from different spots in bilayer graphene as shown in (b).

However the 2D intensity and FWHM mappings show a different picture. The 2D intensity at the region with green dot is higher than in the region around orange dot in figure 2.16(b) but has lower FWHM as shown in figure 2.16(c). Though both these regions belong to same graphene flake, they give different signal. This is because one of the graphene crystal of bilayer is polycrystalline in nature. From figure 2.15, we know that hexagonal shaped graphene is a monocrystal, therefore we can conclude that the octagonal sided graphene is polycrystalline in nature.

The schematic in figure 2.16(c) shows the hexagonal and octagonal shaped graphene that can be observed during CVD growth. A corresponding SEM image is shown in the chapter 1. Though the octagonal shaped graphene is made from different grains, Raman spectra from circularly polarized light is not able to differentiate them in a monolayer graphene which is represented in blue color in figure 2.16(d). However when they are transferred on each other, the grains become visible due to the different rotation angles between single crystal hexagonal graphene and different grains of octagonal graphene. The Raman spectra of single layer graphene and the two different regions of bilayer graphene can be observed in figure 2.16(d).

Further this study can be used to study the grain boundaries and growth mechanism of octagonal graphene. Interestingly unlike in polycrystalline monolayer graphene, the grain boundaries in octagonal graphene are straight. They originate from the center of the flake and the grain marked by green dot makes an angle of  $90^\circ$  at the center as shown with the help of blue square in figure 2.16(b). We will need more information in order to understand such structures.

Thus we are able to probe the crystallinity of graphene at a microscopic scale. It can be used to understand the growth mechanism of single crystals of graphene and other 2D materials such as BN, TSe<sub>2</sub> etc.

Beyond stacking graphene on itself, we can imagine a wealth of smart substrates which can tailor graphene's properties through controlled graphene/substrate interactions. The next section proposes an implementation of graphene on an engineered substrate to control strain distribution.

## 2.3 ENGINEERING STRAIN WITH GRAPHENE

Although we have developed methods to grow graphene in large areas and transfer them to form various hetero-structures as shown in previous sections, there is always the presence of wrinkles as shown in figure 2.9. Such wrinkles are unwanted as they affect the properties of graphene such as its electrical [49], thermal [50] and mechanical [51] properties. They also generate uniaxial stress in the graphene [52].

One of the ways to overcome these problems is by suspending graphene which also prevents doping [53]. However suspended graphene membranes can also contain ripples [54–56] and generate strain in overall structure [50, 57–59]. This is one of the primary reason why size of suspended graphene is limited to around  $10\text{--}150\ \mu\text{m}^2$ . In the following sections we show a novel method of producing graphene with minimum strain, doping and with a priori unlimited area of suspension [60–64]. Also we develop a novel dry lithography technique by which we are able to deposit electrodes on the suspended graphene without using any liquid resist.

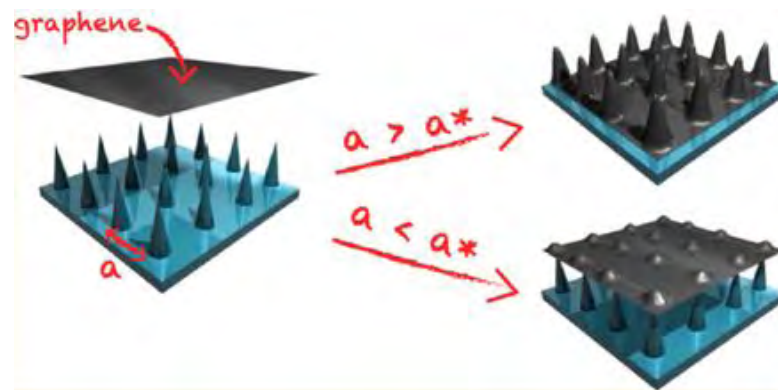


Figure 2.17: Principle of suspending graphene with pillars. "a" is the distance between the pillars which plays a role in the suspension of graphene. Above a critical distance "a\*", graphene collapses onto the pillars while below it, graphene remains fully suspended. (Artist view by Antoine RESERBAT-PLANTEY, Institut Néel)

The principle of the suspending large-area graphene is shown in figure 2.17. The process of fabricating the substrates starts with flat wafers made from doped Si with 500 nm  $\text{SiO}_2$  dielectric. The silica is then patterned using e-beam lithography followed by deep radiative ion etching (RIE) to obtain square network of pillars. The height of pillars is kept around 260 nm with a base of around 100 nm diameter and sharp top. For all the experiments, size of the pillars remains same while the distance between pillars are varied.

Graphene is deposited on these pillars using liquid transfer method and the behavior of graphene is observed with varying distance between the pillars. Transferring graphene in corrugated substrate could be more challenging as any water molecules trapped between substrate and suspended graphene will lead to turbulence when sample is dipped in acetone to remove PMMA. So drying the sample for longer time is necessary.

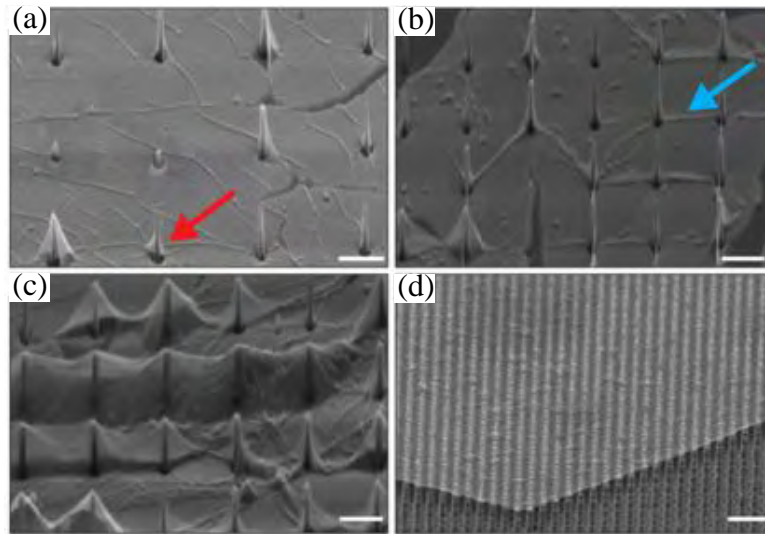


Figure 2.18: Graphene deposited on corrugated substrate with decreasing distance between pillars. Distance between pillars are (a) 2.3 (b) 1.5 (c) 1.4 (d) 0.25  $\mu\text{m}$ . The red arrow points towards locally suspended graphene in (a) while the blue points at ripple formation between pillars. Scale bars lengths are 2  $\mu\text{m}$ . The pillared silica substrate was fabricated in collaboration with Sophie GUÉRON and H el ene BOUCHIAT, LPN, Marcoussis and LPS, Orsay, France

Figure 2.18 shows the scanning electron micrographs of graphene deposited on pillars of increasing density from (a) to (d).

1. In figure 2.18(a), the distance between pillars is so large (more than 1.5  $\mu\text{m}$ ) that the ripples created by individual pillars do not extend to each other and rather develop isotropically from the pillar. Some of the ripples that can be seen at the bottom of the pillars exist probably due to imperfection in the transfer process on corrugated surface. The red arrow points towards locally suspended graphene around the pillar.
2. In figure 2.18(b), the distance between bars pillars is 1.5  $\mu\text{m}$ , and the ripples formed between pillars start to connect each other. There seems to be a preferential direction of ripple formation i.e. the ripples either connect to first or second neighbors as pointed by blue arrow.
3. In figure 2.18(c), the distance between pillars is slightly less than in (b) at 1.4  $\mu\text{m}$ . Graphene is partially suspended and forms ripples along first neighbor directions.



It seems that the formation of ripples is driven along certain directions thus creating domains of self-organized ripples.

4. In figure 2.18(d), the pillar distance dramatically decreased to less than  $0.25 \mu\text{m}$  and graphene is fully suspended over a large area. The area that can be suspended is limited by the size of graphene and area of the pillared-surface.

From these figures, we observe that we can control the graphene/substrate interaction so as to be in a fully collapsed / organized ripples / full suspended regime at will. This opens the possibility to engineer strain in macroscopic graphene. Next subsections address strain in the different observed regimes.

### 2.3.1 Strain in self-assembled network of ripples

Raman spectroscopy is an effective, non-invasive tool to measure strain and doping in graphene systems. We have used Raman mapping to investigate the ripples created by the pillars in figure 2.18(c). In the intensity mapping of the G and 2D peaks in figure 2.19(a) and (c), we are able to observe the lines with alternate high and low intensity. The lines correspond to ripples along pillars formed by graphene.

The difference in intensity in top and bottom of the ripple is due to interference effect: the amount of signal enhanced due to interference from the Si substrate depends on the height of the dielectric ( $\text{SiO}_2$ ) above it as it can be seen in figure 2.19(a). In our case the top and bottom of pillars have a height of 500 nm and 260 nm of  $\text{SiO}_2$  respectively, therefore the Raman signal from graphene on bottom was enhanced while that from graphene on top was diminished according to [65]. For suspended graphene, the dielectrics to consider is a layer of  $\text{SiO}_2$  and second layer of air/graphene that modifies somehow the simulation but leads to similar interference effect. The blue and green spots show the enhancement from top and bottom of pillars respectively in figure 2.19(a). Due to such difference of enhancement of the signal, we are able to observe different domains of ripple orientation as marked by the blue arrow which shows 1st order domain while green arrow shows 2nd order domains. The order of the domains is determined compared to the position of the pillars which can be mapped in the Si intensity map in figure 2.19(b), where the bright points represent the pillars. The different domains in this map are graphene grains which are torn at the boundaries due to strain. The Si intensity is higher at the boundary due to absence of 2.3% absorbance of light by graphene.

We can know about the strain in these system using the frequency mapping of G peak as shown in figure 2.19(d). The top of the ripple have a higher frequency than the bottom part by an difference of  $\Delta\omega_G = 2.8 \text{ cm}^{-1}$ . As shown in figure 2.20(c), the change in frequency of G peak is  $10.8 \text{ cm}^{-1}/\%$  strain. Here we only consider  $G^+$  peak since at

low strain the G peak does not split. The Grüneisen parameter which describes the effect of volume change on vibrational properties of a crystal is given by

$$\gamma_{E_{2g}} = -\frac{1}{\omega_{E_{2g}}^0} \frac{\partial \omega_{E_{2g}}^h}{\partial \varepsilon_h} \quad (1)$$

where  $\varepsilon_h = \varepsilon_{ll} + \varepsilon_{tt}$  is the hydrostatic component of the uniaxial strain with  $l$  and  $t$  representing the longitudinal and transverse components.  $\omega_{E_{2g}}^0$  is the frequency of the peak without strain. The shear deformation potential  $\beta_{E_{2g}}$  is defined by

$$\beta_{E_{2g}} = \frac{1}{\omega_{E_{2g}}^0} \frac{\partial \omega_{E_{2g}}^s}{\partial \varepsilon_s} \quad (2)$$

where  $\varepsilon_s = \varepsilon_{ll} - \varepsilon_{tt}$  is the shear component of the uniaxial strain. The solution to the secular equation is given by

$$\Delta\omega_{E_{2g}}^{\pm} = \Delta\omega_{E_{2g}}^h \pm \frac{1}{2}\Delta\omega_{E_{2g}}^s \quad (3)$$

where  $\Delta\omega_{E_{2g}}^h = \Delta\omega_{E_{G^+}}$  and  $\Delta\omega_{E_{2g}}^s = \Delta\omega_{E_{G^-}}$  are the shifts of frequency due to hydrostatic and shear component of strain respectively. The strain in graphene splits the G peak of graphene in two parts. One along the direction of strain ( $G^-$ ) and one transverse to the axis of curvature ( $G^+$ ). As the  $sp^2$  bonds increase in length due to strain, the C-C vibration softens leading to decrease in frequency. Therefore frequency of  $G^-$  decreases faster than that of  $G^+$ . The overall shift in frequency is given by

$$\Delta\omega_{E_{2g}}^{\pm} = -\omega_{E_{2g}}^0 \gamma_{E_{2g}} (\varepsilon_{ll} + \varepsilon_{tt}) \pm \frac{1}{2} \omega_{E_{2g}}^0 \beta_{E_{2g}} (\varepsilon_{ll} - \varepsilon_{tt}) \quad (4)$$

In case of uniaxial strain  $\varepsilon_{ll} = \varepsilon$  and  $\varepsilon_{tt} = \nu\varepsilon$  where  $\nu$  is the Poisson's ratio which is taken to be 0.13 by Mohiuddin et al in [66]. They found the values of  $\beta_{E_{2g}} = 0.99$  and  $\gamma_{E_{2g}} = 1.99$ . Putting these value in equation (4), it was calculated  $\frac{\partial \omega_{G^+}}{\partial \varepsilon} \approx 18.6 \text{ cm}^{-1}/\%$  and  $\frac{\partial \omega_{G^-}}{\partial \varepsilon} \approx 36.4 \text{ cm}^{-1}/\%$ . Taking into account the experimental conditions, the values were adjusted to  $\frac{\partial \omega_{G^+}}{\partial \varepsilon} \approx 10.8 \text{ cm}^{-1}/\%$  and  $\frac{\partial \omega_{G^-}}{\partial \varepsilon} \approx 31.7 \text{ cm}^{-1}/\%$  from figure 2.20(c). Therefore a  $\Delta\omega_G = 2.8 \text{ cm}^{-1}$  corresponds to a strain of 0.2% according to ref [66, 67]. However the change in frequency is affected not only by the strain but also by doping due to substrate and the contribution of each could be difficult to decipher.

In order to qualitatively understand the effect of doping from substrates, we transferred our CVD graphene on Si/SiO<sub>2</sub> substrate. In general, we have observed that after

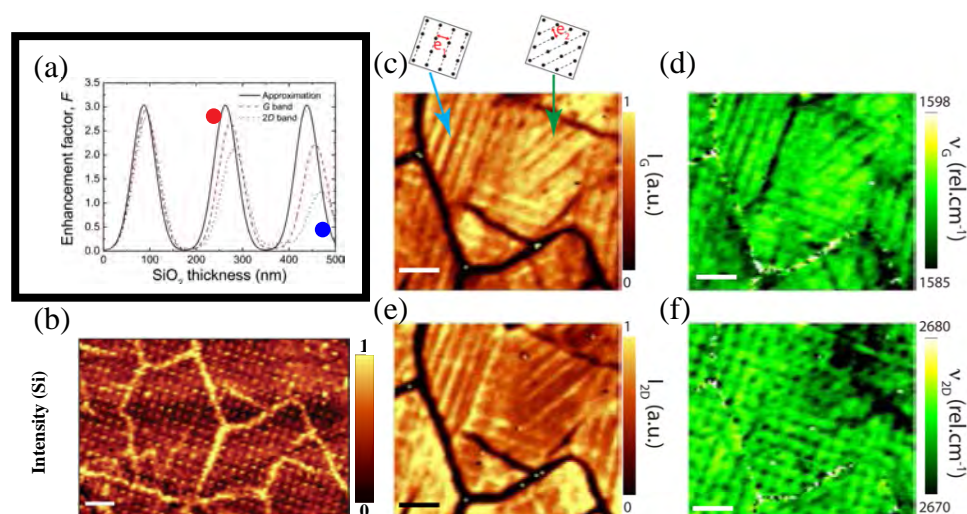


Figure 2.19: Mapping graphene ripples using Raman spectroscopy. (a) Enhancement of Raman signal of graphene depending on the thickness of  $\text{SiO}_2$  [65]. The red and blue points show the enhancement factor of signal corresponding to bottom and top of pillars. (b) Raman Si intensity mapping of graphene on corrugated surface. The position of the pillars can be located by the bright points and graphene grain boundaries are seen as bright lines separating poly-crystalline graphene. (c) G peak intensity (d) G peak position (e) 2D peak intensity and (f) 2D position are the Raman spectroscopy mappings of suspended graphene with ripples as shown in figure 2.18(c). In (c), the blue and green arrows point towards grains with 1st and 2nd neighbor ripple formation of graphene. (Raman mappings adapted from [60])

the transfer, graphene becomes hole-doped as can be seen from figure 2.20(a). The measurement of resistivity of our CVD graphene after transferring onto Si/ $\text{SiO}_2$  substrate shows the Dirac peak corresponding to charge neutrality point falls in the positive back-gate range which means that the Fermi level is below the charge neutrality point in the absence of gate voltage. In other words, graphene is usually hole-doped in our case.

According to ref [68], on doping the graphene with holes, the frequency of the 2D band increases as pointed by the red arrow in figure 2.20(b). This would mean that graphene on top of pillars, in the frequency mapping of 2D peak, should appear as bright points (higher frequency). However the center of the pillars are shown by dark points or lower frequency in figure 2.19(d). This means that the strain experienced by graphene, as calculated from shift of G peak, is much higher than 0.2% such that it offsets increase in frequency due to doping. Simultaneously the strain lowers the position of 2D peak as

shown by green arrow in figure 2.20(b). The observed lowering of frequency proves that the effect from strain dominates.

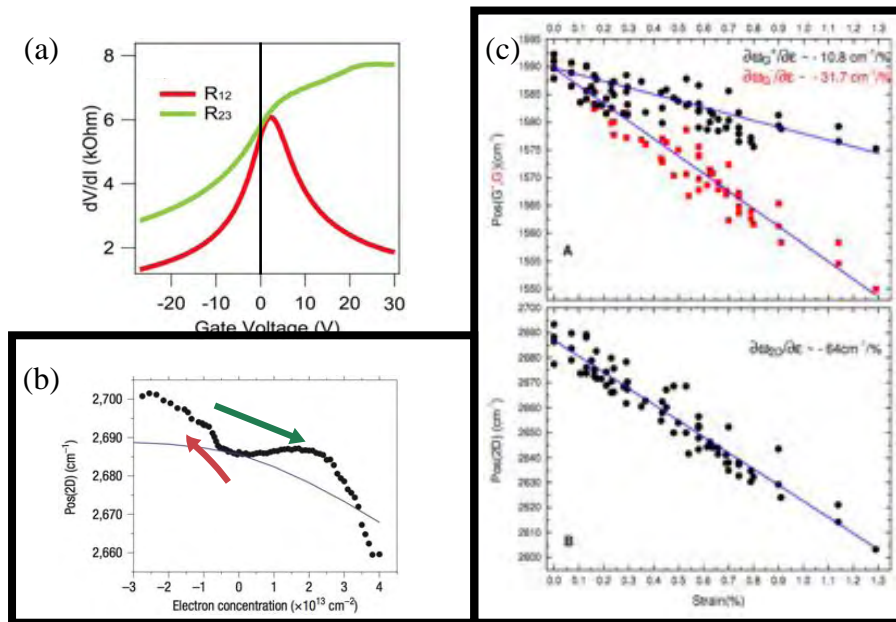


Figure 2.20: Effect of doping and strain on graphene. (a) Differential four probe resistance from pure monolayer graphene (red curve) and with multilayer layer patch in the electron flow path (green curve). Black line corresponds to 0 Volts (adapted from ref [16]). (b) Position of 2D peak as function of doping (adapted from [68]). (c) Positions of the  $G^+$  and  $G^-$  and 2D peaks, as a function of uniaxial strain. The lines are linear fits to the data. The slopes of the fitting lines are also indicated. (Adapted from [66]).

Another reason for higher strain in ripples in graphene is that the laser spot-size (300 nm) is around six times the size of ripples which was found to be around 40-50 nm from the SEM images, hence the spectra measured at each spot of laser beam is an average of a larger area compared to ripple. A high value of strain at the ripples and specially around graphene on the pillars is expected since weight of the ripple is balanced by the graphene on pointed pillars. It would be interesting to measure electronic transport in self-organized rippled graphene as dramatic change is expected for transport perpendicular and parallel to ripples [49].

The SEM image of fully suspended graphene can be seen for  $a < a^*$  in figure 2.21(a) and (b). In (a), we can also observe graphene which is supported on flat SiO<sub>2</sub> and ramps towards full suspension. The supported graphene has lot of puddles probably due to molecules trapped under it or uneven surface of SiO<sub>2</sub>. These could act as scattering

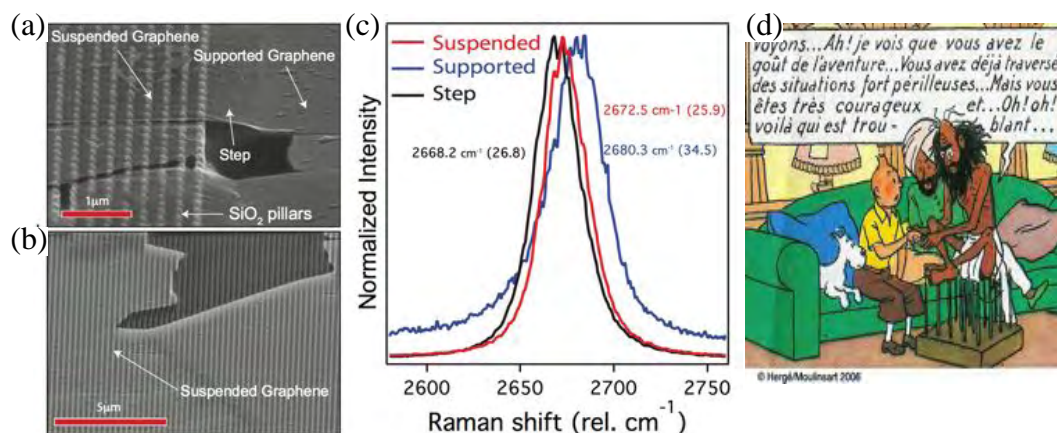


Figure 2.21: Description of supported and suspended graphene. (a) and (b) SEM micrograph of fully suspended graphene on pillars with distance between pillars "a" = 250 nm (Scale bars represent 1 μm). In (a) we also observe supported graphene on flat SiO<sub>2</sub>, ramp of graphene at the boundary and tears in graphene when it is suspended. (c) Raman spectra of graphene at suspended, supported and ramp portion in (a). (d) Fakir sitting on pillar/nailed surface as an illustration of our samples [69].

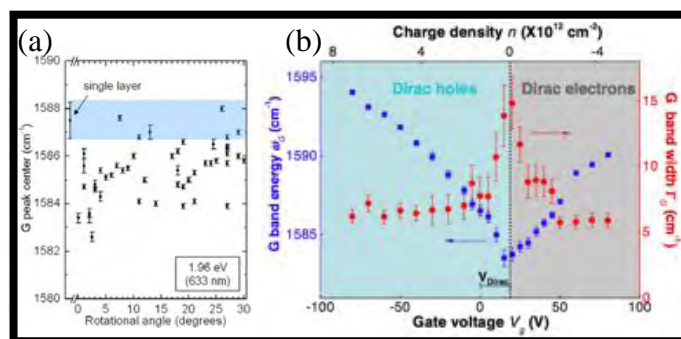


Figure 2.22: Influence of doping in G mode. The blue region in (a) shows the position of G peak of CVD graphene suspended in TEM grid. (the rest of data belong to rotated bilayer graphene) ( figure adapted from [38]). (b) Change in frequency (blue squares) and FWHM (red circles) of G peak with application of electrostatic field using gate voltage ( figure adapted from [70])

points for electrons during transport measurements. On the other hand, graphene on pillars appears to be much flatter. The Raman spectra of these different regions are shown in figure 2.21(c). There is a frequency downshift of  $\Delta\omega_G = -11.9$  cm<sup>-1</sup>, 1596.4

$\text{cm}^{-1}$  to  $1584.5 \text{ cm}^{-1}$ , from supported to suspended region. This shift is due to removal of electrostatic doping of the substrate and a small contribution from strain.

In order to understand their contribution, we study the effect of each of them separately. Figure 2.22(a) shows position of the G peak of suspended CVD graphene which is undoped. The position varies from  $1586.8$  to  $1588.2 \text{ cm}^{-1}$  which are highlighted in blue region [38]. So in an ideal case with no strain in graphene, frequency of G peak should be around  $1587 \text{ cm}^{-1}$  Figure 2.22(b) shows the effect electrostatic doping on Raman G peak of exfoliated graphene. As we move away from the charge neutrality point, frequency of G peak increases while the FWHM decreases [70].

We can roughly assume that reduction of frequency due to doping is around  $9.4 \text{ cm}^{-1}$  ( $1596.4 \text{ cm}^{-1}$  to  $1587 \text{ cm}^{-1}$ ). In our case, the peak from graphene on pillars shows  $1584.5 \text{ cm}^{-1}$ . This extra reduction of  $2.5 \text{ cm}^{-1}$  ( $1587 \text{ cm}^{-1}$  to  $1584.5 \text{ cm}^{-1}$ ) in frequency corresponds to strain of 0.2%. The increase in FWHM from supported ( $10.9 \text{ cm}^{-1}$ ) to suspended graphene ( $13.9 \text{ cm}^{-1}$ ) proves that we have moved from doped to undoped graphene.

The ramp of graphene is expected to have the higher strain. It can be analogically explained from figure 2.21(d) where a fakir is standing on pillars (nails). He is able to stand since the strain is greatly reduced due to distribution on the closely spaced nails over his whole sitting surface. However he will not be able to stand on the ramp, as his weight will now be distributed on less surface thus creating a large strain on his feet. Similarly there is frequency downshift of  $\Delta\omega_G = -3.1 \text{ cm}^{-1}$  from suspended to ramp graphene which is due to excess strain of around 0.3% compared to suspended graphene considering G+ peak frequency changes by  $-10.8 \text{ cm}^{-1}/\%$  from figure 2.20(c).

Earlier we mentioned that the strain in graphene around pillars, whose distance between them are higher than critical distance ( $a^*$ ), is supposed to much higher than 0.2%. If we assume that the change in the Fermi level by doping effect by the pillars is same as flat surface in figure 2.21(a), then change in frequency of G peak, without strain, would be around  $1596 \text{ cm}^{-1}$ . However the position of the peak was found to be around  $1586 \text{ cm}^{-1}$ . This downward shift of around  $10 \text{ cm}^{-1}$  is caused by strain experienced by graphene on the pillars which is around 1%. Therefore we can conclude that fully suspended graphene experiences much less strain compared to ripples of graphene. With suspended graphene we are able to access its intrinsic properties therefore the next step would be to make devices out of it.

### 2.3.2 Differentiating strain and doping

Strain and doping affects of the Raman modes but rate of shift of frequency is different therefore Lee *at al* have been able to differentiate these effects by plotting the frequency

of 2D and G as shown in figure 2.23(a) [71]. They have assumed that for a non-doped and non-strained graphene, the frequency of G and 2D mode would be 1581.6 and 2669.94  $\text{cm}^{-1}$  respectively corresponding to their experimental data from scotch tape exfoliated graphene. If in this mapping the points move along the pink lines with a slope of 2.2, then the effect is due to strain. The type of the strain (compression or expansion) dictates direction of the plot along the pink lines. This kind of mapping is valid only for hole doping and as move away from the **O** point along the black lines with slope of 0.7, the hole doping of the sample increases. For example, for a spectra given by a point **P**, we can calculate the doping level by moving along the black line and the strain effect by moving along the pink line.

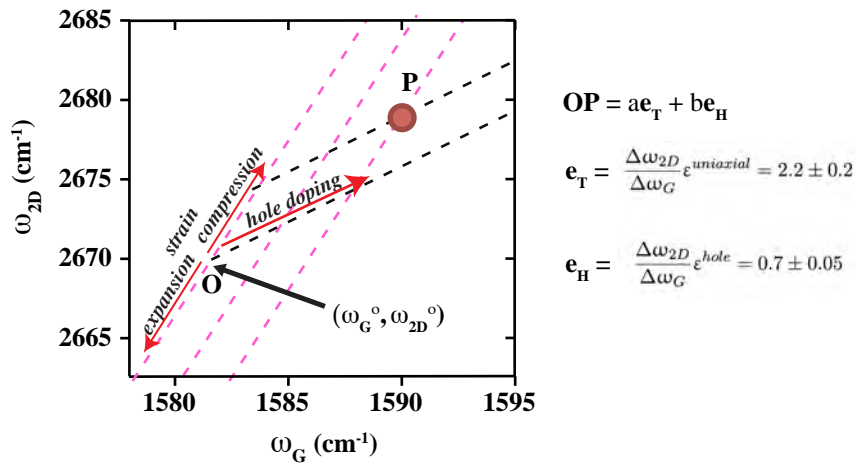


Figure 2.23: Differentiating the strain and doping effect in graphene. **O** gives the point where graphene is non-doped and non-strained. The pink lines show change in frequency of Raman modes due to strain while the black lines correspond to doping effect. (figure adapted from [71])

In order to have deep understanding of effect of the substrate and suspended graphene, we make a line scan across the supported, ramp and suspended graphene as shown in figure 2.24(a). The spectra from the line scan were recorded and are plotted in the figure 2.24(b). The dark green arrows show the direction of evolution of spectra as we move from supported (red shades) to ramp (green shades) to supported graphene (blue shades). From the red shades of spots, we can infer that the supported graphene is compressed and has wide variation of hole-doping. As we move towards the ramp, the strain evolves from compression to expansion leading to decrease in frequency of G and 2D mode. At the same time, the doping level decreases due to de-coupling from the

substrate. In the fully suspended region on pillars, graphene seems to have minimum doping while having a compressive strain around 0.08%.

From the above discussion, we have been able to show in corrugated substrate, hole-doping is minimum as the area of contact between pillars and graphene is less than 5% and strain due to suspension is around 0.08%. This shows that suspending graphene using arrays of pillars is novel way of suspending large area of graphene.

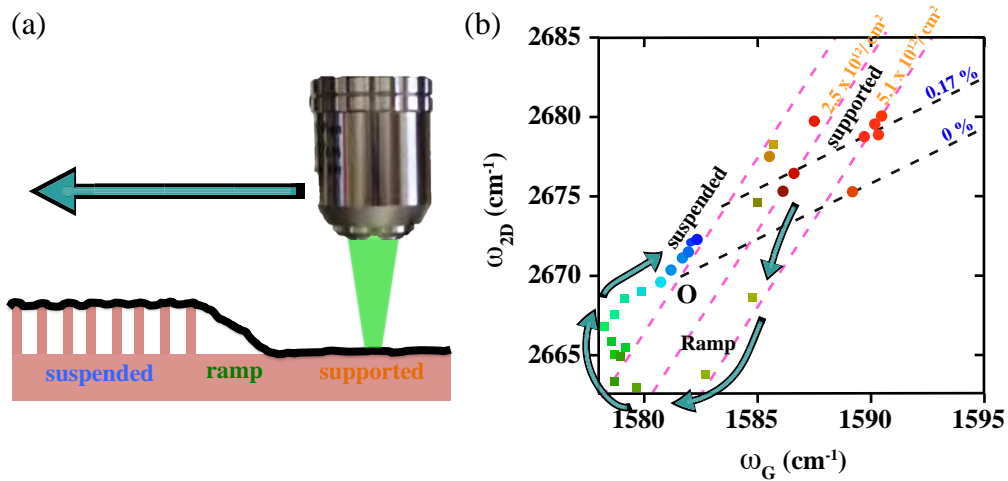


Figure 2.24: Effect of strain and doping in suspended graphene. (a) Raman line scan across supported, ramp and suspended graphene. (b) Frequency plot of 2D vs. G of supported (red shades), ramp (green shades) and suspended graphene (blue shades). The green arrows show direction of scan and evolution of spectra from supported to ramp to suspended graphene.

### 2.3.3 Dry electrode deposition

Though we have suspended graphene over large area, we need to connect it with electrodes to make devices. With a Young's modulus of 1 TPa and very low mass, graphene is an ideal candidate for high quality factor nano-electromechanical systems (NEMS) [72]. Sensing ultra-low density of molecules has become necessary for various purposes and sensors made from graphene have been used to detect gas in sub-part per million level [73–76]. Having large area suspended graphene is an advantage since the area of detection is large. However electrical connections to the suspended graphene is challenging.

Most suspended graphene membranes are fabricated by transferring on a sacrificial resist on which people use classical lithography technique to make electrodes which involves spin-coating liquid resist on the sample, baking and exposing graphene to laser



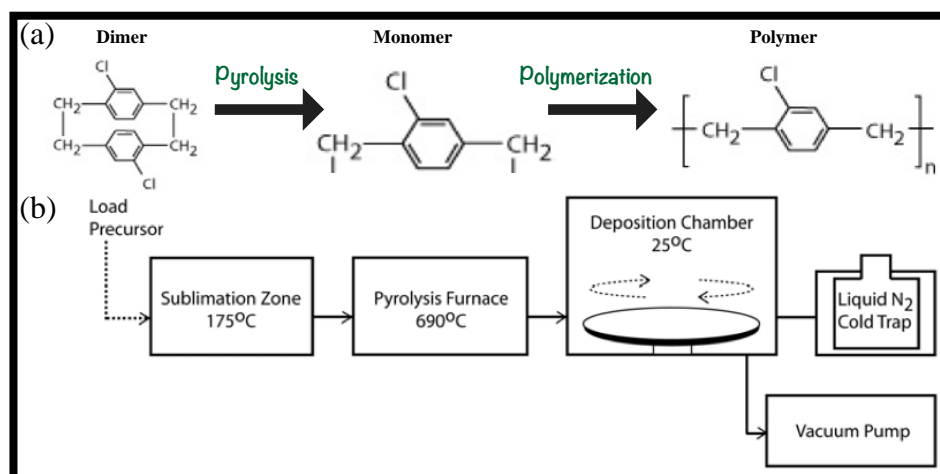


Figure 2.25: Parylene C deposition. (a) Process of pyrolysis of Parylene C to form monomer and then to form polymer in the substrate. (b) Schematic of deposition chamber of Parylene C: sublimation chamber to vaporize the parylene, pyrolysis chamber to form monomers and deposition chamber to polymerize on substrate (figures adapted from [77]). Parylene deposition courtesy Emmanuel ANDRE, Institut Néel

or electron beam and wet removal of the resist [53, 57, 62]. In our case, the graphene is suspended on pillars so any liquid applied on it might remove graphene. Though we managed to suspend graphene without exposing to lithography step to remove the oxide below it but the challenge is to perform resist free evaporation of electrodes on corrugated and fragile surface. We have thus developed a flexible shadow masking technique based on a polymer inspired by Selvarasah *et al* in [78].

Parylene, poly-para-xylylene, is a widely utilized material in the medical and electronic industry for its ability to pin hole free conformal coating and biological compatibility. This has also been used for micro-patterning biomolecular arrays [77, 78] and depositing metal of various patterns at micro scale. Parylene is deposited on to surface using a cold CVD surface. A parylene C molecule along with the polymerization process is shown in figure 2.25(a). These molecules are then vaporized at 175°C in a chamber and injected into pyrolysis chamber at 690°C. Here the molecules dissociate to form monomers. These monomers move into the room temperature deposition chamber and adsorb on the surface of the substrate. They migrate on the surface and chemically react with other monomers to form polymer chains. A schematic of the cold CVD process is shown in figure 2.25(b).

Parylene is deposited on SiO<sub>2</sub> substrate as shown in figure 2.26(a). It can be seen that when it is removed from the substrate it is a thin transparent, easy to handle and flexible

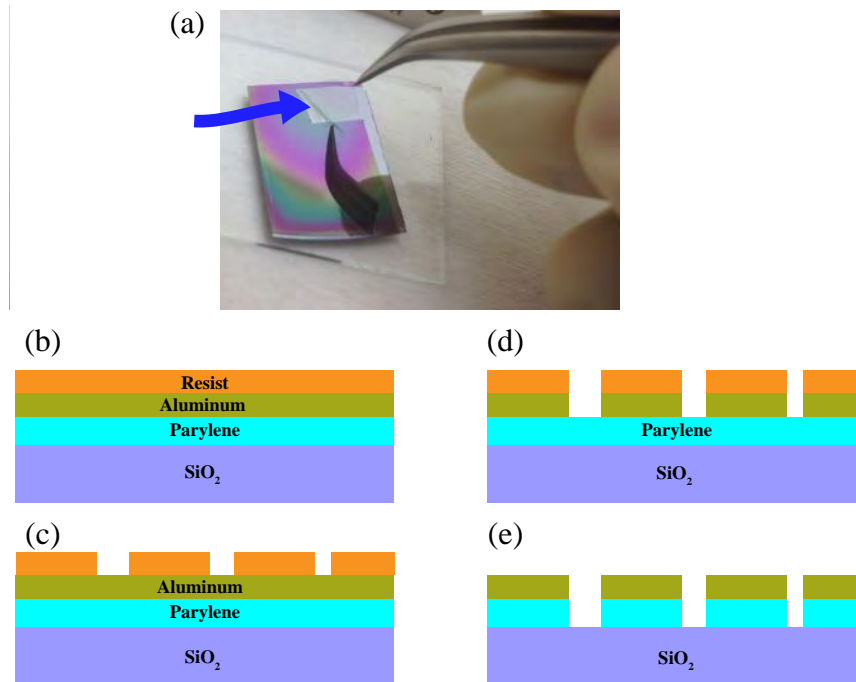


Figure 2.26: Parylene stencil mask fabrication. (a) Optical image of parylene deposited on Si substrate. The blue arrow points to parylene peeled off from the substrate with tweezers. (b) Deposition of resist and aluminum layer on parylene. (c) Laser lithography on resist layer. (d) Removal of aluminum layer with MF<sub>319</sub>. (e) Oxygen plasma etch of parylene through holes created to make mask for electrodes and final aluminum mask removal.

membrane shown with blue arrow in (a). Transparency allows us to align the electrode pattern with a micropositioner on a specific graphene flake seen through the mask and flexibility is useful since it has soft landing on graphene without destroying it.

Equal thickness fringes of reflected light are seen on parylene when it is deposited on Si substrate because parylene deposition is smooth and transparent enough to promote interference effect. Thin layers of around 10nm of aluminum and S1805 resist is then deposited on it figure 2.26(b). On the resist we perform a laser lithography step to pattern contacts which are specifically designed for the graphene grains pre-located by optical microscopy figure 2.26(c). Through these holes the aluminum layer is dissolved using MF<sub>319</sub> figure 2.26(d) to obtain the mask. Then the sample is exposed to oxygen plasma to create mask for electrodes on the parylene figure 2.26(e). Thereafter the aluminum and resist layers are removed.

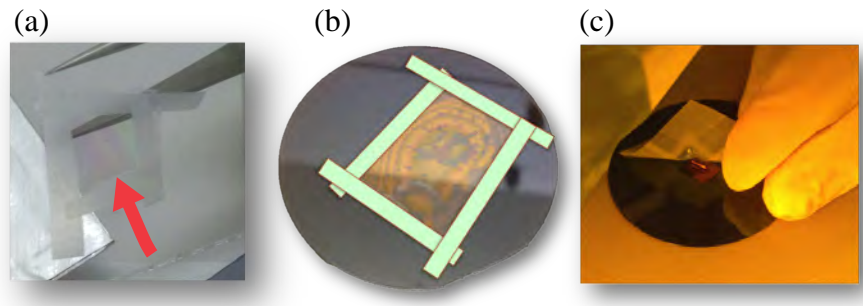


Figure 2.27: Dry electrode deposition on graphene membrane. (a) Parylene mask supported by scotch tape. The red arrow points towards the transparent mask. (b) The sample with graphene is stuck to a Si substrate used as a holder. Parylene mask is aligned over the graphene flake and gently dropped on it for electrode evaporation. (c) Dry lift-off process after deposition of electrodes

After the lithography the mask can be easily removed from the Si substrate by simply peeling it off. In order to avoid folding of the mask, it is framed with scotch tape at its border as shown in figure 2.27(a). It is mounted on a standard aligner where it is positioned over a specific flake. Then the mask is aligned over it and gently dropped on the graphene flake. The scotch tape sticks to Si substrate to avoid movement of the mask shown in figure 2.27(b). 5 nm Ti and 100 nm Au are deposited over it in an electron gun metal evaporator system. After the deposition, the mask is removed as shown in figure 2.27(c). This way we have completely removed any kind of liquid in the lithography process.

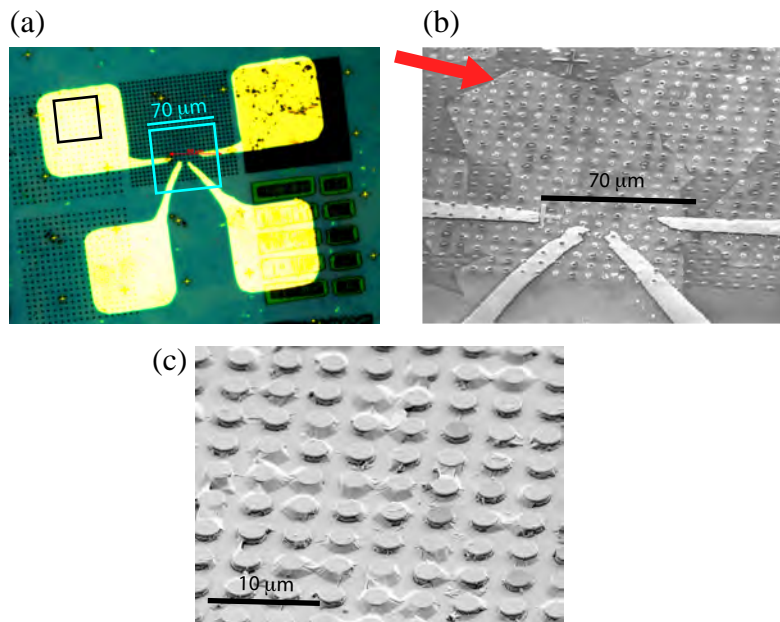


Figure 2.28: Demonstration of the use of transfer stencil mask. (a) Optical image of four electrodes deposited over graphene on corrugated substrate. (b) SEM image of the light blue square in (a). The red arrow points towards graphene. (c) SEM image of black square in (a)

Figure 2.28(a) shows optical image of the corrugated substrate after the deposition of the four electrodes. The regular arrays of dots are pillars on which graphene has been deposited. The distance between the pillars are different which gives different contrast: the darker the contrast, the closer are pillars. A SEM image of zoomed view of the electrodes (light blue square) is shown in figure 2.28(b). Here we can observe four electrodes which are spaced by 50 μm on top a graphene flake and are visible in SEM image with a lighter contrast pointed by red arrow. A zoomed SEM image of the black square in (a) is shown in figure 2.28(c). It can be seen that the metal electrodes are deposited on top of graphene which is able to sustain the weight of the metals without collapsing. In this sample the pillars are not pointed as discussed before but have flat surface and graphene is only suspended on the sides of the pillars. Work is in progress to apply this technique to fully suspended graphene.

Connecting fully suspended graphene would also allow to create original nano-electromechanical systems with an electrostatic actuation as was realized from our CVD graphene as shown below.

### 2.3.4 Other suspended devices

Suspended graphene can be used to study nano-electromechanical system (NEMS). Figure 2.29(a), shows a SEM image of graphene that has been deposited on well etched from  $\text{SiO}_2$  substrate. When such a device is kept in vacuum it inflates as shown in the 3D atomic force microscopy (AFM) image in figure 2.29(b) and (c). This is because the pressure in the trench is higher than outside which leads to the inflation and also proves that graphene is leak-proof to air molecules. Such membranes are also connected with electrodes to study mechanical behavior under electrostatic excitation. (PhD thesis by Cornelia SCHWARZ [79]).

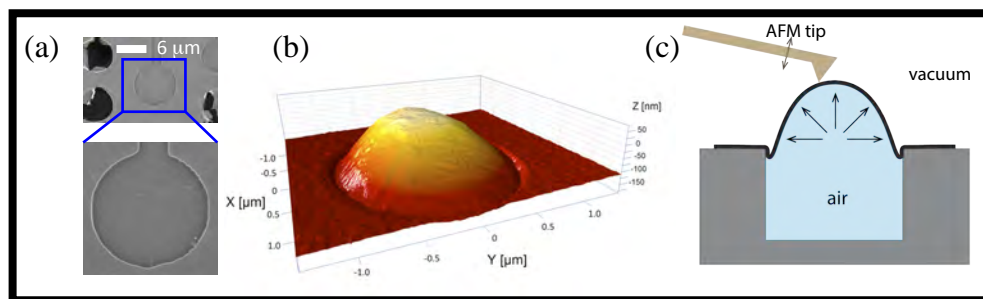


Figure 2.29: Graphene inflated diaphragm. (a) SEM image of our CVD graphene on  $\text{SiO}_2$  trench. A zoomed image of the successful transfer of graphene. (b) AFM image of graphene suspended over a trench in vacuum conditions (c) Schematic of suspended inflated graphene in vacuum. (Image © Cornelia SCHWARZ, PhD student, Institut Néel)

This section deals with graphene on corrugated substrates and has highlighted the strong influence of the silicon substrate on doping and strain in graphene. The next section investigates the role of the substrate on deposited graphene and shows how the latter can be chosen for specific applications.

## 2.4 GRAPHENE ON INSULATORS

In order to implement graphene devices, it is of great importance to provide easy to handle graphene deposited on a processable surface. Still the presence of a substrate shall not be detrimental to its properties. In this section, we show first the influence of the catalytic substrate on graphene's properties. Then we focus on microelectronic compatible substrates for graphene transfer, and finally on applications of graphene as an active substrate for devices.

## 2.4.1 Graphene on BN stack

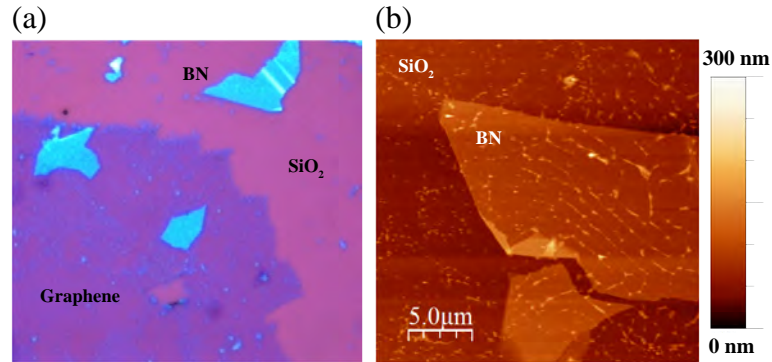


Figure 2.30: CVD graphene transferred on BN by liquid transfer method. (a) Optical (b) AFM image of graphene on BN. (AFM image by Mira BARAKET, Institut Néel)

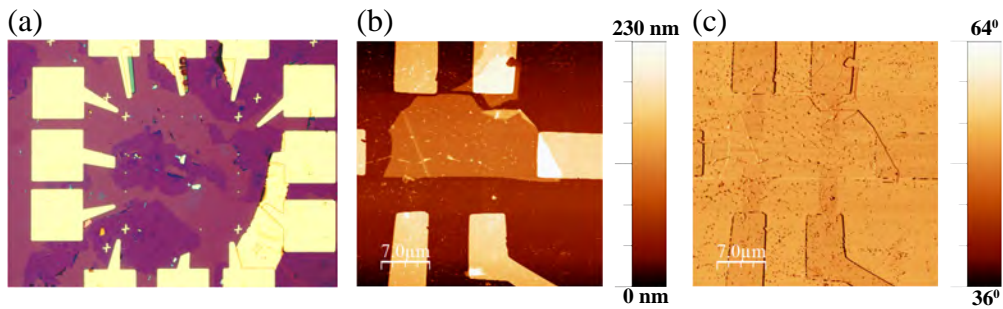


Figure 2.31: Nanofabrication of graphene on BN devices. (a)

$$R = R_c + \frac{L}{W\mu\sqrt{(n_0e)^2 + [7.56 \times 10^{10}(V_g - V_{NP})]^2}} \quad (5)$$

BN is indeed the ideal substrate for high performance graphene-based electronic devices. When considering mechanical applications of graphene, other materials have to be considered such as diamond.

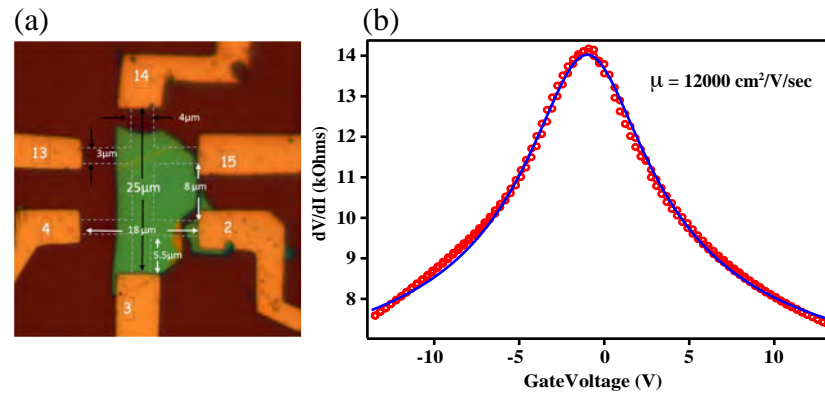


Figure 2.32: Graphene on BN Hall bar characteristics. (a)

#### 2.4.2 Graphene on diamond anvil cells

Considering the outstanding mechanical properties of graphene, it has attracted much interest from the high pressure community to investigate 2-dimensional high in-plane stiffness. However, most high pressure studies have been performed for graphene deposited on different kinds of substrates, the high pressure behavior of which get convoluted with the graphene one. In order to measure optical phonons of graphene under high pressure, it was transferred to a diamond anvil of 300 μm diameter as shown in figure 2.33(a) in order to remove any intermediate substrate. Thereafter another diamond anvil was placed on top to apply pressure upto 13 GPa and Raman spectra were measured in-situ. The Raman spectra of graphene without applying pressure is shown in figure 2.33(b). The high intensity Raman peak for diamond is seen at 1331.9 cm<sup>-1</sup>, while the lower intensity graphene bands are observed at 1584.3 cm<sup>-1</sup> (G band) and at 2637.5 cm<sup>-1</sup> (2D band). On applying pressure on the system, the G band shifts to higher frequency as shown in figure 2.33(c) and its FWHM increases. The shift in the frequency is plotted in figure 2.33(d). The high pressure measurements were done by Gardenia PINHEIRO, Prof. Alfonso SAN-MIGUEL at Institute Lumière Matière, Lyon.

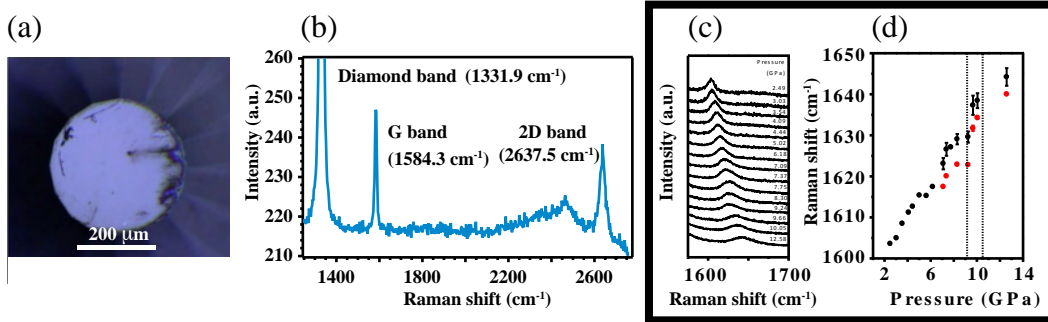


Figure 2.33: Graphene on diamond anvil for high pressure measurements. (a) Optical image of graphene transferred on diamond anvil of 300  $\mu\text{m}$  diameter. (b) Raman spectra of graphene on diamond. (c) Evolution of G band with increasing pressure from top to bottom. (d) Position of G band with increasing pressure on graphene. (high pressure measurements by Gardenia PINHEIRO, Alfonso SAN-MIGUEL, Institute Lumière Matière, Lyon).

The previous sections are proofs of concepts of optimized substrates for graphene applications. However, for upscaling graphene integration, it is mandatory to provide large scale, easy to produce graphene on insulator substrates for lower technological applications.

### 2.4.3 Large area transfer

Till now we have shown how graphene can be transferred on Si/SiO<sub>2</sub> substrates in centimeter scale. However there is a need to transfer graphene on any substrate and at larger scale. Therefore we modified our liquid-assisted transfer method in order to perform large graphene transfer on wafer scale as shown in figure 2.34. Though the principle of transfer method remains same, the larger scale adds to the complexities. There are especially two important steps that we cared about.

1. The PMMA coating on graphene needs to be uniform. Non-uniformity of coating results in sinking of graphene + PMMA into the etchant which leads to tearing of the structure.
2. Bubbles of gas are formed during the etching process, although the source is not verified. Removal of these bubbles is necessary for full copper etching and uniform deposition on the target substrate. At this stage we performed manual removal of the gas bubbles. However a straightforward method needs to be developed, such as large scale bubbling separation by electrochemical exfoliation on the copper.



Examples of large area transfer are shown in figure 2.34. Such wafer scale transfer of graphene opens the possibility to use it for industrial applications.

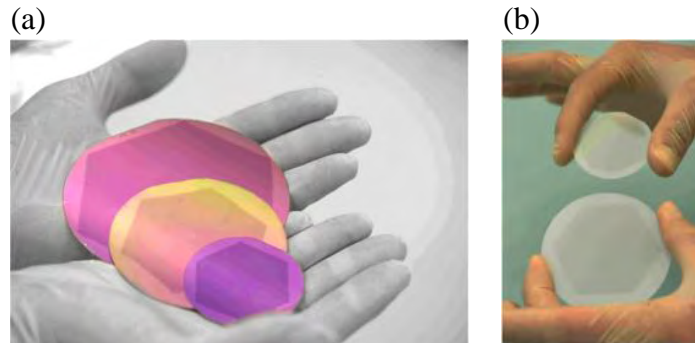


Figure 2.34: Upscaling graphene on wafer transfer. (a) Graphene transferred on 2, 3 and 4 inch Si/SiO<sub>2</sub> wafer. (b) Graphene transferred on 2 and 3 inch sapphire wafer. Note: The graphene is polycrystalline monolayer cut into hexagonal shape for clarity.

These large scale graphene on insulator substrates are of interest to design graphene-based devices taking direct advantage of graphene's properties. Furthermore, one can also use graphene as a substrate that will provide new properties for making devices. In that case, graphene is not the core of the device function but improves the overall performances of the devices as shown below.

## 2.5 GRAPHENE AS ACTIVE COMPONENT

We will focus now on using graphene as an exposed 2-D surface coupled to an active element. In this case, the surface of graphene will be used as a platform to promote a function such as light emission or bioelectronic transduction.

### 2.5.1 Graphene as transparent conducting electrode

One of the most promising application of graphene is its use as a transparent conducting electrode to replace the brittle indium tin oxide (ITO). In this context, one easily thinks about photovoltaics application, but any kind of light emitter/detector is in principle concerned. As a proof of concept, we have collaborated with INAC-CEA to implement graphene artificial stacks as the top electrode of nitride heterostructure blue LEDs.

In general, Ni/Au is used as electrodes to inject electrons into the GaN quantum LED. Though it is an efficient injector of the electrons, it blocks the blue light that is emitted by

the LED. Therefore mesh of electrode have been used to minimize this effect. Graphene positions itself ideally since it is a semi-metal and transparent. Four layers of CVD graphene were transferred onto the quantum well LED as shown in the schematic figure 2.35(a). In principle we are able to illuminate a wide area of quantum LED. Graphene was deposited on the area marked by black square and around 20 - 30 % of area showed recombination of electron and holes, hence bright illumination, as shown in figure 2.35(b). However not all parts are illuminated since contact between graphene and p-doped GaN layer is not optimized yet. We have tried to make comparison between direct injection from graphene and injection through graphene on top of Ni/Au patches (disks visible on figure 2.35(c)). However light emission seems similar whether Ni/Au pads are present or not below graphene which rules out the point of Schottky barrier adaptation for our low efficiency (at least in the first order). Interestingly the different contrast at the SEM image in figure 2.35(c) are related to light emission: efficient light emission corresponds to high density of dark regions. The whiter regions seem to correspond to bad coupling of the graphene to the substrate, which might be due to trapped species below graphene.

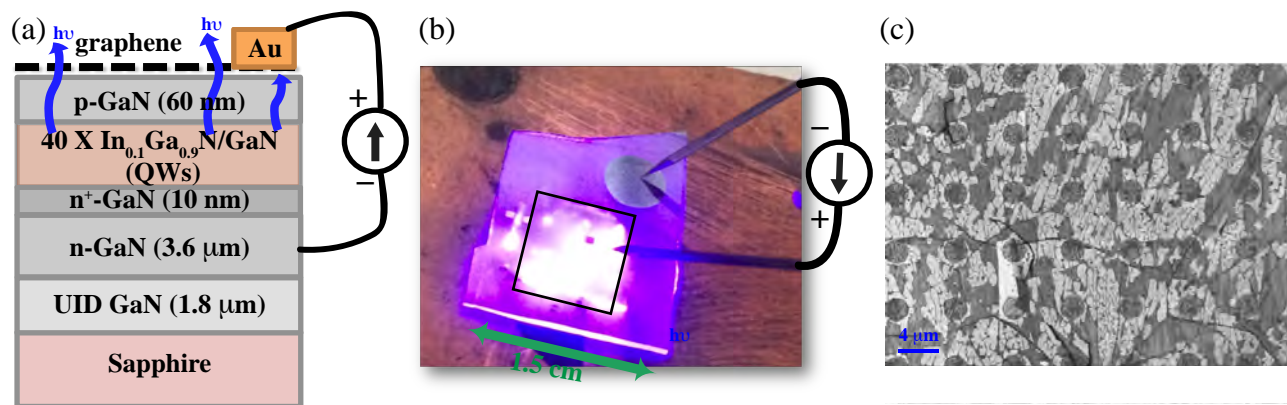


Figure 2.35: Graphene as transparent electrode on LED. (a) Schematic of GaN quantum LED with graphene as electrode. The blue arrows show that light is able to pass through graphene but not through Au electrode. (b) Photo of a working GaN quantum LED with graphene electrode. The black square shows the region where four layers of CVD graphene was transferred. (c) SEM image illustrates the different contrast in graphene deposited in p-doped GaN layer. The round disks are Ni/Au patches. (collaboration: GaN quantum well LEDs were fabricated by Anna MUKHTAROVA *et al* INAC-CEA, Grenoble) [84]

In the case of graphene transparent electrode, graphene is used as one element of the overall structure. However, it does not appear to modify the behavior of the active part

of the device. In the following, graphene is implemented for bioelectronic device and we will show that the overall fabrication of the device is indeed modified by it.

### 2.5.2 *Graphene as substrate for neuron growth*

Graphene also offers an ideal platform for sensing and culturing neural networks. Its biocompatible, soft, and chemically inert nature associated to the lack of dangling bonds offers novel perspectives for direct integration in bioelectric probes. The 2-D electron/-hole gas directly exposed to the cell leads to a high sensitivity and strong coupling to the neurons. Moreover, the possibility to transfer it on transparent and flexible substrates opens the way to a variety of applications for in-vitro studies and in-vivo implants.

At Institut Néel, we investigate our CVD grown monolayer graphene with regard to its biocompatibility and bioelectrical interfacing. We found, that while on any other substrate an adhesive coating (such as poly-L-lysine) is needed to assure neuronal growth in culture, graphene actively promotes the growth even without a coating (figure 2.36(a)). Graphene based devices can be also used for electrical detection of neuronal activity. Neurons are electrically active cells, which process and transmit information through electrical signals, called action potentials (rapid voltage pulses induced by ionic exchange on the cell membrane). Using highly sensitive graphene field effect transistor, these action potentials can be detected in a non-invasive manner through the detection of conductance/current modulation induced by the electrical activity of the cell as shown in figure 2.36(b). The red curve in figure 2.36(c) shows the activity of the neurons. In order to verify the signal, a poison was administered to the neuron which killed the neuron, therefore the blue curve does not show any signal.

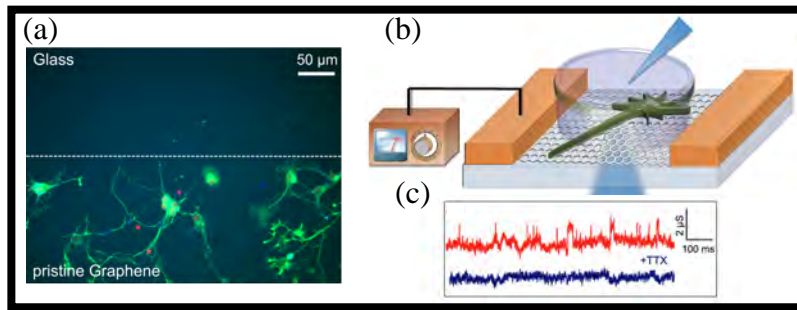


Figure 2.36: Interfacing graphene to neurons: a) Immunofluorescence image of neurons cultured for 4 days on pristine graphene on glass. Neurons preferentially grow on the area covered with graphene. (b) Schematic of graphene field effect transistor (FET) with a neuron on it. (c) Red curve gives electronic readout of active neurons while blue curve gives for dead neurons. (Image © Farida VELIEV, PhD thesis at Institute Néel)

In all this section examples, graphene is used as an active element in devices, both for its transparency and conductivity. We will now show that it is furthermore possible to implement its flexibility into devices in a process compatible way.

## 2.6 GRAPHENE ON FLEXIBLE SUBSTRATE

All the above transfers of graphene have been done on solid substrates but electronic devices which are flexible and stretchable are found to be more versatile. Graphene has emerged as strong candidate for its transparency and flexibility. The optical absorbance of few layers of graphene is found to be lower than traditionally used brittle Indium Tin Oxide (ITO) besides the higher mobility of graphene. Graphene has already found application in flexible optoelectronic devices such as touch screens [22], organic light-emitting diodes [85] and organic photovoltaic devices [86].

Due to flexibility of the substrate, transferring graphene by liquid assisted method becomes challenging. We tried to circumvent the problem by growing the substrate on graphene instead of the transferring process. The schematic is shown below in figure 2.37. After the growth of graphene, we mask one side of copper from polymer deposition. We make a deposition of polymer molecules on the entire surface area. After removing the mask, graphene on the opposite side is removed by oxygen plasma. Thereafter the copper foil is removed using an etchant leaving behind graphene+polymer bilayer. This bilayer can be handled by mechanical tweezers and dried in ambient conditions.

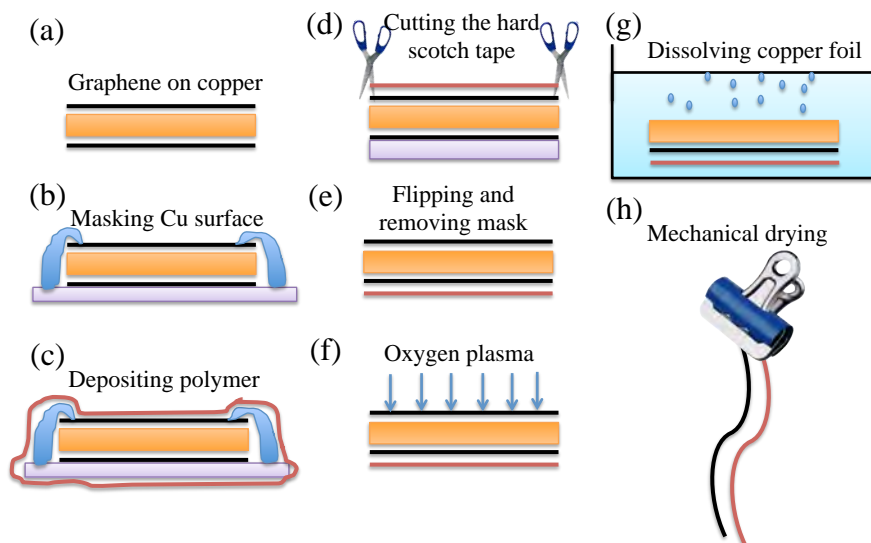


Figure 2.37: Schematic of process flow to transfer graphene on flexible substrate

In this work, graphene has been transferred to polymer membrane upto A4 sheet scale as shown in figure 2.38(a). The material was found to be robust and remains hanging on electrodes as shown in figure 2.38(b). The square resistance is  $\approx 1$  kOhms though the value changes on mechanical folding of graphene. We have found that this technique can be scaled for industrial production. Moreover the technique could be used to make applications based on graphene such as membrane for loud speaker, medical applications and 3-dimensional coating of graphene. The process has be submitted for patent application. (V. ref: 07258-01, N.ref: B13654 FR)

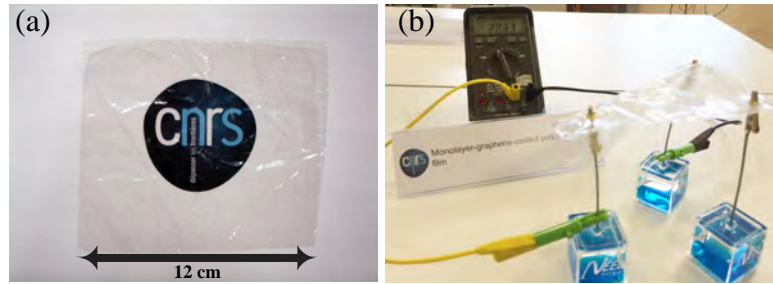


Figure 2.38: Flexible and conducting graphene membrane. (a) A4 scale polymer-graphene transparent membrane. (b) The membrane is suspended on conducting electrodes and resistance is measured with a multimeter. The resistance measurement across diagonal shows 1 kΩ.

Since we have shown that we are able to make high quality graphene and transfer it on different substrates, we will make a comparison of our expertise with two other companies which have launched their products in the market.

## 2.7 COMPARISON WITH OTHER COMPANIES



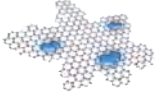
	 Graphenea	 BGT MATERIALS	 Hybrid group
Graphene on copper Max size(cm <sup>2</sup> )	82	60 x 760	20 x 20
Monolayer %	Multi-layer patches	> 95%	100%
Single crystal size(μm)	<10	30 - 200	300
Transmittance	> 97%	> 97%	> 98%
Transferred on Si/SiO <sub>2</sub> Max size (inch)	4	4	4
Mobility cm <sup>2</sup> /V.s	4000(Hall)	2000-4000 (Hall)	5000
I(D)/I(G) ratio	< 5%	< 5%	< 5%
Flexible substrate (size in cm <sup>2</sup> )	PET (82)	PET (20x25)	Polymer (20x20)
Sheet resistance Ohm/sq	580±50	30-800	1,000
Transparency	> 95	85-95	Not calculated

Figure 2.39: Comparison of CVD graphene grown and transferred by Graphenea, BGT materials and our Hybrid group.

Graphenea is Spain-based company while BGT materials is Britain-based company that are one of the major providers of the graphene in the market. In figure 2.39, we make a comparison of different parameters of the graphene-based products with the ones produced by us. In terms of size, graphene produced by these companies are comparable or bigger than our group however we are able to produce perfectly monolayer graphene without multilayer patches which gives a better transmittance and higher mobility. All the three groups have the ability to transfer graphene on 4 inch wafer. From the Raman spectroscopy we found that the D band is almost negligible compared to G and 2D band. This is true for the entire surface of the transferred graphene. Both the companies claim I(D)/I(G) ratio to be less than 5% however this does not hold true for the entire graphene surface as Raman spectroscopy done by our group on their sample show high intensity D band on various places.

Using our novel method to grow flexible substrate on graphene, we have been able to transfer graphene on a larger flexible, transparent substrate compared to others. It can be seen that the sheet resistance of graphene on Parylene (23,000 kOhm) is much higher than that of PET (30-800 Ohm). One of the reason could be that the graphene is doped when it is transferred on PET while it remains un-doped when parylene is deposited on graphene.

## 2.8 CONCLUSION

In this chapter, we have shown a method to overcome two main difficulties to transfer CVD graphene grown on copper foil to form bilayer graphene. The bilayer structure was then probed using Raman spectroscopy which proved that the two layers of artificially transferred graphene was interacting to form bilayer structure. Such interaction allowed us, using Raman mapping, to distinguish between different grains present in the polycrystalline bilayer graphene system. The FWHM and intensity of the 2D peak of graphene was found to be highly sensitive to rotation angle between the two graphene layers, therefore it was used to classify various rotation angles in bilayer graphene. Since the Raman signal varied with the rotation angle, this information was used to prove that the 6-sided graphene crystals are indeed single crystals. There are also octagonal crystals that can be observed during the growth of single crystals. We have proved that these crystals are polycrystalline in nature by transferring them on 6 sided single crystals and identifying individual grains.

With slight modification of the liquid transfer technique, graphene was suspended on corrugated substrate in microscopic scale. We found that if the distance between pillars are high (above 250 nm), ripples of graphene were formed which seemed to force each other to align along certain directions. If the distance between pillars was less than 250 nm, graphene remained fully suspended over a large area. Using Raman spectroscopy, we found that the strain in the suspended graphene was less than 0.2% which makes it useful for various applications. Thereafter a transparent, flexible, soft stencil mask process was developed to deposit electrodes on the fully suspended graphene.

Graphene was utilized as a transparent electrode for quantum well GaN LED cell. Here we found that the injection area of the holes into the cell was greatly increased due to efficient transfer from graphene to p-doped GaN layer. Graphene was also found to be a better substrate to grow neurons compared to glass substrate which makes it useful for electro-optical studies of neurons. The action potentials of neurons was detected using a graphene field effect transistors.



The vibrational behavior of graphene under high pressure in range of giga Pascal was measured by transferring graphene on diamond tips. The shift in Raman bands were measured in-situ while applying pressure.

The transfer method was scaled up to transfer graphene on different and large substrates. We are able to transfer graphene onto 4 inch metal and sapphire substrates. And finally we have developed a novel process of transferring graphene onto flexible substrates in large area which is in the process of being patented.

In this chapter, I addressed how to tailor properties of graphene with its environment. Another approach to tune its intrinsic properties is to engineer directly the structure at the nanoscale level. Next chapter is dedicated to using defects as tailoring agent.

## CONTROLLING FORMATION OF DEFECTS AND DISCRIMINATING THEIR NATURE IN GRAPHENE BY OPTICAL PHONONS

In spite of the advances in growth and fabrication techniques [87], there is yet no industrial production of any such devices exploiting wonderful properties of graphene. One of the main reason for this situation is because many applications such as transistors, gas sensors, nano-composites require modification of graphene properties to adapt to needs of application. In the microelectronics industry the primary need of material is electronic bandgap. The electronic band structure in graphene is such that it has zero bandgap. This means that, although electrons have a high mobility in graphene, their flow cannot be stopped using an electric field unlike in semiconductor materials. Therefore ability to control graphene properties could open a way for applications such as supercapacitors, spintronics etc.

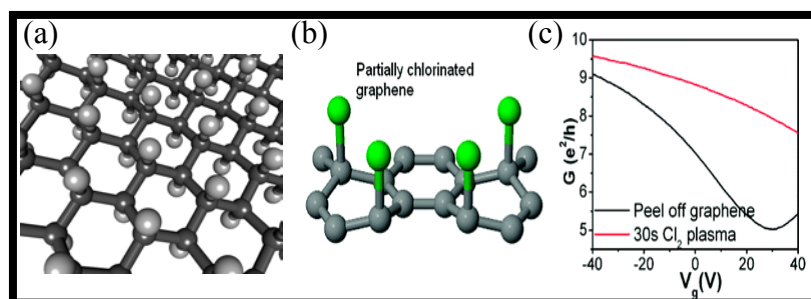


Figure 3.1: Covalently functionalized graphene. (a) Atomic structure of graphene with white and black balls representing hydrogen and carbon respectively (source: wikipedia). (b) Partially chlorinated graphene and (c) change of conductance of graphene on partial chlorination. (adapted from [88])

The key engineer the properties of graphene lies in the ability to alter the honeycomb structure of graphene in a controllable way. Different methods are possible: Functionalization, intercalation, inducing defects etc. Whatever the chosen method the consequences is a strong modification of graphene structure and thus its electronic and vibrational properties. All these effects can be probed efficiently by optical phonons. One of the ways is by functionalizing it with hydrogen on graphene using Ar/H<sub>2</sub> plasma or

RF plasma. An example of such structure is shown in figure 3.1(a) with the white and black balls representing hydrogen and carbon respectively. It is found that depending on the coverage of  $sp^3$  bonded hydrogen, the metallic state can become semi-conducting even insulator state [89–92]. In such structures, researchers also managed to get back the pristine graphene using annealing techniques [93,94]. Halogenation seems to be another option of doping graphene with chlorine, fluorine, iodine or bromine atoms. Due to higher electronegativity of these atoms, graphene is easily doped by covalently bonding with carbon atoms figure 3.1(b). This has been achieved by halogen plasma method or exposing sample to high temperature in presence of halogens [88,95–97]. This would change the  $sp^2$  to  $sp^3$  hybridized carbon and change the periodicity of the lattice structure. Such modification of structure has been found to open a band gap of around 0.4 eV which in turn modifies electron transport properties as shown in figure 3.1(c). [98–101].

Modification of electronic properties can also be found in graphene nano-ribbon (GNR) and quantum dots [102] due to confinement of electrons. It is found that the energy gap increases with decrease in width of GNR [10]. These structures are fabricated using e-beam lithography and etching graphene using oxygen plasma, hence they are limited to electronics industry. Jayeeta *et al* have demonstrated that intrinsic extended defects between graphene grains can act as metallic nanowire at atomic scale [103].

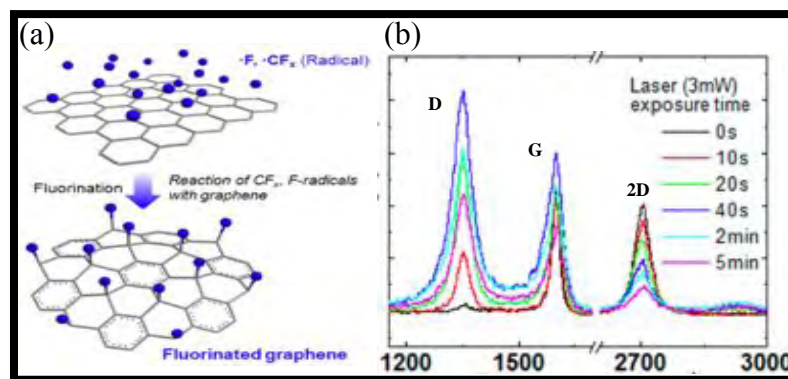


Figure 3.2: Monitoring the grafting of fluorine on graphene. (a) Schematic of effect of fluorination of graphene on the C-C bonds. (b) Evolution of Raman spectra of fluorinated graphene with time. (adapted from [92])

It is also reported that disorder can be induced in graphene lattice structure by using oxygen plasma [104–106]. Disorder changes the lattice structure hence its electrical transport properties are modified. This can be brought about using electron beam radiation in few minutes [107,108] and  $sp^2$  bonds can be broken using soft x-rays possibly opening a new route to nano-structured graphene [109]. Mild oxidation and fluorination creates

$sp^3$  type defect in graphene by covalent bonding of halogen with carbon in graphene lattice. This is shown in figure 3.2(a) where the fluorination of graphene has caused to change the structure of graphene. The hexagonal lattice structure has been distorted by breaking the  $sp^2$  bonds to form  $sp^3$  with fluorine. The effect of breaking of fluorination can be monitored by Raman spectroscopy (see figure 3.2(b)). With increasing in time of fluorination, the intensity of D band increases while that of G and 2D band decreases.

$Ar^+$  ion bombardment does not form  $sp^3$  bonds but creates vacancy-like defects [110–115]. Schematic of such bombardment is shown in figure 3.3(a). The size of the holes depends on the size and speed of particles. High resolution transmission image of bombarded graphene is seen in figure 3.3(b) with bivacancy and trivacancy defects. Interestingly it is also possible to replace these vacancies with single atoms such as Pt, Co, In as shown in figure 3.3(c) [114].

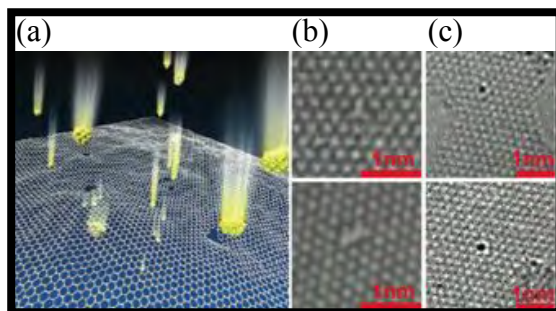


Figure 3.3: Creating defects by Argon ion bombardment. (a) Schematic of graphene bombarded with high energy particle. (b) HRTEM images of vacancy type defect created in graphene. (c) TEM images of Pt atoms trapped in the vacancies. (adapted from [114])

Although defects in graphene have been induced by different methods as mentioned above, most of the techniques require ultra-high vacuum conditions and costly machines to create plasma or electron or ion beams. In this work, we provide a new wet chemical method of inducing defects which is scalable at large industrial scale without using precision instruments like in semi-conductor industries. This study is important from the research point of view because graphene comes in contact with lot of chemicals during transfer process of CVD graphene and subsequent lithography processes. Although graphene is considered to be chemically inert, some chemicals can react with to graphene lattice structure and alter its properties. Many times these defects are be mistakenly considered to be intrinsic. Hence it is important to study the kind of defects created chemically and the evolution of defects. Understanding the reaction could lead to control of the type of defects induced and engineering them according to applications. Also the

study can be used to determine appropriate process preventing defects in graphene due to chemicals as we show it subsequent sub-sections.

Classifying the kind of defects created using different techniques is important for engineering application. Raman spectroscopy provides a fast and reliable method to study them. Defects in carbon-based materials has been studied since last 40 years in nano crystalline graphite [116–124], disordered carbon [125–127], carbon nanotubes [128–130] and graphene. Recently Raman spectroscopy has been used to classify different defects in graphene [131,132]. In this chapter we show, using Raman spectroscopy, how defects are induced by chemical method and type of defects induced in graphene with time.

### 3.1 CHEMICAL CONTROL OF DEFECTS DENSITY ON GRAPHENE

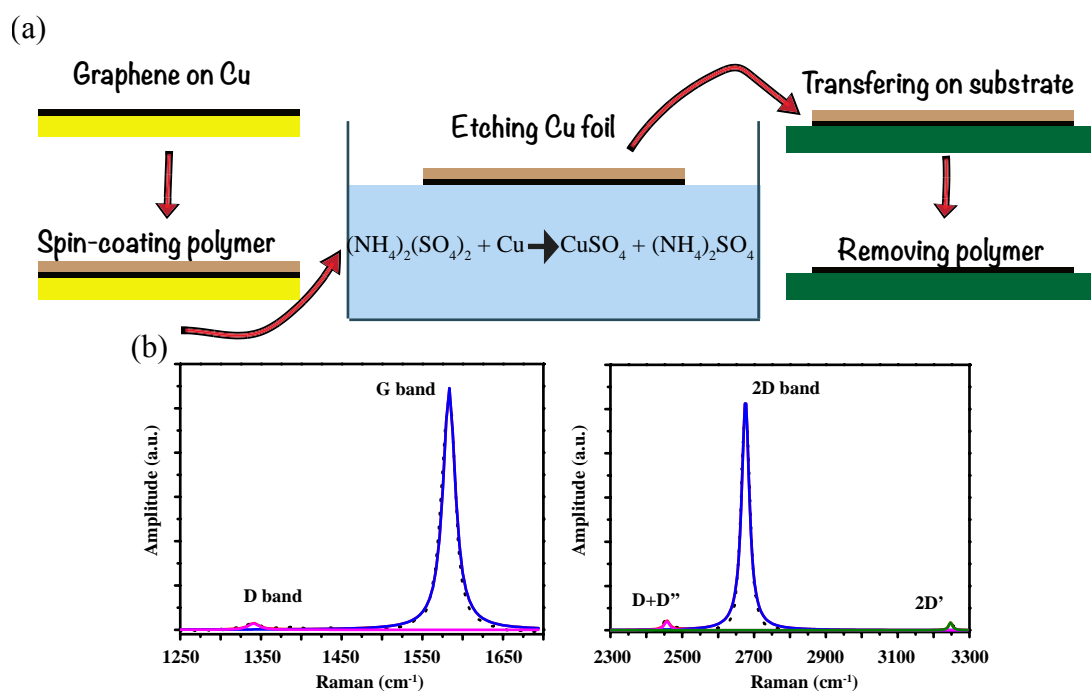


Figure 3.4: A typical liquid-assisted transfer process (a) PMMA is spin-coated on Graphene/Cu foil which is then etched in  $(\text{NH}_4)_2(\text{SO}_4)_2$  to remove copper. Then it is transferred on  $\text{SiO}_2$  wafer and PMMA is removed using acetone. (b) Raman spectra of graphene before inducing defects by chemicals.

Figure 3.4 shows the schematic of the protocol to transfer high quality graphene on a substrate (a) and then create defects in it using chemical method (c). Graphene is grown

using the CVD method on copper foil. It is spin-coated with a polymer which acts as a support layer when the copper foil is etched in Ammonium Persulfate  $(\text{NH}_4)_2(\text{SO}_4)_2$  solution. The concentration of the  $(\text{NH}_4)_2(\text{SO}_4)_2$  is kept at 0.1g/mL. After the copper is etched, graphene is washed in DI water to remove any ions adsorbed to its surface. It is then transferred to 300nm Si/SiO<sub>2</sub> substrate and the polymer is removed using acetone for few hours. Figure 3.4(b) shows the Raman spectra at 1800 grooves/mm grating of the graphene after the transfer. Typical Raman signature of graphene with G band at  $1582\text{ cm}^{-1}$  with FWHM =  $15\text{ cm}^{-1}$  and 2D band at  $2682\text{ cm}^{-1}$  with FWHM =  $26\text{ cm}^{-1}$  is observed. The presence of negligible intensity of D band compared to G band shows high quality of our CVD graphene which allowed us to observe other low intensity higher order bands such as D+D' and 2D'. Thus we are able to transfer graphene without inducing large amounts of defects.

One of the common chemical etchant that is used to dissolve copper foil is sodium persulfate  $\text{Na}_2(\text{SO}_4)_2$ . We found that this chemical is also able to induce defects in graphene. In order to study these defects, the samples of high quality graphene was transferred on Si/SiO<sub>2</sub> substrates and put under solution of 0.2 g/mL of  $\text{Na}_2(\text{SO}_4)_2$  solution at 35°C for a given amount of time as shown in figure 3.5(a).

Empirically we observed that the presence of copper ions is necessary to etch graphene, absence of which no etching took place. Therefore we dissolved a 1 cm X 1 cm X 25  $\mu\text{m}$  copper foil in 5 ml of solution of  $\text{Na}_2(\text{SO}_4)_2$ . After the etching graphene in these conditions, the sample was taken out of the solution, rinsed in DI water and in isopropanol before blow drying in nitrogen gas. The defects created in this process was monitored using Raman spectroscopy.

### 3.2 ASSESSING DEFECT DENSITY BY RAMAN SPECTROSCOPY

After the seminal work of Tunistra *et al* and efforts of the Raman community to understand the effects of number of defects on the vibrational properties of  $\text{sp}^2$  carbon systems, the emerging of monolayer graphene gives us the opportunity to emphasize this fundamental question. Raman spectra of the graphene after etching using  $\text{Na}_2(\text{SO}_4)_2$  is shown in figure 3.5(b). It is found that the D and D' peaks are increasing with time. The variation of the D peak amplitude and area with etching time is shown in figure 3.5(c). We notice that initially the intensity and area of D band increases with etching time and reaches its peak value. Similar behavior was observed where defects were created using oxygen/ halogen plasma or Ar bombardment. However, in our case, the amplitude and area of D band remains almost constant in the later stages of etching. Figure 3.5(d) shows that the FWHM increases significantly at later stage of etching but the position does not show variation.

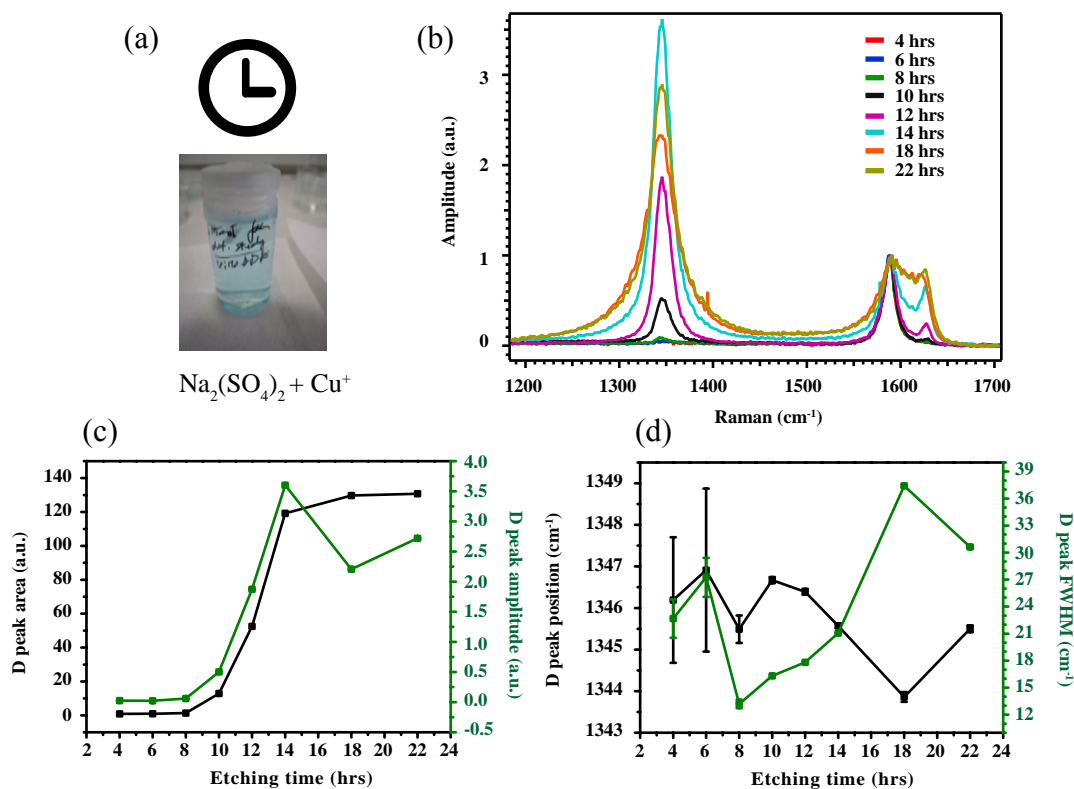


Figure 3.5: Raman evolution of chemical induced defects. (a) The graphene+ $\text{SiO}_2$  layer is dipped onto  $\text{Na}_2(\text{SO}_4)_2$  solution for given time. (b) Evolution of Raman spectra of graphene after putting under 0.2 g/mL  $\text{Na}_2(\text{SO}_4)_2$ . (c) and (d) Evolution of area, amplitude, frequency and FWHM of D peak with time of etching

The effect of etching graphene can be seen in the G and D' peaks as well. Figure 3.6 shows the evolution of the G and D' peaks with etching time. Here we have deconvoluted the spectra from  $1500 \text{ cm}^{-1}$  to  $1700 \text{ cm}^{-1}$  from figure 3.5(b) into two lorentzian peaks similar to [132]. For the first 6 hrs of etching the D' band is negligible. After 8~10 hrs, D' band makes its appearance. Thereafter its intensity increases rapidly until it stabilizes. On the other hand, G peak remains unaffected till 14 hours, after which its amplitude starts to decrease. Clearly from these figures, there are different stages of etching process. This kind of behavior is also seen in graphene where defects were induced by oxygen/fluorine plasma and Ar ion bombardment as mentioned in literature above. In order to understand this behavior, we follow a well known model as explained below.

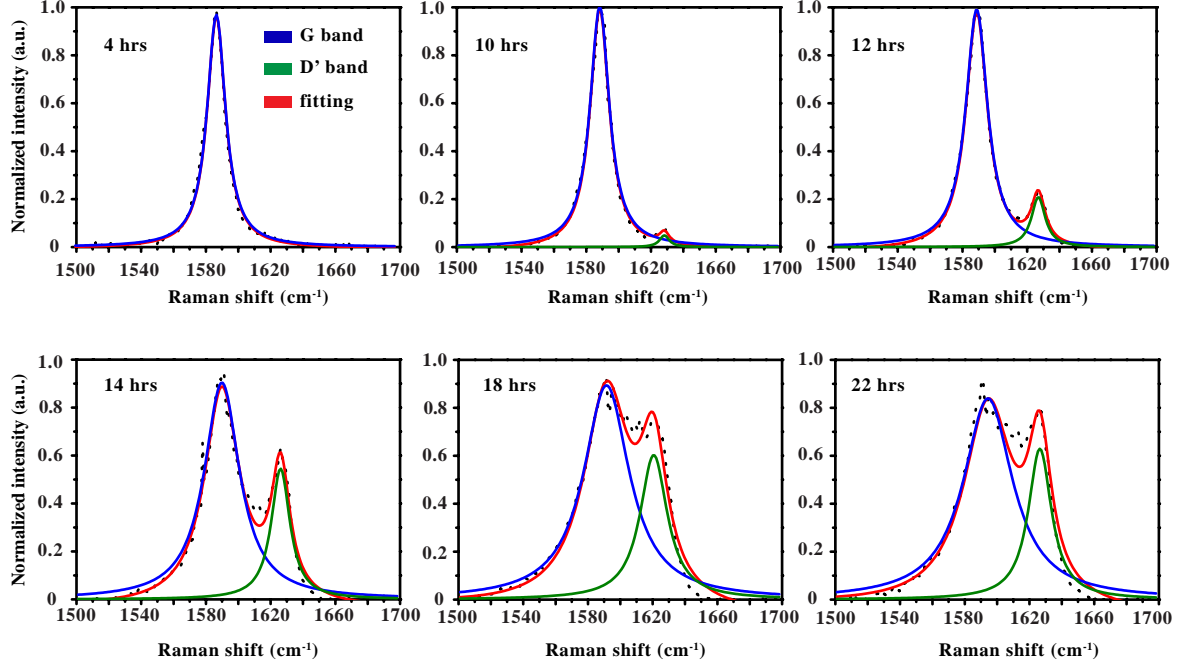


Figure 3.6: Evolution of the G peak and D' peak with etching time.

Lucchese *et al* in [112] observed similar behavior in Raman study of defects induced by Ar ion bombardment in graphene. In figure 3.7(a), the defect is assumed to be at the center of circle with  $r_s$  showing the structurally disordered graphene due to defect. The region between  $r_s$  and  $r_a$  is called activated region where selection rules break down and intensity of D band is enhanced. This means that any electron-hole pair created in activated region is able to travel long enough to be scattered by the defect and detected by spectroscopy method. Therefore the intensity of D band can be correlated to green region. So as the number of defect density increases figure 3.7(b, c), the green region starts to cover more area until figure 3.7(d). At this point the D band reaches its maximum intensity, thus completing the stage 1. Thereafter as the defects increase in stage 2, the red region start to cover more area which means breaking of the hexagonal graphene lattice structure itself leading to decrease in all Raman bands as shown later.

If we consider intensity of G band is represented by the white+green region, then the ratio between  $I_X/I_G$ , where X is D or D', will increase with etching time till it reaches maximum value. The increase in D band and D' band is due to increase in defect density of graphene. In order to quantify the defect density, we define  $L_d$  as the distance between two defects. The  $I_X/I_G$  ratio is related to  $L_d$  by equation.



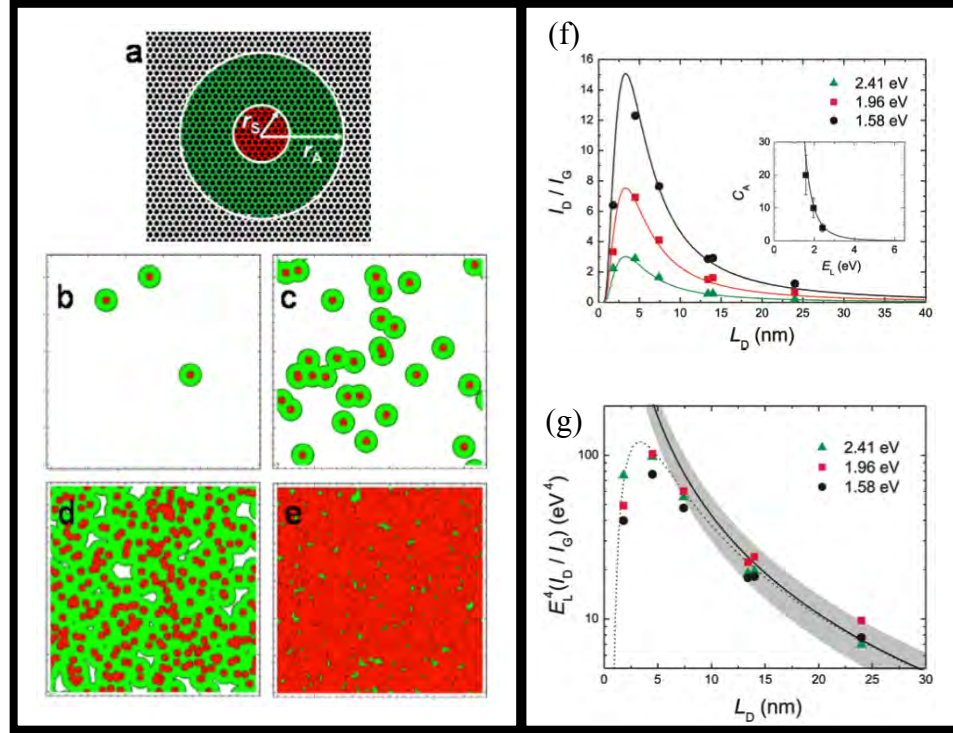


Figure 3.7: Modeling of defect influence on optical phonons. (a) gives definition of the "activated" A-region (green) and "structurally-disordered" S-region (red). The radii are measured from the center of defects in the simulation [112]. (b-e) shows the evolution of the "activated" and "structurally-disordered" with time. (f)  $I_D/I_G$  for graphene with three different laser energies. Inset plots  $C_A$  as function of  $E_L$ . (g)  $E_L^4(I_D/I_G)$  as function of  $L_D$  which converges the three curves in (f) into one curve by taking into account  $C_A = 160E_L^{-4}$ . These figures are taken from [111].

$$I_X/I_G = C_A f_A(L_d) + C_S f_S(L_d) \quad (6)$$

where X stands for D or D' band.  $f_A$  and  $f_S$  represent the fraction of area of "Activated" (green) and "Structurally-disordered" (red) regions in figure 3.7(b), (c), (d), (e). They are function of  $L_d$ .  $C_A$  is the ratio of scattering efficiency between the phonon X and G phonon in activated region and  $C_S$  relates to  $I_X/I_G$  due to distortion of crystal lattice. Equation 6 can be further written as

$$I_X/I_G = C_A \frac{(r_a^2 - r_s^2)}{(r_a^2 - 2r_s^2)} [e^{-\pi r_s^2/L_d^2} - e^{-\pi(r_a^2 - r_s^2)/L_d^2}] + C_S [1 - e^{-\pi r_s^2/L_d^2}] \quad (7)$$

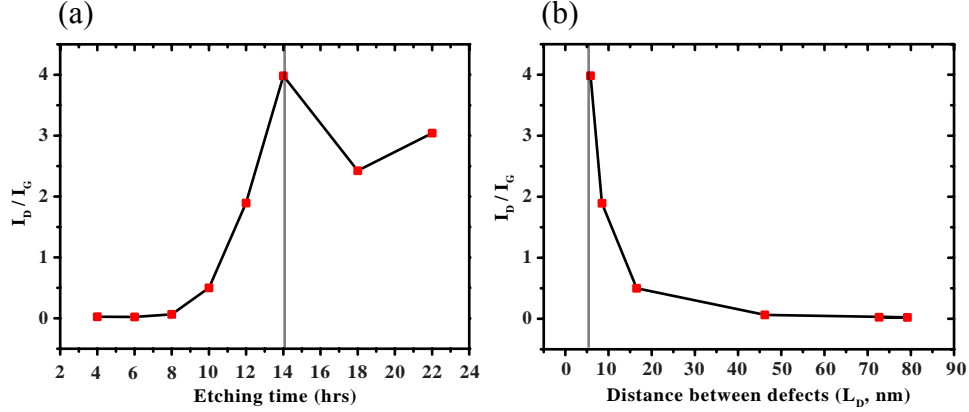


Figure 3.8: Kinetics of defect formation by chemical etching. (a) gives the  $I_D/I_G$  ratio with the etching time in our sample. (b) shows the  $I_D/I_G$  ratio with distance between  $L_d$ , distance between defects. The straight line gives the value of  $L_D$  of 5 nm at the end of 14 hours of etching.

In the limit of low defect concentration equation (7) becomes

$$I_D/I_G = C_A \frac{\pi(r_a^2 - r_s^2)}{L_d^2} + C_S \frac{\pi r_s^2}{L_d^2} \quad (8)$$

According to [132],  $C_S$  has very little effect (less than 10%) on stage 1 since it concerns contribution from breaking of C-C bonds and can be neglected for D band for low defect contribution. Hence equation (8) can be assumed as

$$I_D/I_G \approx C_A \frac{\pi(r_a^2 - r_s^2)}{L_d^2} \quad (9)$$

From equation 9,  $C_A$  is the maximum value of  $I_D/I_G$  when the D band is activated in entire sample. From ref [111, 131], we find that the above ratio depends on the laser wavelength as shown in figure 3.7(f). This is because  $I(D)$  and  $I(D')$  shows no dependence while  $I(G)$  is proportional to forth power of laser energy. Therefore the laser dependence can be normalized using following equation as shown in figure 3.7(g) as it is done in [111].

$$C_A = 160E_L^{-4} \quad (10)$$

where  $E_L$  is 2.33 eV for 532 nm laser used. Using value of  $C_A$  from equation(10),  $r_a = 3$  nm,  $r_s = 1$  nm and using equation(9), we find the distance between defects,  $L_d$ , corresponding to the values of  $I_D/I_G$ .  $r_a = v_F/\omega_D$ , where  $v_F$  is Fermi-velocity and  $\omega_D$  is frequency of D phonon. Value of  $r_s$  depends on the type of defect.

The distance between defects at different stages are represented in figure 3.9(a).  $L_d$  is the distance between the centers of the defects. At stage 1, defects are far away from each other but at the end of stage 1, the defect density increases such that the green circles touch each other. At this point, the defect density is  $8.8 \times 10^{11}$  per  $\text{nm}^2$  according to equation 11. The value of  $I_D/I_G$  is maximum and an ideal value of  $L_d$  should be around 6 nm. In the literature, the value of  $L_d$  is as found to be around 3-4 nm [110–112]. At the stage 2, there is overlap of the green region due to high density of defects which can be calculated from following equation.

$$n_D = \frac{10^{14}}{\pi L_D^2} \quad (11)$$

where  $n_D$  is density of defects and  $L_D$  is distance between defects.

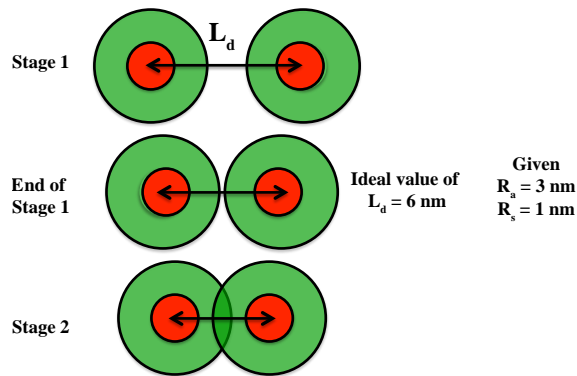


Figure 3.9: Model of distance between defects at different stages of etching. At the end of stage 1, the green circles (defect activated region) touch each other at which the distance between defects is around 6 nm. At stage 2, the defects come closer thus overlapping the activated regions.

In figure 3.8(a) we have presented the ratio of intensity of D and G peaks from our spectra of figure 3.5(b). We find that it reaches a maximum value at 14 hrs of etching time after which it starts to fall. The maximum value of ratio can be considered as the time which separates the etching process in stage 1 and stage 2. The distance between defects,  $L_d$ , is calculated corresponding to the values of  $I_D/I_G$  and are plotted in figure 3.8(b). In our case, the distance between defects at the stage 1 is found to be around 5 nm which is higher than that in literature.

The evolution of defect formation can be divided into two stages at 14 hrs at which the  $I_D/I_G$  is maximum. At stage 1, the graphene lattice structure is still intact but in stage

2, the distance between defects is less than 6 nm and the lattice structure starts to break leading to amorphization of hexagonal lattice structure of graphene. Figure 3.10 shows the evolution of area, intensity, FWHM, position of G peak and D' peak with etching time.

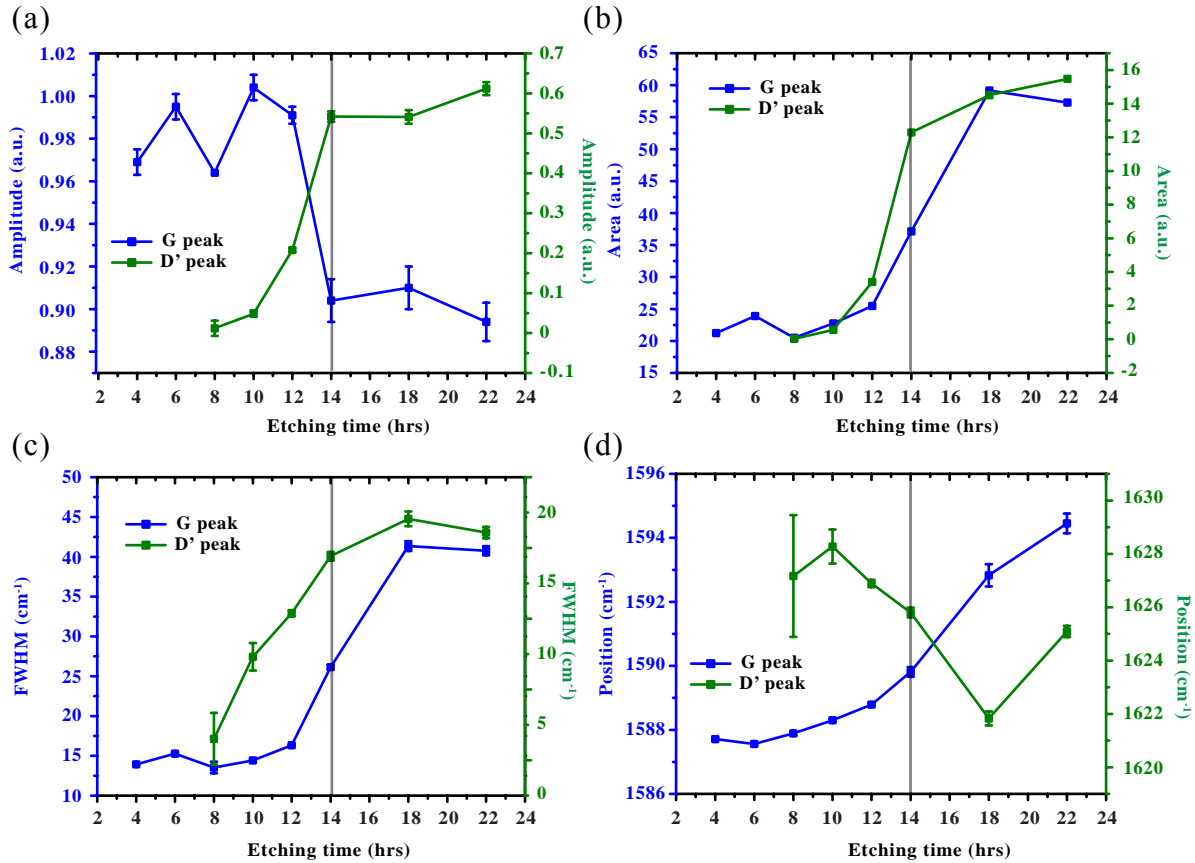


Figure 3.10: Raman analysis of G and D' phonons. Evolution of amplitude, area, FWHM and position in (a), (b), (c) and (d) respectively of the G peak and D' peak with etching time.

Figure 3.10(a) shows the amplitude of the G peak and D' peak. Initially the intensity of G peak remains constant at stage 1 but immediately starts to fall as stage 2 is reached. On the other hand, D' intensity continues to rise with time even after stage 2. According to theory, D' intensity is expected to go down but it continues to rise in our case unlike in ref [131, 132] where it almost remained constant. In figure 3.10(b), both the area of G and D' peak increase with time. Though the intensity of G peak decreases, its area increases

due to increase in its FWHM as shown in figure 3.10(c). Stage 2 has higher FWHM since the graphene  $sp^2$  structure starts to break and presence of  $sp^3$  bonds increases. The decrease in life-time of phonon is attributed to the fact that the distance travelled by electron-hole pairs before scattering with defect is less than distance travelled before scattering with a phonon.

In stage 1, the frequency of G peak does not change much but as approach stage 2, its frequency starts to increase as theoretically calculated in [110]. In stage 1, the C-C bond are still  $sp^2$  hybridized but in stage 2 they are  $sp^3$  hybridized which applies strain in the lattice. The increase could also be due to presence of double bonds instead of delocalized bonds in graphene structure [133]. Since the graphene lattice structure is no more  $sp^2$  hybridized, the frequency of D' band decreases in stage 2 leading to difficulty in separating the peaks. Similar results have been calculated and observed in ref [91, 110, 132]. It is also to be noted that, in our case, the position of D' peak unexpectedly increases at 22 hours of etching.

All the Raman defect studies have focussed on the evolution of Raman spectra on local area. In figure 3.11, we present for the first time (as far as we know) the spatial evolution of defects with etching time. Three different samples were put under solution of  $Na_2(SO_4)_2$  for 2 hrs, 10 hrs, 22 hrs. In each sample we make a confocal Raman mapping using 50X objective with 532nm laser. 1800 grooves/mm grating is used which gives a resolution smaller than  $0.9\text{ cm}^{-1}$ . After 2 hrs of etching under solvent, figure 3.11(a) shows that the D band intensity in almost negligible is graphene except in wrinkles. It can be explained from the simulation in [134] that formation in wrinkles leads to breaking of C-C bonds which in turn leads to higher intensity of D band. After 6-10 hrs, the intensity of D band has increased overall and the wrinkles show higher intensity. The chemical kinetics could be higher at the wrinkles due to broken or strained C-C bonds which increase its reactivity with etchant.

After 22 hrs, intensity is almost uniform due to the limitation of spot size (300 nm) of laser except at the edge of graphene. At the edge of graphene, intensity of D band decreases since the laser spot collects information outside the sample and makes an average. As the intensity of D peak increases, intensity of the G and 2D peaks decrease due to increase in C-C  $sp^3$  bonds with etching time as shown in figure 3.11(b) and (c), respectively.

The study shows that chemicals are able to induce defects in graphene. In our case, we discover that  $Na_2(SO_4)_2$  induces defects in graphene after around 2-3 hours in contact which is important to know when fabricate device (see chapter 2). However what is the type of defect induced during this process?

Raman spectroscopy has also been used to characterize the type of defect produced in graphene [131]. In stage 1,  $I(D) \sim A_d N_d$  and  $I(D') \sim B_d N_d$  where  $N_d$  is the defect concentration while  $A_d, B_d$  depends only on perturbation caused by the defect. Hence

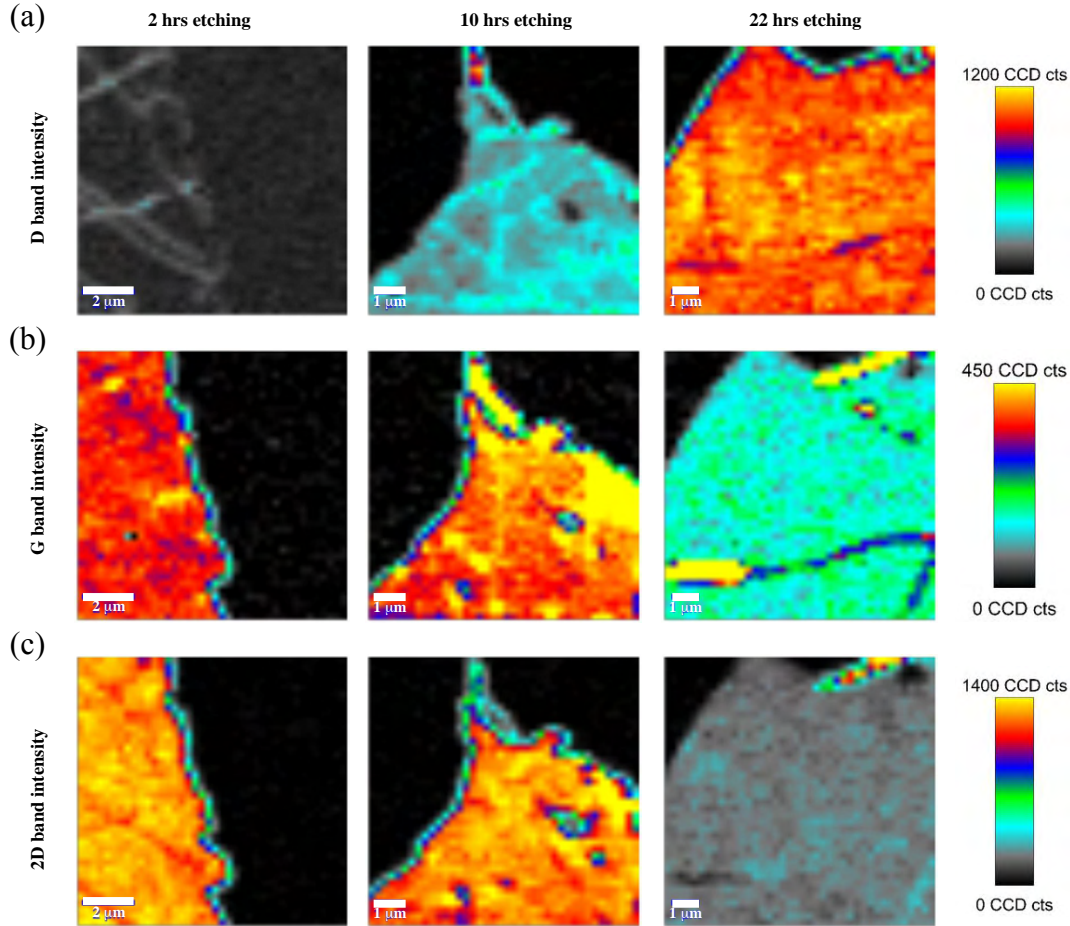


Figure 3.11: Spatially resolved Raman imaging of defect formation. Raman mapping of CVD graphene. (a), (b), (c) shows the D peak, G peak and 2D peak respectively with etching time.

$\frac{I_D}{I_{D'}} \sim \frac{A_d}{B_d}$  depends on the type of defect. This is shown in figure 3.12(a) where  $\frac{I_D}{I_{D'}} = 13$  for  $sp^3$  defects, = 7 for vacancies and 3.5 for boundaries according to ref [131]. Within the figure, we have plotted our data as shown in red squares with an orange line showing the slope. We have found the ratio  $\frac{I_D}{I_{D'}}$  to be around 9. This means that we have mixture of  $sp^3$  and vacancies defects.

In ref [132], the above difference in ratio is attributed to  $C_{S,D'}$  which is the  $C_S$  for  $D'$  peak. We recall  $C_S$  gives the cross-section of  $\frac{I_D}{I_G}$  due to lattice distortion. Although there is no clear explanation in literature,  $C_S$  is found to be more important for  $D'$  peak

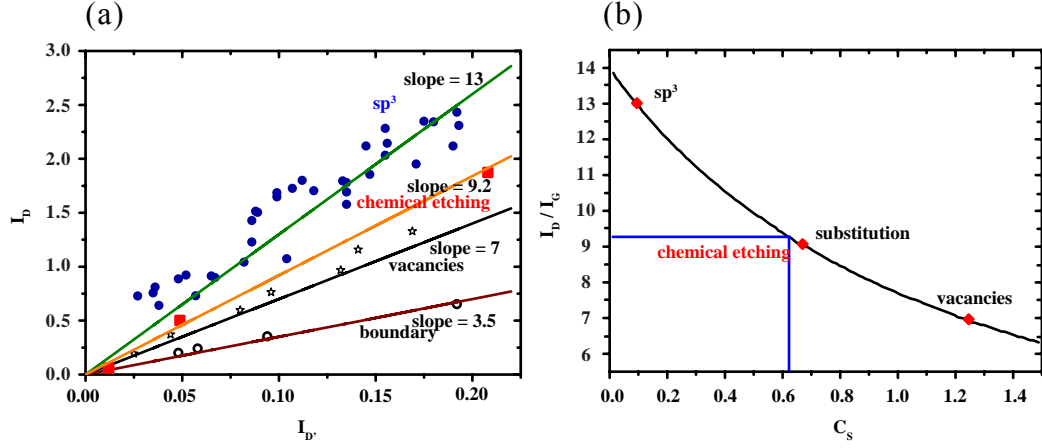


Figure 3.12: Discrimination of defect nature from Raman analysis. (a) Linear dependence between  $\frac{I_D}{I_{D'}}$  for different types of defects. Figure adapted from ref [131] and our data added in red (chemical etching). (b) Plot of  $\frac{I_D}{I_{D'}}$  as function of  $C_S$  adapted from ref [132] with blue lines showing value of  $C_S$  for chemical etching process.

than for D peak and its value depends on the type of defect. A possible way to explain would be: we had assumed that the defect induced phonon arise from center of defect as shown figure 3.7(a) and travels through a distance  $r_a$ . D' phonon has a shorter value of  $r_a$  compared to D phonon as they have higher frequency ( $r_a = v_F/\omega_{D'}$ , where  $v_F$  and  $\omega_{D'}$  is frequency of D' phonon). Since the  $r_s$  do not change, D' phonon are more likely to be affected by lattice distortion than D phonon. Hence

$$I_{D'}/I_G \approx C_{A,D'} \frac{\pi(r_{a,D'}^2 - r_{s,D'}^2)}{L_d^2} + C_{S,D'} \frac{\pi(r_{s,D'}^2)}{L_d^2} \quad (12)$$

where  $C_{A,D'}$ ,  $r_{a,D'}$ ,  $r_{s,D'}$  are  $C_A$ ,  $r_a$ ,  $r_s$  for D' peak. And similarly for D peak equation(9) can be written as

$$I_D/I_G \approx C_{A,D} \frac{\pi(r_{a,D}^2 - r_{s,D}^2)}{L_d^2} \quad (13)$$

Hence

$$I_D/I_{D'} \approx \frac{C_{A,D}(r_{a,D}^2 - r_{s,D}^2)}{C_{A,D'}(r_{a,D'}^2 - r_{s,D'}^2) + C_{S,D'}r_{s,D'}^2} \quad (14)$$

Ref [132] plots the eq.(14) taking  $C_{A,D} = 4.2$ ,  $C_{A,D'} = 0.5$ ,  $r_{a,D} = 3$  nm,  $r_{s,D} = 1$  nm,  $r_{a,D'} = 2.6$  nm,  $r_{s,D'} = 1.4$  nm. These data and plot of eq.(14) are adapted from ref [132]. The value of  $C_{A,D'}$  is calculated from coupling between D' phonon and G phonon. STM images of defects gave values of  $r_s$ . Although these value were calculated for Ar+ ion bombardment samples, we note that eq.(14) has been used to find  $C_S$  for all kinds of defects and is independent of laser energy as the energy term in  $C_A$  and  $C_S$  in numerator and denominator cancels out.

Also intensity of both D peak and D' peak do not depend on laser energy [135]. If  $C_{S,D'}$  would be = 0, then  $I_D/I_{D'}$  would have been constant regardless of the type of defect. The plot of eq.(14) is shown in Figure 3.12(b) (adapted from ref [132]). Our date point ( $I_D/I_{D'} = 9.2$  and  $C_S = 0.62$ ) is quite close to that found for substitution defects where carbon atoms are substituted by boron atoms leading to higher  $sp^3/sp^2$  ratio. In our case, we could be grafting some molecules such as hydrogen onto carbon atoms forming  $sp^3$  bonds which activated defect-assisted peaks.

As far as TEM images cannot differentiate between  $sp^3$  and  $sp^2$  bonds, TEM images of graphene under etchant for 0 hr and 15 hr show no difference in atomic structure (see figure 3.13). The first image (a) is from graphene which is not etched while the second image (b) is after 15 hours of etching in  $Na_2(SO_4)_2$ . Both these figures show large area of graphene with hexagonal carbon structure and large patches of PMMA which could not be removed even after putting under warm acetone for few hours. From the available TEM images till now, it seems there is negligible amount of atomic defects or vacancies. However, the Raman defect bands are activated in these samples with etching time in similar manner as shown in figure 3.5(c).

Although no quantitative analysis is made, the longer etched sample (more than 20 hrs) seemed to more easily destroyed under irradiation. TEM images shown in figure 3.13(c) show that holes in the graphene seemed to grow bigger under the e-beam irradiation.

The fact that the TEM images in figure 3.13 show no difference in lattice structure and Raman intensities and areas of D and D' band in figure 3.10(a) and figure 3.10(d) respectively, do not fall after 20 hours of etching, we could point towards a possible mechanism of defects induced in graphene which is different from plasma-induced defects.

1. Initially there could be grafting of hydrogen molecules which contribute to increase in defect induced bands by forming  $sp^3$  bonds. Hydrogen is the only element that is smaller than carbon atom that could be present during the process. Any other bigger element would have been detectable by TEM imaging. This process of grafting hydrogen reaches a maximum value at 14 hours of etching.
2. Thereafter as we keep the sample in etchant, the reaction grafting hydrogen molecules is unable to form further  $sp^3$  bonds since surface of graphene reaches a certain saturation limit. Therefore we reach a quasi-stage 2 where the intensity of D and D'



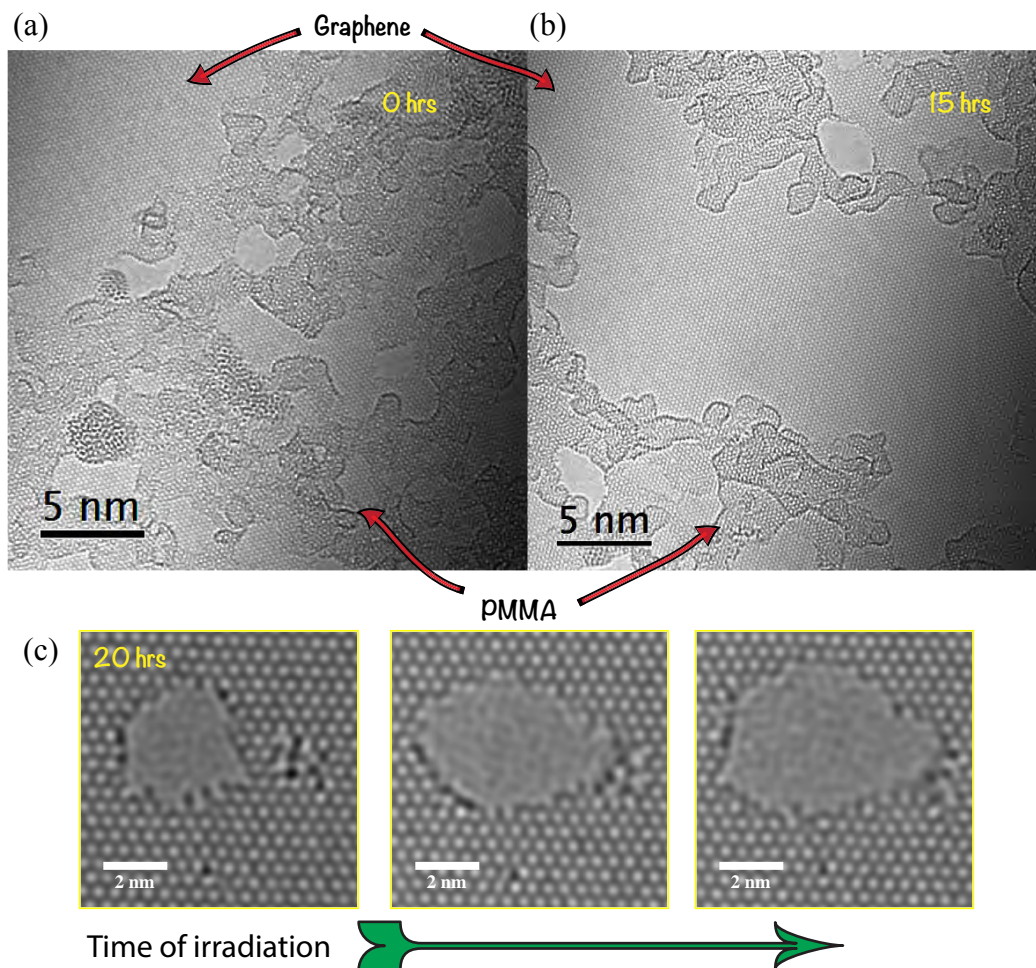


Figure 3.13: Atomic structure of graphene in different stages. TEM image of graphene after (a) 0 hr (b) 15 hr of etching. (c) hole in graphene upon irradiation. Image courtesy Hanako OKUNO from CEA Grenoble on our CVD graphene.

band do not decrease. Beyond this point, energy is required to form C-H bonds. This is possible in the case of hydrogenation using plasma [93,94].

Indeed effect of annealing could be seen with Raman bands in a similar manner as was observed in hydrogenated graphene samples in [91,93,94]. The chemically defected samples (12 hours) were annealed in ultra high vacuum (UHV) at 500°C for one hour. As it can be observed in figure 3.14(a), the intensity of D and D' bands decrease which confirms the reversible defect creation using chemicals. The frequency of G band slightly

increases while intensity of 2D band decreases (See figure 3.14(b)). Such effects on G and 2D band are due to doping effect from the substrate and are also observed due to annealing effect on hydrogenated sample using plasma. Since we not able to observe any other atoms in the graphene lattice structure using TEM analysis and defect formation in graphene is reversible, we can probably suggest that we are grafting hydrogen in graphene lattice as shown in the schematic in figure 3.14(c). Formation of graphene oxide is ruled out because G peak in graphene oxide is a single lorentzian with frequency around  $1600\text{ cm}^{-1}$  with a broad D peak and negligible 2D peak [133].

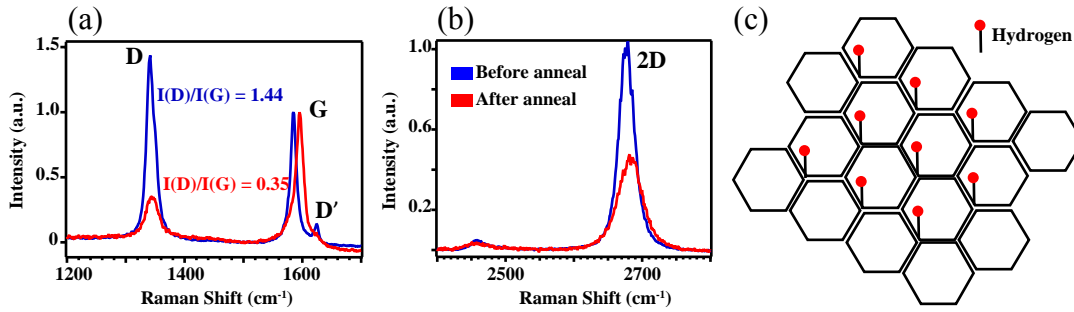


Figure 3.14: Effect of annealing on Raman bands in ultra high vacuum (UHV) at  $500^{\circ}\text{C}$  for one hour. Effect of annealing on (a) D, G and D' bands. (b) 2D band. (c) Schematic of hydrogenated graphene.

### 3.2.1 Effect of high density of defects on optical phonons

Although the Raman spectra of fluorinated graphene in ref [132] are fitted with 2 peaks (G peak and D' peak), a closer look at them in figure 3.15(b) shows that fitting is not very accurate. Therefore one of the spectrum was extracted and replotted with 4 lorentzian peaks as shown in figure 3.15(c). It can be observed that the spectra is better fitted in this case and similarly our spectra can also be fitted with 4 lorentzian peak as shown in Figure 3.15(d).

Figure 3.16(a) and (b) shows the dispersion of G peak and D' peak when the spectra is fitted with only two peaks like it is done in the literature. Contrary to general positive dispersion of G peak in ref [111, 125, 136], in our case, G peak has a dispersion of about  $\frac{\partial\omega_G}{\partial\epsilon_L} \approx -6\text{ cm}^{-1}$ . A possible reason could be difference of etching methods. On the other hand, D' peak shows a dispersion similar to ref [132] with positive dispersion of  $\approx 7.8\text{ cm}^{-1}$ .

Figure 3.17(a),(b),(c) and (d) are dispersion curves when the spectra is plotted with four curves like in Figure 3.15(d). Here we find that the peak 1 and peak 2 behave like G

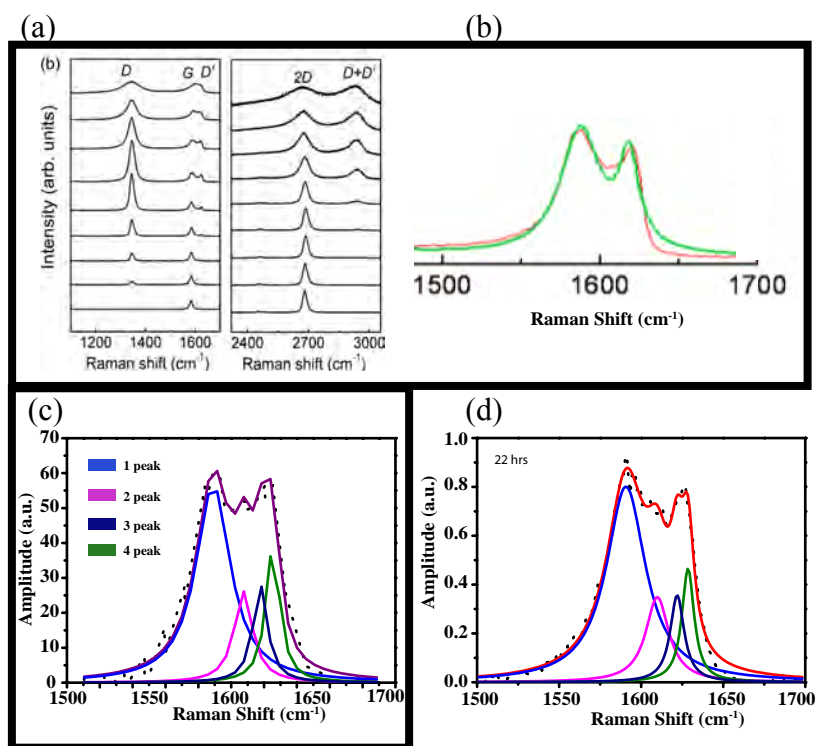


Figure 3.15: Splitting of G and D' phonons for high density defect sample. (a) Raman spectra of fluorinated graphene with increasing defect concentration. (b) Example of spectra with fitted with two Lorentzian peaks. (Green) overall fitting on (red) spectrum. (a) and (b) adapted from [132]. (c) and (d) Comparison of highly defective graphene between fluorinated and chemical etching respectively.

peak with negative dispersions of  $4.9 \text{ cm}^{-1}$  and  $5.7 \text{ cm}^{-1}$  respectively. Peak 3 and peak 4 follows the same trend as that of D' band with positive dispersion curve of  $5 \text{ cm}^{-1}$  and  $6.6 \text{ cm}^{-1}$  respectively. Peak 1 and 2 could be a split of G peak. Due to deformation of lattice structure due to high density of defects, the  $E_{2g}$  vibrations frequency may not be same in two different directions and hence the split. Peak 3 and 4 could be explained by the fact that intra-valley resonance process of D' peak could follow two paths i.e. defect scattering  $\rightarrow$  phonon scattering or phonon scattering  $\rightarrow$  defect scattering (refer to annex for scattering process of D' band). The two different paths could lead to small difference in frequency. Another possible explanation of splitting of bands could be due to huge change of phonon dispersion relation due to high density of defects.

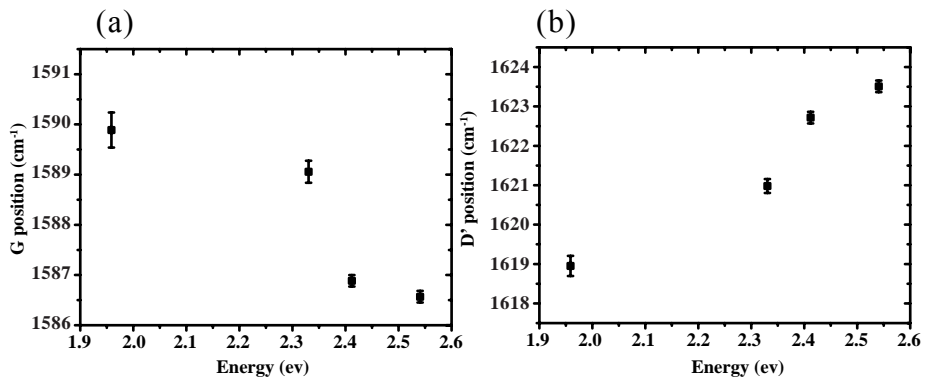


Figure 3.16: Dispersion of G and D' peak for density defect sample. (a) G peak and (b) D' peak as a function of laser energy.

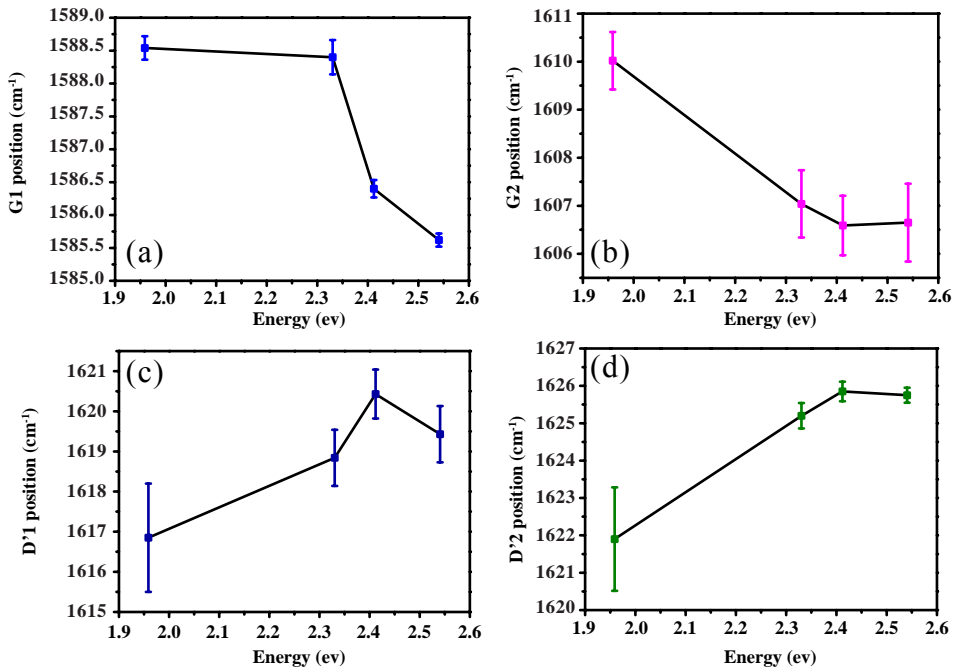


Figure 3.17: Splitting of G and D' band at high defect concentration. (a) G1 peak, (b) G2 peak, (c) D'1 peak and (d) D'2 peak as a function of laser energy

### 3.2.2 Defect study using second-order Raman scattering

Though the first-order Raman graphene bands such as D peak, G peak and D' peak have been extensively used to study defects in graphene as mentioned in sub-section above,

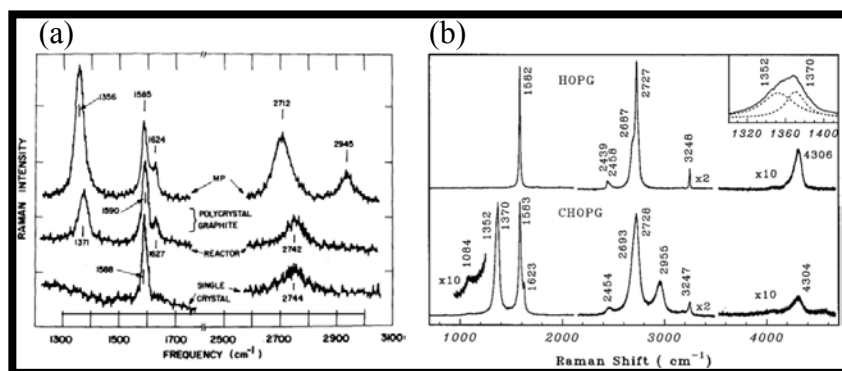


Figure 3.18: Defect comparison with graphite. (a) Raman spectra of single crystal and polycrystalline graphite. (adapted from [118]). (b) Raman spectra of Highly Oriented Pyrolytic Graphite (HOPG) and carbon implanted HOPG. (adapted from [137])

there are few studies on second-order Raman peaks. But these peaks have been observed in different systems since 1970s [117–119, 122]. In ref [138], Raman scattering upto 5th order has been observed due to peculiar enhancement of higher order Raman peaks. However in this section we will only talk about certain second-order bands such as the 2D peak, D+D'' peak, 2D' peak, D+ D' peak and how these peaks behave with introduction of defects in graphene. As it can be observed in figure 3.18(a), Tsu *et al* had shown the presence of D+D' peak in graphite crystals as early as 1978. This band is absent for single crystal graphite but is present in polycrystalline graphite [118]. More recently in 1998, Tan *et al* had observed the D+ D' peak at  $\approx 2980 \text{ cm}^{-1}$  when Highly Oriented Pyrolytic Graphite (HOPG) was bombarded with carbon ions as shown in figure 3.18(b).

The D+D'' peak was also known as G\* peak initially. The frequency of the peak is around  $2450 \text{ cm}^{-1}$ . It was observed in highly oriented pyrolytic graphite (HOPG) as far back as 1981 [119, 122]. Since then it has been reported in many carbon materials. The D+D'' originates from a two phonon process which involves transverse optical (TO) and longitudinal acoustic (LA) phonon [139, 140]. The TO branch contributes to D peak ( $1333 \text{ cm}^{-1}$ ) and LA branch contributes to D'' ( $1130 \text{ cm}^{-1}$ ) giving a total around  $2450 \text{ cm}^{-1}$ .

The 2D' peak which arises at  $\approx 3200 \text{ cm}^{-1}$  is the overtone of D' peak. It can be seen in HOPG and graphene without defects. Like the 2D peak, it is a double resonance but an intra-valley process involving two phonons of opposite vectors to conserve momentum from the LO branch of the phonon dispersion around  $\Gamma$  point [66, 141, 142]. There are many experiments which show that this peak is affected by strain like the D, G, 2D peaks [143, 144].

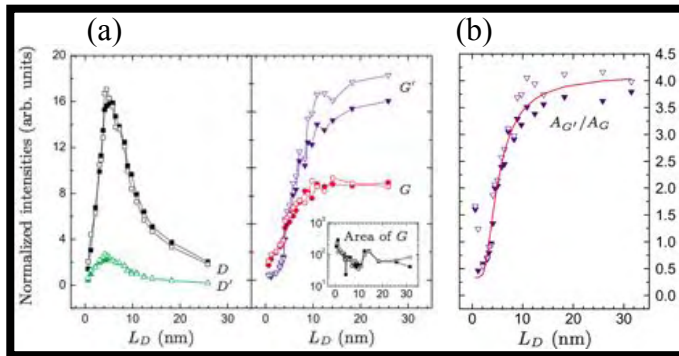


Figure 3.19: 2D optical phonon evolution with defects. (a) Normalized intensities of D, D', G and G' as a function of distance between defects ( $L_D$ ). Here G' is same as 2D. (b)  $A(G')/A(G)$  or  $A(2D)/A(G)$  as a function of ( $L_D$ ) (adapted from [110])

Unlike the above three bands, D+D' peak which exists at  $\approx 2980 \text{ cm}^{-1}$  is a defect induced peak. It was previously known as D'' peak. In ref [119], it is mentioned that the peak is affected by the varying crystallite size of HOPG, glassy carbon, pressed carbon rods, and carbon powders. Later this peak was studied in ion-implanted HOPG to induce defects [145,146]. It is a two phonon state with a combination of D peak ( $1360 \text{ cm}^{-1}$ ) and D' peak ( $1620 \text{ cm}^{-1}$ ), both of which are defect activated peaks.

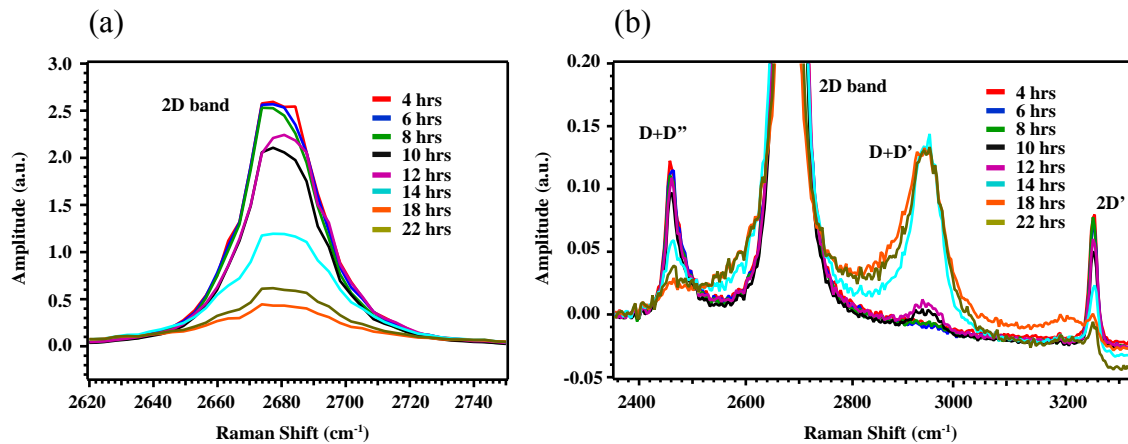


Figure 3.20: Effect of etchant on second order optical phonons. (a) and (b) overtones (2D and 2D') and two phonon (D+D'' , D+D') Raman spectra of CVD graphene after etching under  $\text{Na}_2(\text{SO}_4)_2$ .

In literature, we find that the 2D peak has been utilized to study defects in graphene. Ref [131] shows the evolution of the intensity and integrated area of the 2D peak as the defect concentration increases using mild plasma. In ref [105, 110] the ratio of  $I_{2D}/I_G$  is used to separate the two stages of defect formation. This can be seen in figure 3.19(a) where intensities of D, D', G and G' or 2D has been plotted vs.  $L_D$ . Figure 3.19(b) shows that the ratio of  $A(2D) / A(G)$  decreases exponentially as the density of the defect increases. However the other two second-order phonon peaks and overtones in similar studies have not been used to study defects in graphene. This is probably due to much lower intensity of these peaks compared to G, D, D' and 2D peaks. In this subsection we present the evolution of two phonon and overtone peaks with defects that have been induced by chemical means as mentioned in previous subsection. From figure 3.20(a), we can observe that the 2D peak decreases as the etching time increases. Figure 3.20(b) shows the zoomed image of three peaks. Here the 2D, D+D'' and 2D' peaks start to decrease with etching time since their resonance process do not involve scattering from defects. On the other hand, defect induced D+D' peaks start to increase its intensity since it involves scattering from defects as mentioned earlier.

Figure 3.21 (a), (b) and (d) shows the evolution of area, intensity and FWHM of these peaks with the etching time respectively. In each of these figures, there is a transition time at around 14 hours. In figure 3.21(a), at 14 hours there is maximum decrease of intensity of 2D, D+D'' and 2D' while D+D' has maximum increase at this point. This is same for area under the peak in figure 3.21(b). The FWHM of all the peaks increases in stage 2 in figure 3.21(d), as the  $sp^2$  structure of the graphene lattice starts to break which causes decrease in the phonon life-time. This behavior is very similar to what we had already observed in figure 3.10(a), (b) and (c). However there is not much change in position of D+D'', 2D, D+D' and 2D' peaks in figure 3.21(c). Unlike our results, position of 2D peak is found to decrease at stage 2 in ref [110]. This could be due to different mechanism of etching in our case.

Figure 3.22(a) show that the  $I(D + D')/I(G)$  behaves in the same manner as  $I(D)/I(G)$  and  $I(D')/I(G)$ . On the other hand,  $I(D + D'')/I(G)$  and  $I(2D')/I(G)$  decrease as the defects concentration increases in figure 3.22(b). In these figures the values of  $L_d$  is taken from equation(9) since the distance between defects remains same for all Raman peaks. The light brown curves in both these diagrams are guide to the eye. It seems that these peaks are highly sensitive to defect formation and could be used for finest determination of different stages of etching even possibly the difference between grafting hydrogen bonds and breaking  $sp^2$  bonds.

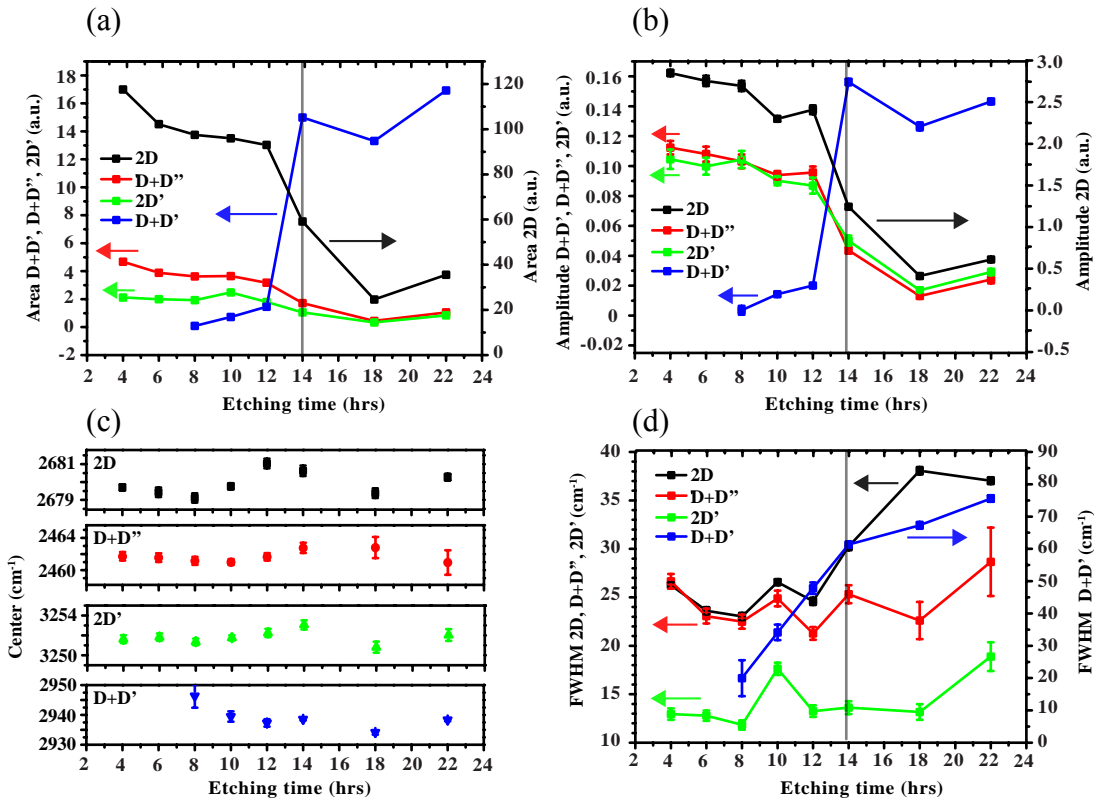


Figure 3.21: Raman analysis of second order phonons with etching time. Evolution of area, amplitude, position and FWHM in (a), (b), (c) and (d) respectively of overtones ( $2D$  and  $2D'$ ) and two phonon ( $D+D''$  and  $D+D'$ ). Raman spectra of CVD graphene after putting under  $\text{Na}_2(\text{SO}_4)_2$ .

### 3.3 INTRODUCTION TO CHARGED DEFECTS

In the above section, we have seen how we can induce structural defects in graphene. However there is another kind of defect that can be induced in graphene without affecting its structure. In liquid assisted transfer method, a substrate is used to fish the graphene from below and left to dry. With time, the liquid flows out and lets the graphene+PMMA stick to substrate surface. However some molecules/ions remain and some get trapped between graphene and substrate. These charges act as scattering points which limits the mobility of CVD graphene on  $\text{SiO}_2$  substrate to around  $5000\text{-}7000\text{ cm}^2\text{V}^{-1}\text{s}^{-1}$  [16] while suspended graphene has mobility as high as  $200,000\text{ cm}^2\text{V}^{-1}\text{s}^{-1}$  [57].



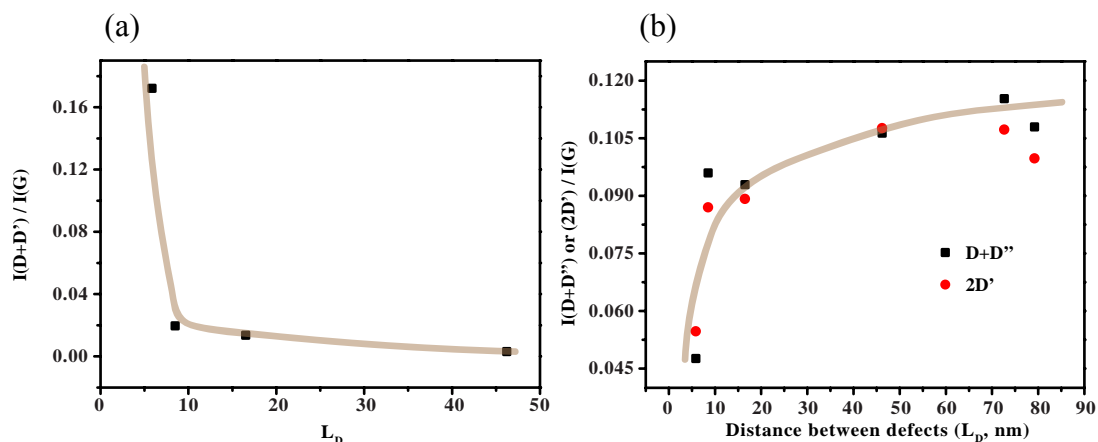


Figure 3.22: High sensitivity of second order phonons with defect density. (a)  $I(D + D')/I(G)$ , (b)  $I(D + D'')/I(G)$  and  $I(2D')/I(G)$  vs.  $L_d$ . The light brown lines are guide to the eye.

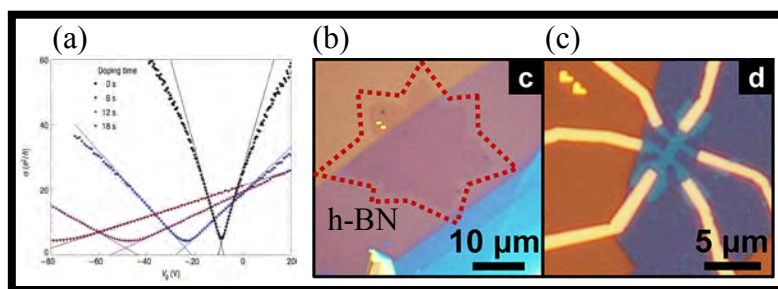


Figure 3.23: Effect of charged dopants on transport properties. (a) The conductivity  $\sigma$  versus back-gate voltage ( $V_g$ ) for pristine graphene and with increasing doping concentrations with time. (adapted from [147]). (b) Large single crystal outlined by red dashed line for clarity transferred on h-BN flake using the dry transfer method. (c) Hall bar of graphene on h-BN.(adapted from [148]).

Therefore studying the effect of charged impurities becomes necessary to understand their role in modifying graphene properties. Previous studies show change in conductivity and movement of Dirac point of pristine graphene upon doping with  $K^+$  ions in ultra high vacuum as shown in figure 3.23(a) [147, 149, 150]. It can be observed that the Dirac point moves as the time of deposition of  $K^+$  ions increases which is consistent with doping. Secondly the width of the minimum conductivity region broadens which means that the mobility of graphene decreases with higher  $K^+$  deposition. Similar movement of the charge neutrality was also observed by depositing charged particles on graphene transis-

tors [151, 152]. Researchers have avoided the effect of unwanted charged particles in the vicinity by encapsulating the exfoliated graphene with hexagonal boron nitride layers (h-BN) [148]. This way people have measured ballistic transport in graphene. However this technique requires micro scale alignment of individual graphene flakes and is not scalable.

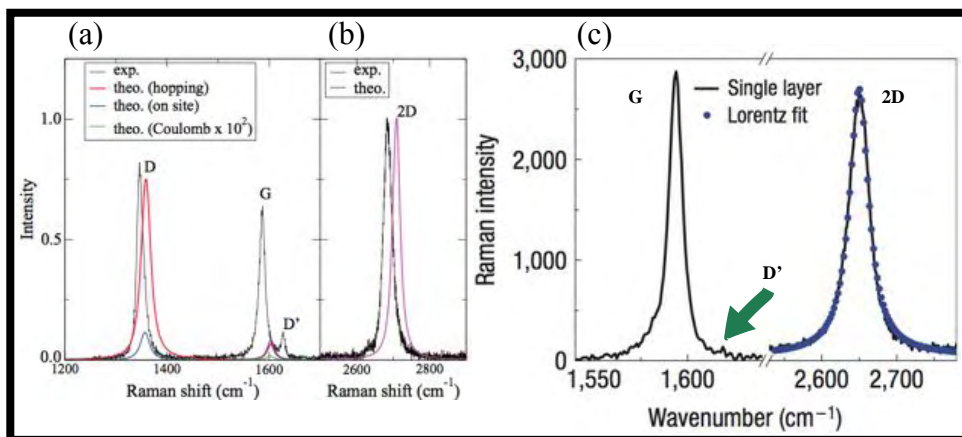


Figure 3.24: Effect of charged dopants on optical properties. (a) Calculated Raman spectra for three types of defects: hopping (red), on-site (blue) and Coulomb charge defects. The G peak is not calculated in this model and is absent in the spectrum. The black spectrum is experimental Raman data from defected graphene. (b) All calculated spectra in (a) are normalized to the calculated 2D intensity shown in pink (adapted from [153]) (c) Experimental Raman spectrum of graphene doped with  $K^+$  ions in ultra high vacuum conditions (adapted from [147]).

As mentioned in previous sub-section, Raman spectroscopy has been extensively used to study defects in graphene. In ref [153], three types of defects are mentioned. These are 1) hopping defects 2) on-site defects and 3) Coulomb defects. The Raman peaks for different kinds of defects as shown in figure 3.24(a). The black spectrum is an experimental Raman spectrum of graphene with defects for reference to the calculated peaks. The G peak in calculated spectra is absent since only those spectra originating due to double resonance (DR) mechanism is calculated. The red spectrum corresponds to peaks generated by hopping defects. Electrons are delocalized in graphene, allowing them to move in all directions by hopping between bonds. These defects, by deforming carbon-carbon bonds, affect the energy needed by electrons to hop to nearest neighbors with respect to bond length. The blue spectrum represents the on-site defects. These defects change the value of on-site potential of the carbon atoms by forming hydrogen bonds.

The green curve represents the Raman spectra due to charges defects. These defects do not disturb the lattice of graphene but are adsorbed at a distance "h" from the graphene sheet and add a Coulomb potential to the lattice points. From the calculations, the D peak is absent for charged impurities but it gives rise to small intensity D' peak which seems to be more sensitive to the charged particles. In order to enhance the Raman signal, the distance between charged impurity and carbon atom was kept at 0.27 nm, same as the  $K^+$  ion and carbon atoms in ref [147] and found it to be very small. However the calculation was done assuming a  $KC_8$  configuration i.e. one potassium ion for eight carbon atoms. Indeed the Raman spectra from the experiments in ref [147] exhibit low or almost negligible intensity of D' peak as shown by green arrow in figure 3.24(c). However all the charged particles in these experiments are externally deposited on exfoliated graphene in ultra-high vacuum conditions.

There is another method by which the graphene can be intrinsically doped with charged particles during the growth process itself. In the CVD growth of graphene, many times copper foil is used to catalyze  $CH_4$  to dissolve carbon into copper. Most often certain copper foils (Alfa Aesar, 99.8%, product no. 13382) are coated with some other materials such as Cr/ $CrO_2$  in order to avoid its oxidation. These particles may not be removed by the etching solution of the copper and hence could act as charged particle to graphene.

In the following sub-section we will show how the Cr/ $CrO_2$  coating locally enhances the electric field and induces anomalously large D' peak although the D peak intensity is small as expected from high quality graphene.

### 3.4 CREATING CHARGE DEFECTS BY CVD GROWTH

Chemical Vapor Deposition (CVD) method of growing graphene is a surface phenomenon during which the precursor,  $CH_4$  in our case, comes in contact with a catalytic surface, copper foil in our case, at  $1000^\circ C$ . The dissolved carbon atoms then segregate into hexagonal network as the temperature of copper foil is lowered. Since all this growth mechanism takes place at the surface of the copper, any kind of contaminates can play a role in the growth of graphene.

This property was used by Zhou *et al* to grow large crystal of graphene of millimeter scale. There they used the fact that any oxide layer such as  $Cu_2O$  on the copper surface would prevent the nucleation of the carbon atoms. Pure copper is highly reactive to oxygen in air and forms self-limiting  $Cu_2O$  preventing further oxidation of copper below it. By limiting the dissolution of carbon on copper, they were able to grow large grains of single crystal graphene with increasing growth time [154]. This growth method was reproduced in our group. Schematic in figure 3.25(a) illustrates the phenomenon where

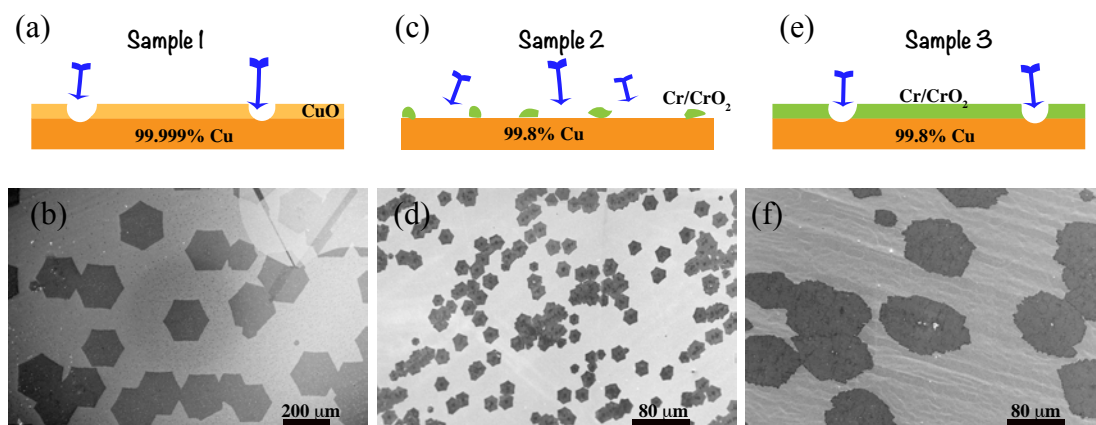


Figure 3.25: SEM images of CVD growth graphene on the different copper substrates. (a) schematic of 99.999% copper without annealing (b) SEM micrograph of sample 1. (c) and (e) schematic of 99.8% Cr coated copper with annealing with  $H_2$  at 1mbar for 1 hr and without annealing, respectively. (d) and (f) graphene grown on sample 2 and sample 3 respectively. The blue arrows point towards nucleation sites on copper.

$Cu_2O$  prevents nucleation of carbon atoms, thus decreasing nucleation centers. The SEM image in figure 3.25(b) shows single crystals of average size  $\approx 300 \mu m$  grown using the process (sample 1).

In ref [16], the copper foil used for growth was (Alfa Aesar, 99.8%, product no. 13382) coated with Cr/CrO<sub>2</sub> to prevent oxidation of copper. Here an annealing step was introduced for 1 hour before the growth process during which  $H_2$  atoms at 1mbar pressure remove any kind of contamination from the copper surface. This process also removes Cr/CrO<sub>2</sub> or  $Cu_2O$  from the copper and consequently increase nucleation density of the carbon atoms. Figure 3.25(c) and (d) show the schematic and SEM images of graphene respectively grown on the copper foil with pre-growth annealing in 100 sccm of  $H_2$  for 1 hr at 1mbar (sample 2). From the schematic, we notice that there is a large area of copper surface exposed to carbon precursor and hence the nucleation density high. Therefore the size of the single crystal grains is restricted to 30-50  $\mu m$ .

Using the same copper foil, we initiated the growth of graphene without the annealing step in order to grow large size crystals of graphene. The growth temperature is kept at 1000°C. The flow of  $CH_4$ , hydrogen and argon is kept at 4 sccm, 1000 sccm, 500 sccm respectively for a growth time of 15 minutes (sample 3). Since the annealing process is not carried out, there was a layer of Cr/CrO<sub>2</sub> left at the surface which prevented the nucleation so the size of graphene increased to around 100  $\mu m$ . The chromium particles affects the shape of graphene which is found to be irregular. Such growth also

contain multilayer patches of graphene, probably due to higher dissolution of carbon in chromium. This shows that the surface contaminants and purity of the copper foil plays a role in the growth of graphene.

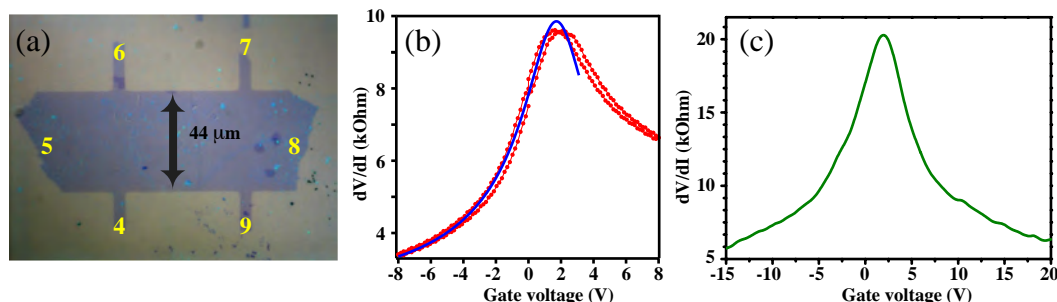


Figure 3.26: Transistor characteristics of pristine and defected graphene. (a) Charged defect graphene (Sample 3) is etched in Hall bar form with the electrodes marked in yellow. (b) Resistance measurement between electrodes 6 and 7 while applying voltage between electrodes 5 and 8 in sample 3. The blue curve gives the mobility of holes to be  $\approx 1500 \text{ cm}^2\text{V}^{-1}\text{s}^{-1}$  (Transport measurement by Mira BARAKET, postdoc, Institut Néel) (c) Four probes resistance measurement in standard CVD graphene (sample 2) with  $\approx 4000 \text{ cm}^2\text{V}^{-1}\text{s}^{-1}$ .

The hallmarks of the charged defect adsorbed on the graphene in the transport measurement are 1) decrease in the overall mobility and 2) the asymmetry of the electron and hole mobility in the resistance or conductivity curve. The decrease in mobility is due to increase in charged impurities which serve as scattering points for particle transport. Since the impurities are also charged, the scattering effect is not the same for electrons and holes giving rise to asymmetric mobilities. These effects can be observed in figure 3.23(a) where the hole mobility is higher than the electron mobility. Sample 3 was etched to form a hall bar figure 3.26(a) and connected with gold electrodes. Thereafter voltage was applied across electrodes 5 and 8 and resistance was measured across electrodes 6 and 7. The measurement was conducted at 1.5 K and is shown in figure 3.26(b). Clearly the asymmetry between hole and electron conductivity is observed with higher hole mobility. The mobility of holes is found to be  $\approx 1500 \text{ cm}^2\text{V}^{-1}\text{s}^{-1}$  from calculated spectrum in blue. A similar four probes measurement of CVD graphene without charged defects gives mobility value of around  $4000 \text{ cm}^2\text{V}^{-1}\text{s}^{-1}$  with symmetric electron and hole mobility as shown in figure 3.26(c).

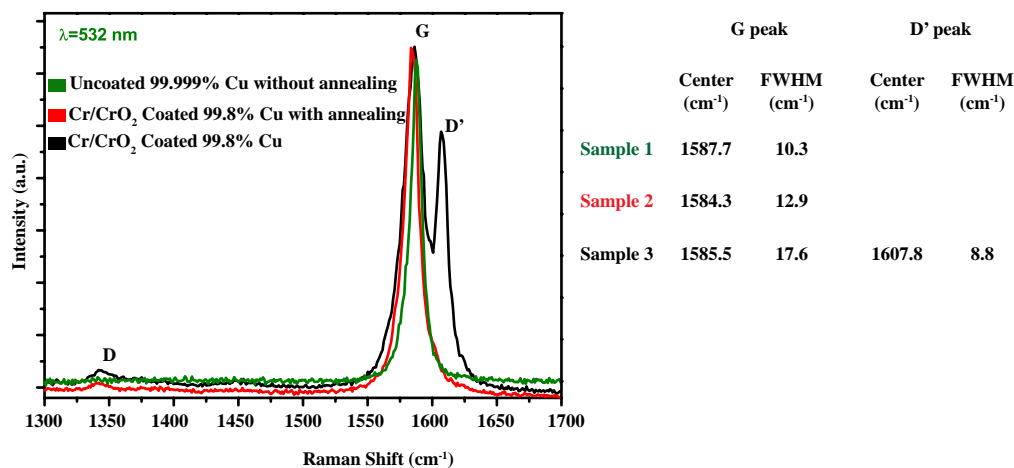


Figure 3.27: Comparison of micro-Raman spectra for different copper substrates. (samples 1, 2, 3)

### 3.5 DETECTING CHARGED DEFECTS BY RAMAN SPECTROSCOPY

Micro-Raman spectroscopy has been used to evaluate the quality of graphene. The spot size of the laser is around 300 nm and laser wavelength is 532 nm. Figure 3.27 shows the average Raman spectra of graphene after the three different samples are transferred to Si/SiO<sub>2</sub> wafer. The (green), (red), (black) represents average spectra from graphene from sample 1, sample 2 and sample 3 respectively. The G peak of sample 1, which is from 99.999% copper, has FWHM of 10.3 cm<sup>-1</sup> and has no D' band and negligible D band. In other words purity of copper foil also plays an important role in the graphene growth, though it is not relevant for the present study.

In sample 2, with Cr/CrO<sub>2</sub> coated 99.8% copper, annealing at 100 sccm of H<sub>2</sub> in 1mbar for 1 hr at 1000°C leads to cleaning of the surface contaminants (sample 2). However the G peak has FWHM of 12.9 cm<sup>-1</sup> which is higher than sample 1 and also a low intensity D peak is seen at around 1340 cm<sup>-1</sup>. Possible reasons could be that annealing process do not fully remove surface contaminants or the purity of copper foil plays a role in the D peak formation.

In sample 3, we observe an unusual high intensity of D' peak in graphene grown from Cr coated 99.98% copper which is not annealed in H<sub>2</sub> although the D peak still has very low intensity. Such high intensity of D' band is not reported earlier neither in experiments nor in theoretical studies. As mentioned earlier in figure 3.24(a), the calculated Raman spectra for hopping and on site defects contain D band whose intensity is higher than D' band as it has been also observed in chemically induced defect studies. Since the

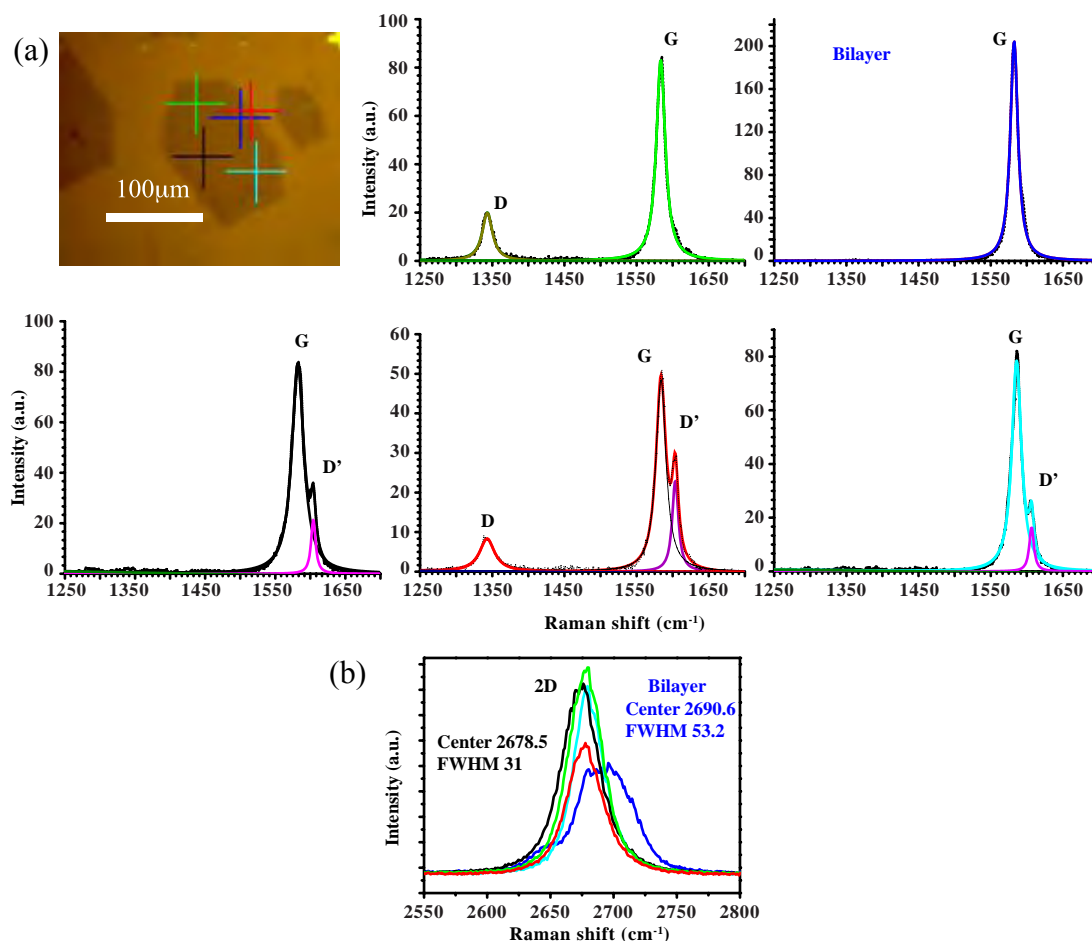


Figure 3.28: Spatial localization of highly charged defects. Optical image of transferred graphene from sample 3 on Si/SiO<sub>2</sub> and the different color (plus) signs correspond to different regions where Raman spectra were taken.

sample 3 does not have high D band, we can rule out these defects. Charge impurities give a D' band without a D band but the intensity usually is very low. This is also experimentally shown in figure 3.24(c) where intensity of D' band is almost negligible. This makes an usually higher intensity of D' band compared to D band remarkable. Besides the G peak is also found to have higher FWHM at  $17.6 \text{ cm}^{-1}$  than sample 1 and 2.

It is found that the unusual high intensity D' peak in sample 3 shown in figure 3.27 is not uniform throughout the sample. Figure 3.28 shows the Raman spectra from different parts of graphene of sample 3. The green spectrum showing D band and G band is

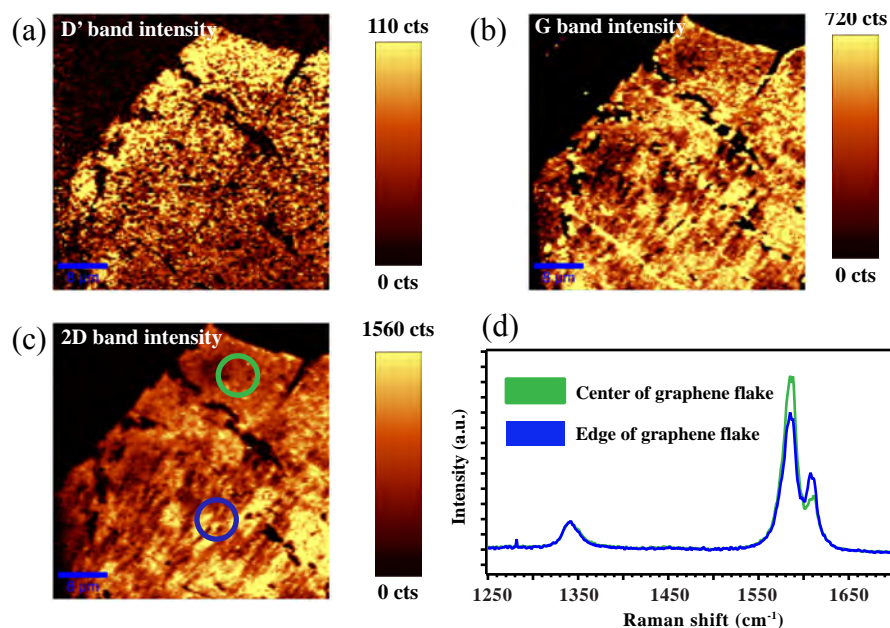


Figure 3.29: Raman spectra discrepancy between edge and center of single crystal graphene. Raman intensity mapping of sample 3 with 532nm laser (a) D' peak (b) G peak (c) 2D peak intensity mapping. (d) Average Raman spectra of edge and center of graphene as shown by blue and green circles in (c). The blue spectrum was taken from bilayer region

taken from slightly away from edge. It has no D' band and D band exist due to holes in graphene created during the transfer process. The blue spectrum has G peak intensity which is almost double than the rest of corresponding G peaks since it is taken from naturally grown double layer of graphene. It has no D and D' bands as expected from literature.

The light blue and black spectra are taken far from edge and show D' band without significant D band that can be separated from the noise. However at the edge, the D band and D' band are visible together as shown in red spectrum. The rise in intensity of D band is due to breaking of hexagonal  $sp^2$  structure at the edge.

Since it has been observed that not all points have a same intensity of D' peak from figure 3.28, we have done Raman intensity mapping of the sample 3. From figure 3.29(a), it can be seen that the intensity of D' band is higher towards the edges and decreases as we move towards the center of the graphene. But the G and 2D peak intensity Raman mappings, see figure 3.29(b) and (c), of the same area show opposite contrast. As we move towards the nucleation center of the graphene, G and 2D peak have higher intensity.



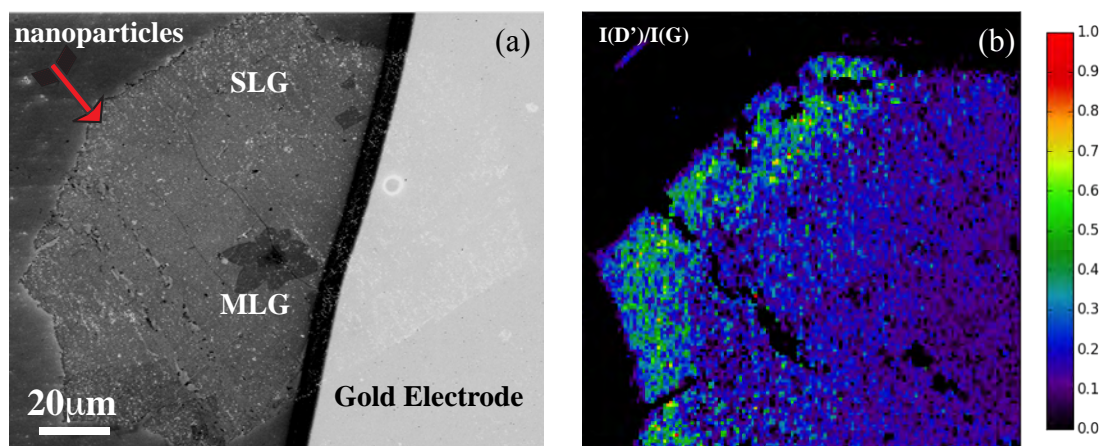


Figure 3.30: Correlation between nano particles and Raman feature. (a) SEM image of graphene from sample 3. Gold electrode is deposited on the right side of the flake. At the nucleation center of the flake, multilayer graphene (MLG) can be observed. The nano particles appear as bright spots whose density is higher at the edge of graphene than at nucleation center. (b)  $I(D')/I(G)$  mapping at the edge of sample 3.

Figure 3.29(d) shows the average Raman intensity of edges (blue) and center (green) as marked by circles in Figure 3.29(c). We note that the D band has same intensity as the regions closest to the edges were avoided since intensity of D band increases at edges. It can be observed that the average intensity of D' band is higher towards the edges (green circle) compared to regions towards the center (blue circle) of the graphene as while it is the reverse for G peak intensity. In order to understand the reason behind such contrast, we performed Scanning Electron Microscopy (SEM) of sample 3.

Corresponding SEM in figure 3.30(a) shows that the nano particles density is higher at the edges. The size of the nano particles were around 40-70 nm. Incidentally there is higher intensity of the D' band and lower intensity of G and 2D peak towards the edges than in the center region. This is also visible in the  $I(D')/I(G)$  mapping of the graphene flake as shown in figure 3.30(b). From these observations, we could also explain the role of Cr/CrO<sub>2</sub> particles in the growth of graphene as follows. Graphene nucleates at certain points on copper surface which is exposed to the CH<sub>4</sub> precursor. Due to presence of H<sub>2</sub> at 20 mbar, oxide layer is removed and is filled with carbon atoms. As graphene starts to grow outwards from nucleation center, it comes across the Cr/CrO<sub>2</sub> layer which retards the growth and gives irregular shape to graphene single crystals. These particles could also give multilayer patches due to higher dissolution of carbon in chromium.

Another way to prove the presence of charged defects in the graphene flake is by inducing structural defects. These defects are induced in a small area by electron bombardment which is then studied using Raman spectroscopy.

### 3.5.1 Creating structural defects by electron bombardment

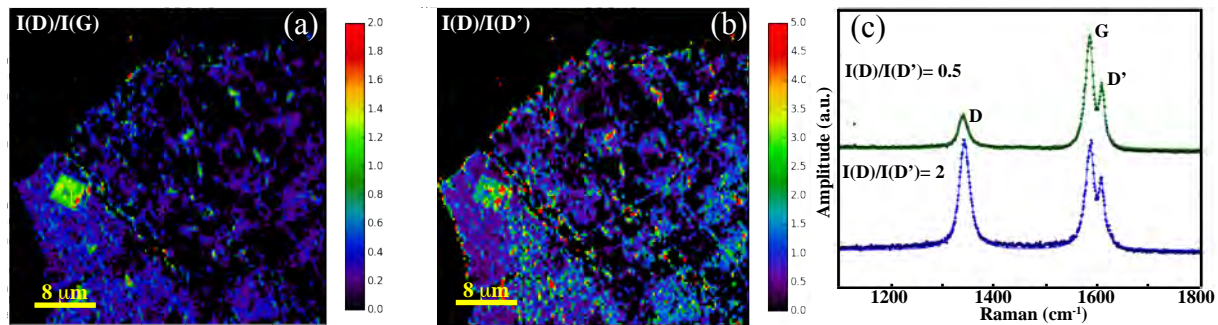


Figure 3.31: Raman study of structural defects by electron beam. (a)  $I(D)/I(G)$  and  $I(D)/I(D')$  mappings at the edge of sample 3. (c) Average spectra of charged defects (green) and structural defects (blue).

On the  $I(D)/I(G)$  mapping in figure 3.31(a), there is a rectangular region where the ratio is high i.e. the intensity of D band intensity is higher than that of G peak. In this region, electrons have been bombarded from a distance of 6 mm with 3 kVolt which gives a dose of  $\approx 10^{17}$  electrons/  $\text{cm}^2$ . Interestingly,  $I(D)/I(D')$  mapping in figure 3.31(b) show that the intensity of  $D'$  band remained unaffected while that of D band increased dramatically. This can be seen in the figure 3.31(c) where the blue spectrum is taken from within the region and green spectrum outside it. The blue spectrum resembles the spectra of defect induced by etching graphene with  $\text{Na}_2(\text{SO}_4)_2$  after 14 hours of etching. Due to electron bombardment, the structure of graphene could be amorphized [107] or bonded with hydrogen atoms [155] or knocked-out of carbon atoms [156] or deposited with carbon film [157]. In all the possible cases,  $\text{sp}^3$  bonds are created in the structure of graphene leading to destruction of graphene  $\text{sp}^2$  lattice structure and enhancement of intensity of D band in this region. Outside the rectangle, with unusual high D band and less intense  $D'$  band, we are able to rule out hopping defects (due to deformation of carbon-carbon bonds) and on-site defects (due to formation of  $\text{sp}^3$  bonds). Finally these defects can be attributed to third kind of defects which are due to charged defects.

Since such unusual ratio of  $I(D)/I(D')$  ( $= 0.5$ ) has not been observed before, we study its wavelength dependence to confirm the process of creation of these peaks by double resonance process.

### 3.5.2 Wavelength dependence

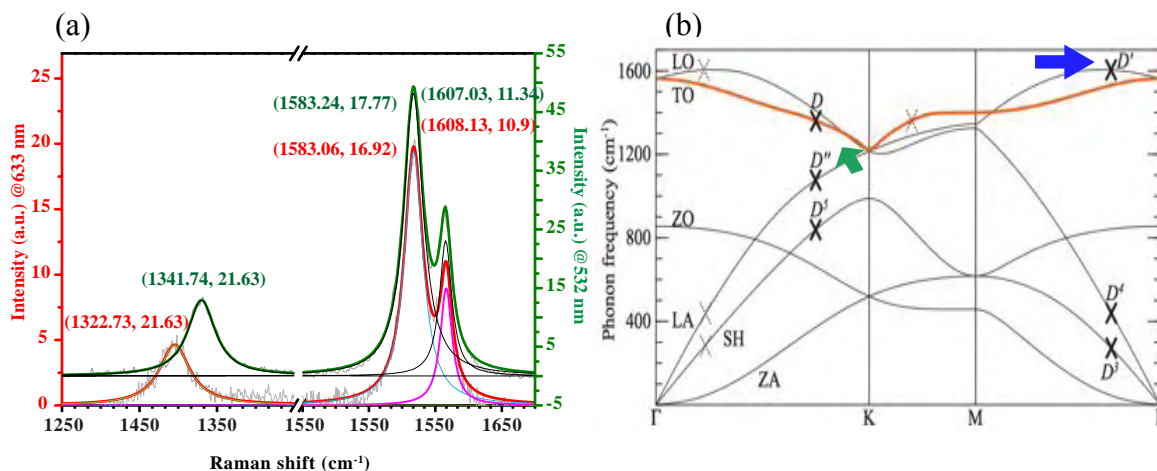


Figure 3.32: Wavelength dependency of  $D'$  optical phonon. (a) Raman spectra of sample 3 taken with 633nm (red curve) and 532nm (green curve). (b) Phonon dispersion curve of graphene (figure adapted from [153]).

Study of Raman peak with different laser wavelengths give us information regarding the process by which the Raman peak is formed. It is well known that the dispersion of D peak with laser energy is around  $50 \text{ cm}^{-1}/\text{eV}$  from ref [158, 159]. From figure 3.32(a), we find that the D peak has shifted from  $1322.73 \text{ cm}^{-1}$  to  $1341.74 \text{ cm}^{-1}$  as we move from 633 nm to 532 nm laser wavelength. This gives us a dispersion of around  $51 \text{ cm}^{-1}/\text{eV}$  which is close to value from literature. In figure 3.32(b), the frequency of D phonon is increasing away from K point as laser energy increases (see the green arrow).

$D'$  peak originates from longitudinal (LO) branch from M to  $\Gamma$  point as shown with blue arrow in figure 3.32(b). The phonon dispersion is rather flat at this point and phonon energy should have little wavelength dependence. From our experiments, we observe a change of around  $1.1 \text{ cm}^{-1}$  only from 633nm to 532nm laser as shown in figure 3.32(a). The slight change in frequency in G peak is within the error of experiments.

Thus this lack of wavelength dependency strengthens the fact that the measured phonon is the  $D'$  which is linked to charge defects. We noticed that the intensity of

D' peak depends on the density of nano particles which is linked to the strength of the electric field. Therefore we try to manipulate the intensity of D' peak by applying electric field using back-gate.

### 3.5.3 Raman scattering by back-gate doping

Since the D' band originated from charge Coulomb defect, we could possibly affect the intensity of the band by applying an electric field to the charges. In our experiment we used Si-doped substrate as back-gate with 285 nm thick SiO<sub>2</sub> dielectric to induce doping in graphene. This way we could monitor the change in the G peak and D' peak with changing the carrier density by electric field effect (EFE). In literature [68,70], it has been found that G peak stiffens and its FWHM decreases when the doping levels of electrons and holes are higher than half of the phonon energy. However when the doping level is in between half the phonon energy, the electron-phonon coupling is strong which causes phonon softening. The phonons are able to decay into electron-holes which decreases its life-time and enhances its FWHM, the so-called Kohn anomaly. This decay is not possible in higher doping level due to Pauli exclusion principle.

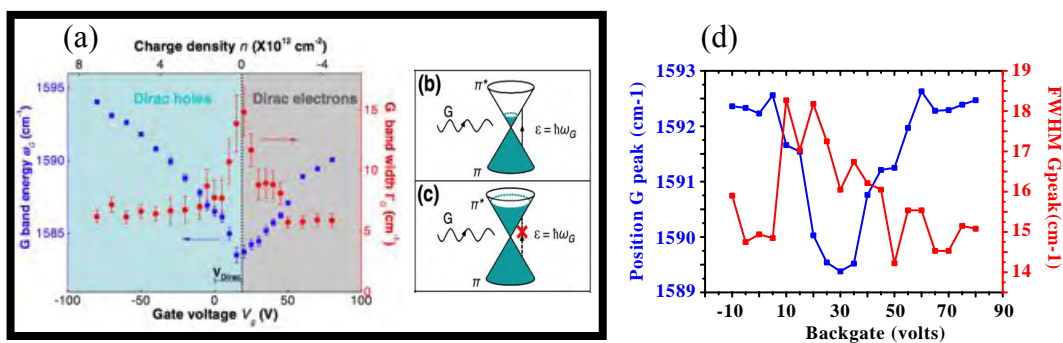


Figure 3.33: Electron-phonon coupling in CVD graphene revealed by electrostatic doping. (a) G band energy or frequency (blue squares) and FWHM (red circles) with changing gate voltage in exfoliated graphene. (b) and (c) Schematic to show G band damping process with changing Fermi-level in graphene. ( (a), (b) and (c) are adopted from [70]). (d) Plot of position (black) and FWHM (brown) of G peak in our CVD graphene from sample 3 on application of back-gate voltage.

Figure 3.33(a) shows the behavior of G peak position and FWHM on application of electric field using back-gate. The Dirac point is shifted to 30 Volt which can be explained by presence of some water molecules and charged particles trapped between graphene and SiO<sub>2</sub> during the liquid-assisted transfer process. The position (black curve) of G

peak decreases around 30 Volt due to Kohn anomaly and reaches a lower limit of  $1590\text{ cm}^{-1}$ . The FWHM (brown curve) shows high value from 5 Volt to 50 Volt as expected from literature. We note here that this is the first time that such phonon softening has been observed in CVD grown graphene at 10 K. Till now such experiment was done using exfoliated graphene sample which are not contaminated with other molecules during the transfer process. Any kind of molecules tends to affect the Fermi level in the graphene, hence adequate cleaning must be done to CVD graphene which comes in contact with water and PMMA molecules during the transfer process.

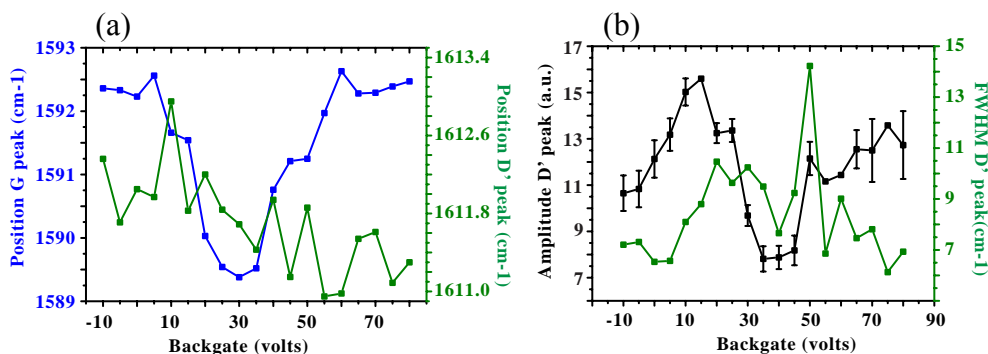


Figure 3.34: Effect of electrostatic doping on D' phonon. (a) Position of G peak (black) and D' peak (green) and (b) Amplitude (black) and FWHM (green) of D' peak on application of back-gate voltage.

Unlike the position of G peak, the position of D' peak remains almost constant as shown in figure 3.34(b). The amplitude of D' peak in figure 3.34(c) seems to oscillate but this behavior is not repeatable. Similarly for FWHM of D' peak. At present this experiment is not conclusive probably as break-down voltage of  $\text{SiO}_2$  is not very high and electric field is not sufficiently high to affect a change in intensity of D' peak. Further investigation needs to be conducted using liquid gating method where it is possible to apply high electric field.

### 3.6 CONCLUSION

In this chapter, we addressed two different kinds of defects: structural and charged defects. In one hand, we have shown how a commonly used chemical  $\text{Na}_2(\text{SO}_4)_2$  can induce structural defects depending on the exposed time. This simple wet chemical method allows us to introduce and control in simple manner the density of defects that were monitored using Raman spectroscopy.

In fact, the huge increase of the D band simultaneously with a very few holes or vacancies shown by TEM images up to 15 hours etching time, indicate that in the first etching step, the structural defects are due to the deposition of small molecules such as hydrogen. In a second step when the etching time become higher than 15 hours up to 22 hours, the non-diminishing trends in the intensity peaks of the D and D' Raman bands suggests that the chemical reaction reaches a limit in inducing defects whereas by using plasma etching or Argon bombardment, ones can totally destroyed the graphene structure.

Beyond the first-order defect related Raman bands; we also present the dependency of second order optical phonons with structural defects. These optical phonons ( $2D$ ,  $D+D'$ ,  $2D''$ ,  $D+D''$ ) show an abrupt change between the two steps described above : (i) grafting molecules followed by (ii) weakness of  $sp^2$  bond in graphene structure allowing a high sensitivity in monitoring and controlling the defects.

Finally, this study shows that the quality of graphene during the CVD growth could be high, however during the transfer process of graphene from metallic foil to other substrates, it can come in contact with common etchant such as  $Na_2(SO_4)_2$  which induces defects. Thus the origin of the defects could be mistaken to be from the growth process. Therefore it is necessary to check the effect of different chemicals on graphene before fabrication of devices.

In other hand, by using specific copper during the CVD process, we have addressed by optical phonon the possibility to detect charged defects.

We present, single crystal graphene which exhibit an unusually high intensity of D' peak compared to D peak in its Raman spectra. This observation point towards charged defects. Moreover, transport measurements performed on this graphene show an asymmetry between electron and hole graphene mobility as expected for charge defects.

Finally, the spatially resolved Raman maps show an inhomogeneous D' intensity throughout these graphene flakes: intensity was higher towards the edge of the flakes compared to its center. This observation is correlated with the higher density of Cr/CrO<sub>2</sub> nanoparticles at the edges observed by SEM giving insights into the growth mechanism.



## CONCLUSION

---

Graphene is now driving outstanding advances in nanoelectronics, still fundamental issues need to be addressed to optimize graphene integration and make functional devices. This thesis addresses from the growth of high quality graphene, transferring it to different substrates to fabricate novel applications and engineering defects into it.

In chapter 1, we have managed to improve two main aspects of classical CVD graphene growth technique.

Firstly we increased the growth scale of graphene to wafer scale and secondly we provided insights on mechanism to decrease the nucleation density of graphene in order to grow sub-millimeter size single crystal graphene.

We have managed to grow large area graphene ( $15 \times 20 \text{ cm}^2$ ) while keeping the advantages if pulsed CVD growth. This was achieved by rolling the copper foil in the CVD chamber in such a way that it avoids touching itself. This way we were able to grow wafer scale graphene without increasing the size of the CVD chamber. It is a energy saving technique, since the energy required to operate the chamber remains same as that of growing smaller area graphene.

We give insights into the mechanism of decreasing the nucleation density of graphene by creating a barrier oxide layer and studying effects of partial pressure of gasses. Growing a thicker layer of  $\text{Cu}_2\text{O}$  retards the growth of graphene by preventing carbon precursor to come in contact with copper. The thickness of  $\text{Cu}_2\text{O}$  layer can be varied by preheating the copper foil in oxygen. The larger the thickness of the  $\text{Cu}_2\text{O}$  layer, lesser is the nucleation density and larger are the single crystal grains. The nucleation density can be further decreased adjusting the partial pressure of  $\text{H}_2$ ,  $\text{CH}_4$  and Ar gasses. This way we have managed to grow single crystal graphene of  $300 \mu\text{m}$  in size.

In chapter 2, we have demonstrated the fabrication of novel graphene-based devices by optimizing liquid-assisted transfer method.

We have identified the problems related to the transfer process for creating a artificially transferred bilayer graphene and optimized it to make graphene crossbar. From confocal spatially resolved Raman spectroscopy, we demonstrated that the two artificially transferred graphene stack behaved as natural bilayer system. The strong interaction between two layers is not restricted to small area but to the whole centimeter scale surface that we fabricated. The same phenomenon was used to classify crystallinity of hexagonal and octagonal graphene flakes obtained by our CVD technique. We have found that hexagonal



graphene flakes were single crystal while octagonal graphene flakes were polycrystalline in nature.

We developed a new method of suspending graphene by transferring it on pillared substrate in order to engineer its mechanical and electronic properties by strain. We found that below a critical distance between pillars, graphene membrane remained fully suspended at macroscopic scale. Raman spectroscopy showed that the strain in such a system was less than 0.2% which is much lower than other suspended devices. In order to get an operating device, a specific process has been developed using transparent, flexible stencil mask which can be aligned over a specific graphene flake. This way electrodes were fabricated on suspended graphene in a completely dry way and without damaging graphene.

Graphene was transferred to different substrates such as GaN quantum well LED, where it was used as transparent electrode. Though not optimized, we found that injection of carriers into the quantum LED was possible in a much larger area compared to a standard metallic mesh electrodes. Finally graphene transfer method was scaled up to transfer graphene on 4 inches silicon and sapphire substrates. And a new technique to transfer graphene to flexible substrate was developed which is being patented.

In chapter 3, we have demonstrated methods to engineer defects into graphene in controllable way.

We have developed a chemical route to induce defects in CVD graphene and characterize it. We have shown how a common chemical  $\text{Na}_2(\text{SO}_4)_2$ , which is usually used to etch the copper foil, is able to induce defects in graphene. Very often the origin of such defects are mistaken to exist during the growth process. Thereafter we have developed a protocol to control the defects with time. From the defects assisted phonons (D and D' peaks) and TEM images, we proposed a new mechanism of etching graphene by chemicals. Small molecules such as hydrogen are grafted onto graphene in the structure before reaching a saturation limit beyond which the chemical reaction is no more able to induce defects. We also studied the evolution of the defect formation using second order phonons (2D and 2D' peaks) and two phonon processes (D+D' and D+D'').

Chemically induced defects involves destroying intrinsic structure of graphene which can be avoided by engineering the properties of graphene by adsorbing charged particles on its surface. In the last chapter we demonstrate, for the first time, that intrinsic charged doping is possible during the growth when the copper foil is contaminated with Cr/CrO<sub>2</sub> particles. Due to such contamination, we observe an unusually high intensity D' band compared to the D band. A higher intensity of D' band compared to D band has not been reported before. We find that the intensity of D' band is higher towards the edge of graphene flake compared to the center, which gives insights into the growth mechanism of graphene. As expected from the literature for charged doping, overall

mobility dropped and there was asymmetry between the electron and hole mobility.

## PERSPECTIVES

Beyond advances presented in this thesis, there are still a lot of issues that need to be addressed before graphene-based devices reach an industrial scale. Some of the immediate issues regarding this work that need to be addressed are as follows:

### *Graphene single crystals at the wafer scale*

The size of the single crystal can be further increased to wafer scale by investigating the role of oxide layer, partial pressure of precursor and etching gases and the time of growth. Presently the decrease in nucleation density is closely related to the slow rate of growth of graphene crystals. Therefore growth time for single crystals is long. In order to be efficient, new methods should be explored to decrease the nucleation density while keeping a high rate of growth of crystals.

### *Novel heterostructure devices*

Since we have been able to fabricate artificial bilayer crossbars, it would be interesting to observe the inter-layer transport of the system. In future, single crystal graphene could be used to make crossbars to see the effect of orientation between top and bottom layers on the transport measurement. Photon absorbing or magnetic molecules can be trapped between the graphene layers to study the photovoltaic effect or magneto-transport properties. The crossbar can then be used as a transparent and conducting cell to measure encapsulated species.

### *Microscopic suspended graphene devices*

Till now transport measurements have shown very high mobility for nanoscale to few micron scale suspended graphene. We need to investigate if the same holds true for microscopic scale suspended graphene. This would open the way to very high aspect ratio NEMS: macroscopic in plane and atom-thick out of plane bringing enhanced sensitivity. This system could also find applications in highly sensitive large area opto-mechanical graphene sensors and used as substrate for Graphene Enhanced Raman Spectroscopy (GERS) effect.

### *Defect engineering at large scale*

We have shown that it is possible to induce defects by chemical method using standard etchants. However more such chemicals should be investigated so that doping level, mobility, chemical structure can be engineered according to the needs of the applications. Such capabilities could lead to better coupling between the graphene and p-doped GaN layer in AlGaIn/GaN quantum well LED to enhance the efficiency of carrier injections. Doped graphene could also be used for large uniform Joule heating surface by passing current through it.

*Defect engineering with charged defects*

Presently the Cr/CrO<sub>2</sub> particles are randomly present on the surface of copper foil. Growth of graphene on such surfaces gives unusual high intensity of D' band. In future, we need to study the magnitude of electric field created by the nano particles and the structure of graphene. This way we will be able to distinguish between structural defects and charged defects at the atomic scale. The spacing and periodicity between the nano particles could play an important role in the global transport properties which needs to be investigated.

From physical investigation of phenomenon affecting graphene structure and quality at the nanoscale, graphene growth should become in the near future fully automatized so as to reduce cost, increase production and ensure reproducible quality. Graphene production is still at its premises, and also are its applications. From a personal point of view, graphene may not displace present day materials. It will rather provide outstanding performances for very specific applications which can now be envisioned from the specific properties of graphene such as high mobility Dirac Fermions or neutral transparency. Let us not make old devices with this new material but rather experience new concepts with it.

## APPENDIX 1: THEORY OF RAMAN SPECTROSCOPY IN GRAPHENE

---

When an incoming light interacts with atoms of material, it is scattered elastically or inelastically. The elastic phenomenon is called Thomson or Rayleigh scattering. Here the momentum ( $k$ ) of the incoming light  $k_i$  and outgoing light  $k_s$  wave is same. In case they are not same ( $k_i \neq k_s$ ), then it is considered inelastic scattering. In case of inelastic scattering in the wavelength from near infrared to near UV region, it is known as Raman scattering. All the scattering follows the laws of momentum and energy conservation as follows

$$\mathbf{k}_s = \mathbf{k}_i \pm \mathbf{q}$$
$$\omega_s = \omega_i \pm \omega$$

where  $\mathbf{k}$  and  $\omega$  are momentum and frequency of the waves considered.

The different forms of inelastic scattering processes are shown in figure 3.35(a) where the  $\omega_i \neq \omega_s$ . In the infra-red (IR) spectroscopy, only those wavelengths whose energy is equivalent to difference in two vibrational states of electronic ground state of energy of the system is absorbed without emission. In Stokes Raman, the incoming photon of any wavelength is scattered and transfers some energy to the system, so its wavelength changes. It is as if an electron were excited from the lowest energy state to another vibrational state, going through an intermediate virtual state. If it is absorbed from higher vibrational state of ground state and emits higher energy photon to go to the lowest state, then it is called Anti-Stokes Raman.

The classical Raman cross section is much lower than the elastic scattering (1 in millions). Therefore various kinds of filters such as notch filter are used to absorb the Rayleigh light while collecting the scattered light. However the Raman cross section can be improved by using Resonance Raman scattering. In this case, the wavelength of the incoming photon can be tuned to exactly match the energy difference between two electronic states as shown in figure 3.35(a). It increases the number of excited electron-hole pairs which then resonantly recombine in another vibrational state of electronic ground state. This is first order resonance Raman scattering.

In all these cases, the momentum of the waves imparts a negligible momentum to the phonon hence phonon momentum is approximately equal to zero. From the dispersion relation of the graphene in figure 3.36, we should be able to see three phonons at the  $\Gamma$

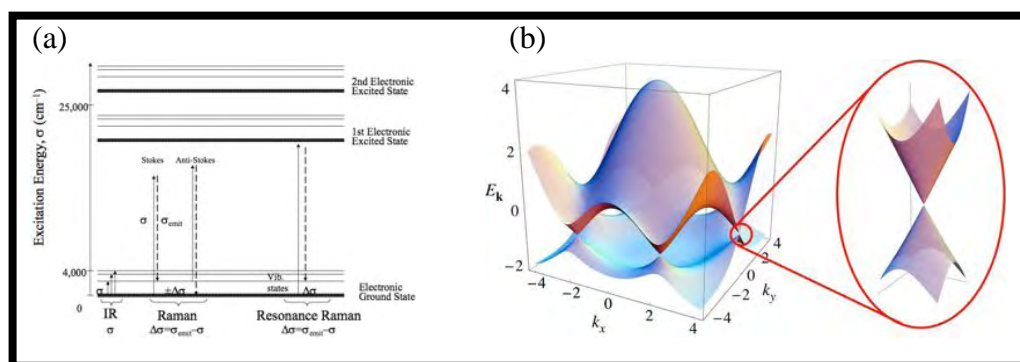


Figure 3.35: (a) Principle of inelastic scattering: Infra-red (IR), Stokes, Anti-Stokes Raman and resonant Raman spectroscopy. (Figure adapted from [160]) (b) Electronic band diagram of graphene (Figure adapted from [161])

point, namely acoustic phonons, oTO phonon at  $\approx 880 \text{ cm}^{-1}$  and iLO or iTO phonons at  $\approx 1580 \text{ cm}^{-1}$ . However due to selection rules only the phonon at  $\approx 1580 \text{ cm}^{-1}$  is visible and gives rise to the so-called G peak, which belongs to the first order. This peak is present in  $sp^2$  carbon materials though its shape depends on the type of materials. It is doubly degenerate and originates from the iTO and iLO phonons at  $\Gamma$  point. The degeneracy of this phonon can be lifted by applying strain in the graphene system where the G peak splits into  $G^+$  and  $G^-$ .

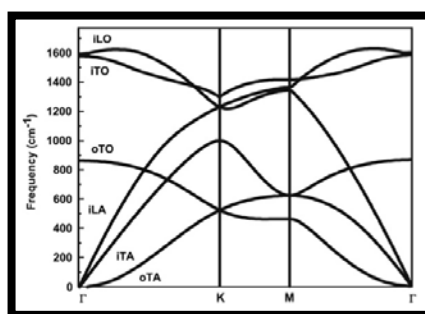


Figure 3.36: Phonon dispersion relation of single layer graphene. (figure adapted from [162])

Graphene is a single layer honeycomb lattice of carbon atoms so the Raman signal from such system should be very low. However the electronic band diagram of graphene, shown in figure 3.35(b) is such that it always fulfills the condition for resonance Raman spectroscopy for any wavelength of laser [163]. This is due to the Dirac cones at  $K$  point where bands are linear and has no bandgap as shown in the enlarged image.

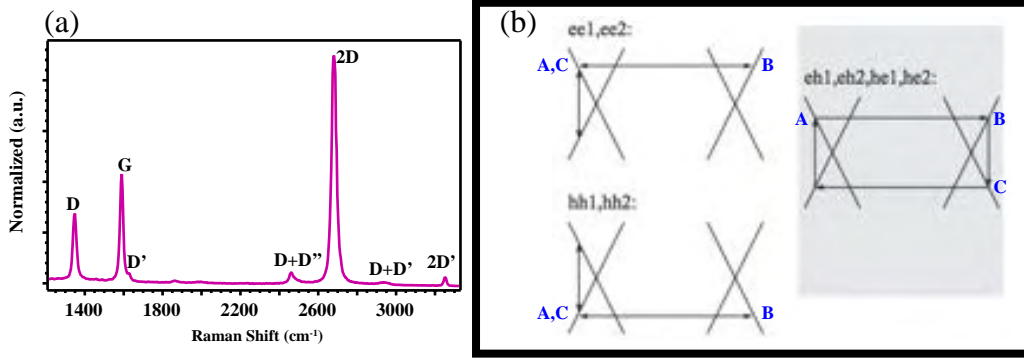


Figure 3.37: (a) Raman spectrum on defected graphene. (b) The crosses represent the Dirac cones at  $K$  and  $K'$  of electronic state of graphene. The vertical lines are creation and annihilation of the electron/hole pair. The horizontal lines represent scattering from defects or phonons. e and h are electrons and holes respectively (figure adapted from [164])

The Raman spectrum of a defected graphene is shown in figure 3.37(a). As it can be observed, there are other Raman bands such as D, D', whose positions do not match any phonon energy at the  $\Gamma$  point. Besides there are bands like 2D with frequency of  $\approx 2700 \text{ cm}^{-1}$  which are well above frequencies in phonon dispersion relation. The presence of these bands cannot be explained by classical Raman scattering at  $\Gamma$ . Therefore another mechanism was developed to where scattering could take place in different momentum space.

### Double Resonance Theory

In the Double Resonance (DR) theory, incoming photon of any wavelength excites electron/ hole pairs in the electronic band structure. The carriers are then scattered twice either by phonons or defects, inelastically or elastically respectively. Thereafter the electron-hole pair recombines to emit a photon with lesser energy. The light-electron, electron-phonon and defect induced electron-electron interactions are treated as first order of the perturbation theory. The Raman cross section of the light scattered by the crystal is given by the Fermi golden rule to the forth order:

$$I \propto \sum_f \left| \sum_{A,B,C} \frac{M_{fc} M_{cb} M_{ba} M_{ai}}{(e_i - e_c - i\frac{\gamma^C}{2})(e_i - e_b - i\frac{\gamma^B}{2})(e_i - e_a - i\frac{\gamma^A}{2})} \right|^2 \delta(e_i - e_f)$$

where  $e_i$  and  $e_f$  are energies of the initial and final states of the system.  $e_a, e_b, e_c$  are the energies of the intermediate virtual steps A, B, C ( see figure 3.37(b)) of the process

during which the one or two phonons are emitted.  $\gamma^A, \gamma^B, \gamma^C$  are their inverse lifetimes of the electronic excitations.  $M_{mn}$  is the first order scattering matrix between virtual states. In our case  $M_{ai}$  and  $M_{cf}$  correspond to creation and recombination matrices of electron-hole pairs in  $\pi$  and  $\pi^*$  bands.  $M_{ab}$  and  $M_{bc}$  are scattering matrices of the virtual states. In case of resonance effect, one of the terms in the denominator is minimal, which enhances the intensity of Raman peaks.

We note here that, after electrons and holes are created by absorption of photons, both of them can be scattered by defects and phonons. These carriers are then scattered twice before getting annihilated. There are two possible cases: 1) the carrier is scattered by a defect and by a phonon or 2) the carriers are scattered by two phonons of opposite momenta. In general, the higher order process of Raman lines are of low intensity. However in graphene, two of the terms in denominator could be minimal, due to which intensity of the second order Raman peaks could be as high as the first order process. This is a double resonance condition.

Assuming that the temperature is low enough and the carriers are at the lowest energy state, hence only the Raman Stokes lines are relevant, we write the intensity of the Raman lines as function of energy or frequency as

$$I(\omega) = \frac{1}{N_q} \sum_{q,u} I_{qu}^{pd} \delta(\omega_l - \omega - \omega_{-q}^u) [n(\omega_{-q}^u) + 1] + \frac{1}{N_q} \sum_{q,u,v} I_{quv}^{pd} \delta(\omega_l - \omega - \omega_{-q}^u - \omega_{+q}^v) [n(\omega_{-q}^u) + 1] [n(\omega_{+q}^v) + 1]$$

where  $I_{qu}^{pd}$  is the probability to excite a phonon in "u" branch with momentum  $\mathbf{q}$  and energy  $\hbar\omega_{-q}$  in the defect-phonon process. Similarly  $I_{quv}^{pd}$  is the probability to excite two phonons in two phonon process.  $N_q$  is the number of phonons with momentum  $\mathbf{q}$  in the phonon branch u and v.  $\delta(\omega)$  is the Dirac delta function while  $n(\omega)$  is Bose-Einstein distribution.

In each of the phonon branches as shown in figure 3.36, there are different types of scattering process such as *ee1* (*electron electron scattering process*) where only the electrons get scattered. In case of D band, the electron is elastically scattered to  $\mathbf{K}'$  and then second scattering event is inelastic in nature due to defects which scattered the electron to  $\mathbf{K}$ . Thereafter the electron-hole recombines to emit a photon with lesser energy. The order of scattering can be reverse to give rise to *ee2* process. Similar process can take place for only holes (*hh1* and *hh2*) and combinations of electrons and holes (*eh1*, *eh2*, *he1* and *he2*) as show in figure 3.37(b). Taking into account all the possibilities of scattering process, combinations of electrons and holes, the probabilities to excite phonons are written as

$$I_{\mathbf{q}\mathbf{u}}^{\text{pd}} = N_d \left| \frac{1}{N_k} \sum_{\mathbf{k}, \mathbf{a}} K_a^{\text{pd}}(\mathbf{k}, \mathbf{q}, \mathbf{u}) \right|^2$$

$$I_{\mathbf{q}\mathbf{u}\mathbf{v}}^{\text{pp}} = \left| \frac{1}{N_k} \sum_{\mathbf{k}, \mathbf{a}, \mathbf{b}} K_b^{\text{pp}}(\mathbf{k}, \mathbf{q}, \mathbf{u}, \mathbf{v}) \right|^2$$

where  $K_a^{\text{pd}}$  and  $K_b^{\text{pp}}(\mathbf{k}, \mathbf{q}, \mathbf{u}, \mathbf{v})$  are amplitudes of the different double resonance processes that can take place over the electronic wave vectors. The various combinations of scattering processes are labeled as a and b indices. These represent the various combinations of scattering labeled as  $ee1$ ,  $ee2$ ,  $hh1$ ,  $hh2$ ,  $eh1$ ,  $eh2$ ,  $he1$ ,  $he2$ . Here  $e$  and  $h$  represents electrons and holes respectively.  $I_{\mathbf{q}\mathbf{u}}^{\text{pd}}$  is assumed to linearly depend on the number of defects ( $N_d$ ) in graphene.

Though all the possible combinations of carrier scattering is possible, their amplitudes  $K_a^{\text{pd}}$ ,  $K_b^{\text{pp}}$  are different depending on the type of scattering. An example to calculate the amplitude of  $K_{ee1}^{\text{pd}}$  is shown below.

$$K_{ee1}^{\text{pd}} = \frac{\langle \pi(\mathbf{k}) | D_{\text{in}} | \pi^*(\mathbf{k}) \rangle \langle \pi^*(\mathbf{k}+\mathbf{q}) | \Delta H_{\mathbf{q},\mathbf{u}} | \pi^*(\mathbf{k}) \rangle \langle \pi^*(\mathbf{k}) | \Delta H_{\mathbf{D}} | \pi^*(\mathbf{k}+\mathbf{q}) \rangle \langle \pi^*(\mathbf{k}) | D_{\text{out}} | \pi(\mathbf{k}) \rangle}{(e_i - e_c - i\frac{\gamma^C}{2})(e_i - e_b - i\frac{\gamma^B}{2})(e_i - e_a - i\frac{\gamma^A}{2})}$$

The first process  $ee1$  represents a laser exciting an electron with momentum  $\mathbf{k}$ . So the scattering matrix is written as  $M_{A_i} = \langle \pi(\mathbf{k}) | D_{\text{in}} | \pi^*(\mathbf{k}) \rangle$  where  $D_{\text{in}}$  is the coupling operator between laser light and crystal. This electron is then scattered to a state  $\mathbf{k}+\mathbf{q}$  by a phonon  $-\mathbf{q}$ . This is given by a scattering matrix  $M_{B_\Lambda} = \langle \pi^*(\mathbf{k}+\mathbf{q}) | \Delta H_{\mathbf{q},\mathbf{u}} | \pi^*(\mathbf{k}) \rangle$ . Here  $\Delta H_{\mathbf{q},\mathbf{u}}$  is the electron-phonon coupling parameter. This electron is scattered back to  $\mathbf{k}$  state by a defect given by matrix element  $M_{B_C} = \langle \pi^*(\mathbf{k}) | \Delta H_{\mathbf{D}} | \pi^*(\mathbf{k}+\mathbf{q}) \rangle$  with  $H_{\mathbf{D}}$  is the electron-defect coupling operator. Finally this electron-hole pair recombines to give a photon. This coupling is given by  $M_{C_f} = \langle \pi^*(\mathbf{k}) | D_{\text{out}} | \pi(\mathbf{k}) \rangle$  with  $D_{\text{out}}$  as coupling parameter. In this case  $e_i = \epsilon_L$  i.e. the laser energy.  $e_a = \epsilon_{\mathbf{k}}^{\pi^*} - \epsilon_{\mathbf{k}}^{\pi}$ ;  $e_b = \epsilon_{\mathbf{k}+\mathbf{q}}^{\pi^*} - \epsilon_{\mathbf{k}}^{\pi^*} + \omega_{-\mathbf{q}}$ ;  $e_c = \epsilon_{\mathbf{k}}^{\pi^*} - \epsilon_{\mathbf{k}+\mathbf{q}}^{\pi^*} + \omega_{-\mathbf{q}}$ . Similarly other amplitudes for other processes can be calculated.

Using the equations mentioned above, the phonons contributing most to graphene Raman signal are calculated along the high symmetry lines for  $\epsilon_L = 2.4$  eV as shown in figure 3.38(a). The  $D$ ,  $D'$  and  $D''$  are high intensity peaks while  $D^3$ ,  $D^4$  and  $D^5$  are low intensity peaks. The  $D$  and  $2D$  peaks arise due to breathing modes (iTO phonon) at  $\mathbf{K}$ . The different double resonance processes of creation of these phonons are shown in



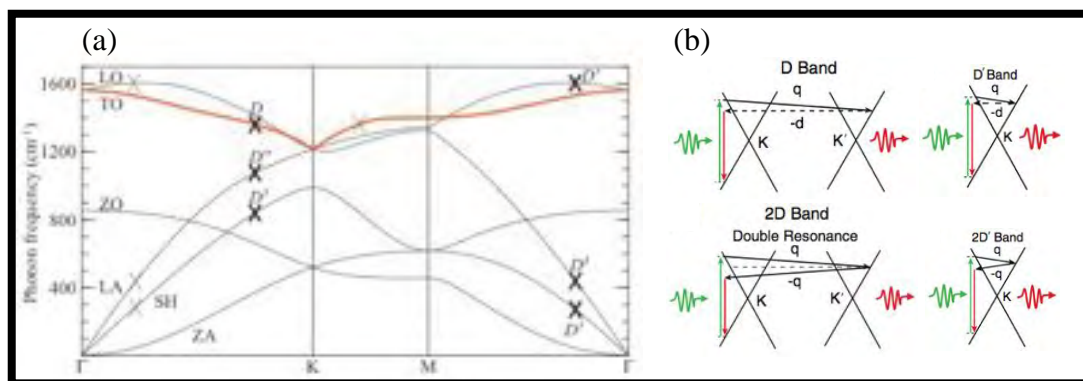


Figure 3.38: (a) Phonon band diagram of single layer graphene for  $\epsilon_1 = 2.4$  eV. (figure adapted from [164]) (b) Examples of  $ee_1$  (*electron electron scattering process*) Inter-valley scattering process gives rise to D and 2D bands while intra-valley process gives rise to D' and 2D' bands. The horizontal dotted and plain arrows represent defect and phonon scattering respectively. (figure adapted from [165])

figure 3.38(b). Both the D and 2D are inter-valley processes. However compared to the defect assisted D peak, the 2D peak originates from the same phonon scattered twice, hence it has double the frequency of the D peak. There are also intra-valley scattering processes such as D' and 2D' bands. Both D and D' bands originate from defects in the system. D+D'' and D+D' peaks are two phonon processes while 2D' peak is second order peak of D' peak. All the graphene peaks are affected differently by defects in graphene, hence a separate chapter has been dedicated to it.

#### Instrumentation

The set-up for confocal Raman measurement is shown in figure 3.39. The laser sources are solid-state and Helium-Neon which produces laser wavelength of 532 nm and 633 nm respectively. The laser is guided to the pinhole using a optical fibre. The pinhole is at the focal point of collimation lens which helps to adjust the focus of laser beam onto the sample. The laser from the source is plane-polarized and half wave plate ( $\lambda/2$ ) can be used to rotate the plane of polarization. The quarter wave plate ( $\lambda/4$ ) is used to turn the plane-polarized laser to circularly-polarized laser. The laser beam falls on the 50/50 beam splitter which directs the laser towards the objectives. They focus the laser onto the sample and also collect the reflected light at the same time. However only the light reflected from the focal plane of the objectives reaches the spectrometer due to the confocality of the microscope. The notch filter absorbs most of the Rayleigh light scattered which allows Raman signal to be visible. The reflected light is then guided by

an optical fibre to a spectrometer where the wavelengths are analyzed and intensity of the wavelength is counted using CCD camera.

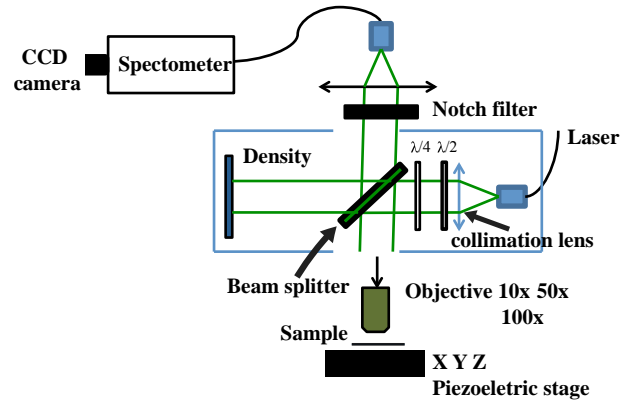


Figure 3.39: Working principle of Raman microscope

### Conclusion

Though classical Raman theory is unable to explain the high intensity of peaks in graphene, Double Resonance (DR) helps explain the different phonon modes. The electronic band structure of graphene is such that condition for resonance Raman spectroscopy is fulfilled for all laser wavelengths. Such properties allow for double resonance conditions, hence we are able to observe second order peaks. Some of the peaks modes are defect-assisted such as D and D' peaks, while others are two phonon processes (D+D' and D+D'' ) or second order processes (2D and 2D'). However all the peaks are affected by defects differently, hence can be used to identify different types of defects.



## REFERENCE

---

- [1] K. S. Novoselov, A. K. Geim, S. V. Morozov, D. Jiang, Y. Zhang, S. V. Dubonos, I. V. Grigorieva, and A. A. Firsov, "Electric field effect in atomically thin carbon films," *Science*, vol. 306, no. 5696, pp. 666–669, 2004.
- [2] A. Geim, "Graphene: Status and prospects," *Science*, vol. 324, no. 5934, pp. 1530–1534, 2009.
- [3] A. Geim, "Nobel lecture: Random walk to graphene," *Rev. Mod. Phys.*, vol. 83, pp. 851–862, Aug 2011.
- [4] K. Novoselov, "Nobel lecture: Graphene: Materials in the flatland," *Rev. Mod. Phys.*, vol. 83, pp. 837–849, Aug 2011.
- [5] A. Castro Neto, F. Guinea, N. Peres, K. Novoselov, and A. Geim, "The electronic properties of graphene," *Rev. Mod. Phys.*, vol. 81, pp. 109–162, Jan 2009.
- [6] S. Morozov, K. Novoselov, M. Katsnelson, F. Schedin, D. Elias, J. Jaszczak, and A. Geim, "Giant intrinsic carrier mobilities in graphene and its bilayer," *Phys. Rev. Lett.*, vol. 100, p. 016602, Jan 2008.
- [7] X. Du, I. Skachko, A. Barker, and E. Y. Andrei, "Approaching ballistic transport in suspended graphene," *Nat Nano*, vol. 3, pp. 491–495, 08 2008.
- [8] K. Bolotin, K. Sikes, J. Hone, H. Stormer, and P. Kim, "Temperature-dependent transport in suspended graphene," *Phys. Rev. Lett.*, vol. 101, p. 096802, Aug 2008.
- [9] A. S. Mayorov, R. V. Gorbachev, S. V. Morozov, L. Britnell, R. Jalil, L. A. Ponomarenko, P. Blake, K. S. Novoselov, K. Watanabe, T. Taniguchi, and A. K. Geim, "Micrometer-scale ballistic transport in encapsulated graphene at room temperature," *Nano Letters*, vol. 11, no. 6, pp. 2396–2399, 2011. PMID: 21574627.
- [10] M. Han, B. Özyilmaz, Y. Zhang, and P. Kim, "Energy band-gap engineering of graphene nanoribbons," *Phys. Rev. Lett.*, vol. 98, p. 206805, May 2007.
- [11] Z. Chen, Y.-M. Lin, M. J. Rooks, and P. Avouris, "Graphene nano-ribbon electronics," *Physica E: Low-dimensional Systems and Nanostructures*, vol. 40, pp. 228–232, 12 2007.

- [12] Y. Zhang, J. P. Small, W. V. Pontius, and P. Kim, "Fabrication and electric-field-dependent transport measurements of mesoscopic graphite devices," *Applied Physics Letters*, vol. 86, no. 7, pp. –, 2005.
- [13] M. C. Lemme, T. Echtermeyer, M. Baus, and H. Kurz, "A graphene field-effect device," *Electron Device Letters, IEEE*, vol. 28, pp. 282–284, April 2007.
- [14] Y.-M. Lin, K. A. Jenkins, A. Valdes-Garcia, J. P. Small, D. B. Farmer, and P. Avouris, "Operation of graphene transistors at gigahertz frequencies," *Nano Letters*, vol. 9, no. 1, pp. 422–426, 2009. PMID: 19099364.
- [15] J.-H. Ahn and B. H. Hong, "Graphene for displays that bend," *Nat Nano*, vol. 9, pp. 737–738, 10 2014.
- [16] Z. Han, A. Kimouche, D. Kalita, A. Allain, H. Arjmandi-Tash, A. Reserbat-Plantey, L. Marty, S. Pairis, V. Reita, N. Bendiab, J. Coraux, and V. Bouchiat, "Homogeneous optical and electronic properties of graphene due to the suppression of multilayer patches during cvd on copper foils," *Advanced Functional Materials*, vol. 24, no. 7, pp. 964–970, 2014.
- [17] H. Zhou, W. J. Yu, L. Liu, R. Cheng, Y. Chen, X. Huang, Y. Liu, Y. Wang, Y. Huang, and X. Duan, "Chemical vapour deposition growth of large single crystals of monolayer and bilayer graphene," *Nat Commun*, vol. 4, 06 2013.
- [18] L. Gan and Z. Luo, "Turning off hydrogen to realize seeded growth of subcentimeter single-crystal graphene grains on copper," *ACS Nano*, vol. 7, no. 10, pp. 9480–9488, 2013. PMID: 24053313.
- [19] A. W. Cummings, D. L. Duong, V. L. Nguyen, D. Van Tuan, J. Kotakoski, J. E. Barrios Vargas, Y. H. Lee, and S. Roche, "Charge transport in polycrystalline graphene: Challenges and opportunities," *Advanced Materials*, vol. 26, no. 30, pp. 5079–5094, 2014.
- [20] R. B. McLellan, "The solubility of carbon in solid gold, copper, and silver," *Scripta Metallurgica*, vol. 3, no. 6, pp. 389 – 391, 1969.
- [21] X. Li, W. Cai, J. An, S. Kim, J. Nah, D. Yang, R. Piner, A. Velamakanni, I. Jung, E. Tutuc, S. K. Banerjee, L. Colombo, and R. S. Ruoff, "Large-area synthesis of high-quality and uniform graphene films on copper foils," *Science*, vol. 324, no. 5932, pp. 1312–1314, 2009.
- [22] S. Bae, H. Kim, Y. Lee, X. Xu, J.-S. Park, Y. Zheng, J. Balakrishnan, T. Lei, H. Ri Kim, Y. I. Song, Y.-J. Kim, K. S. Kim, B. Ozyilmaz, J.-H. Ahn, B. H. Hong, and S. Iijima,

- "Roll-to-roll production of 30-inch graphene films for transparent electrodes," *Nat Nano*, vol. 5, pp. 574–578, 08 2010.
- [23] T. Kobayashi, M. Bando, N. Kimura, K. Shimizu, K. Kadono, N. Umezue, K. Miyahara, S. Hayazaki, S. Nagai, Y. Mizuguchi, Y. Murakami, and D. Hobara, "Production of a 100-m-long high-quality graphene transparent conductive film by roll-to-roll chemical vapor deposition and transfer process," *Applied Physics Letters*, vol. 102, no. 2, pp. –, 2013.
- [24] Q. Yu, L. A. Jauregui, W. Wu, R. Colby, J. Tian, Z. Su, H. Cao, Z. Liu, D. Pandey, D. Wei, T. F. Chung, P. Peng, N. P. Guisinger, E. A. Stach, J. Bao, S.-S. Pei, and Y. P. Chen, "Control and characterization of individual grains and grain boundaries in graphene grown by chemical vapour deposition," *Nat Mater*, vol. 10, pp. 443–449, 06 2011.
- [25] P. Y. Huang, C. S. Ruiz-Vargas, A. M. van der Zande, W. S. Whitney, M. P. Levenford, J. W. Kevek, S. Garg, J. S. Alden, C. J. Hustedt, Y. Zhu, J. Park, P. L. McEuen, and D. A. Muller, "Grains and grain boundaries in single-layer graphene atomic patchwork quilts," *Nature*, vol. 469, pp. 389–392, 01 2011.
- [26] H. Wang, G. Wang, P. Bao, S. Yang, W. Zhu, X. Xie, and W.-J. Zhang, "Controllable synthesis of submillimeter single-crystal monolayer graphene domains on copper foils by suppressing nucleation," *Journal of the American Chemical Society*, vol. 134, no. 8, pp. 3627–3630, 2012. PMID: 22324740.
- [27] Z. Yan, J. Lin, Z. Peng, Z. Sun, Y. Zhu, L. Li, C. Xiang, E. L. Samuel, C. Kittrell, and J. M. Tour, "Toward the synthesis of wafer-scale single-crystal graphene on copper foils," *ACS Nano*, vol. 6, no. 10, pp. 9110–9117, 2012. PMID: 22966902.
- [28] A. Mohsin, L. Liu, P. Liu, W. Deng, I. N. Ivanov, G. Li, O. E. Dyck, G. Duscher, J. R. Dunlap, K. Xiao, and G. Gu, "Synthesis of millimeter-size hexagon-shaped graphene single crystals on resolidified copper," *ACS Nano*, vol. 7, no. 10, pp. 8924–8931, 2013. PMID: 24004046.
- [29] B. Hu, H. Ago, Y. Ito, K. Kawahara, M. Tsuji, E. Magome, K. Sumitani, N. Mizuta, K. Ichi Ikeda, and S. Mizuno, "Epitaxial growth of large-area single-layer graphene over cu(111)/sapphire by atmospheric pressure cvd," *Carbon*, vol. 50, no. 1, pp. 57–65, 2012.
- [30] J.-H. Lee, E. K. Lee, W.-J. Joo, Y. Jang, B.-S. Kim, J. Y. Lim, S.-H. Choi, S. J. Ahn, J. R. Ahn, M.-H. Park, C.-W. Yang, B. L. Choi, S.-W. Hwang, and D. Whang, "Wafer-scale growth of single-crystal monolayer graphene on reusable hydrogen-terminated germanium," *Science*, vol. 344, no. 6181, pp. 286–289, 2014.

- [31] L. Gao, W. Ren, H. Xu, L. Jin, Z. Wang, T. Ma, L.-P. Ma, Z. Zhang, Q. Fu, L.-M. Peng, X. Bao, and H.-M. Cheng, "Repeated growth and bubbling transfer of graphene with millimetre-size single-crystal grains using platinum," *Nat Commun*, vol. 3, p. 699, 02 2012.
- [32] H. H. Kim, Y. Chung, E. Lee, S. K. Lee, and K. Cho, "Water-free transfer method for cvd-grown graphene and its application to flexible air-stable graphene transistors," *Advanced Materials*, vol. 26, no. 20, pp. 3213–3217, 2014.
- [33] W. Jung, D. Kim, M. Lee, S. Kim, J.-H. Kim, and C.-S. Han, "Ultraconformal contact transfer of monolayer graphene on metal to various substrates," *Advanced Materials*, vol. 26, no. 37, pp. 6394–6400, 2014.
- [34] X. Li, Y. Zhu, W. Cai, M. Borysiak, B. Han, D. Chen, R. D. Piner, L. Colombo, and R. S. Ruoff, "Transfer of large-area graphene films for high-performance transparent conductive electrodes," *Nano Letters*, vol. 9, no. 12, pp. 4359–4363, 2009. PMID: 19845330.
- [35] P. Moon and M. Koshino, "Optical absorption in twisted bilayer graphene," *Phys. Rev. B*, vol. 87, p. 205404, May 2013.
- [36] Z. Ni, L. Liu, Y. Wang, Z. Zheng, L.-J. Li, T. Yu, and Z. Shen, "G-band raman double resonance in twisted bilayer graphene: Evidence of band splitting and folding," *Phys. Rev. B*, vol. 80, p. 125404, Sep 2009.
- [37] K. Sato, R. Saito, C. Cong, T. Yu, and M. S. Dresselhaus, "Zone folding effect in raman g-band intensity of twisted bilayer graphene," *Phys. Rev. B*, vol. 86, p. 125414, Sep 2012.
- [38] K. Kim, S. Coh, L. Z. Tan, W. Regan, J. M. Yuk, E. Chatterjee, M. F. Crommie, M. L. Cohen, S. G. Louie, and A. Zettl, "Raman spectroscopy study of rotated double-layer graphene: Misorientation-angle dependence of electronic structure," *Phys. Rev. Lett.*, vol. 108, p. 246103, Jun 2012.
- [39] G. Li, A. Luican, J. M. B. Lopes dos Santos, A. H. Castro Neto, A. Reina, J. Kong, and E. Y. Andrei, "Observation of van hove singularities in twisted graphene layers," *Nat Phys*, vol. 6, pp. 109–113, 02 2010.
- [40] R. W. Havener, H. Zhuang, L. Brown, R. G. Hennig, and J. Park, "Angle-resolved raman imaging of interlayer rotations and interactions in twisted bilayer graphene," *Nano Letters*, vol. 12, no. 6, pp. 3162–3167, 2012. PMID: 22612855.

- [41] A. C. Ferrari, J. C. Meyer, V. Scardaci, C. Casiraghi, M. Lazzeri, F. Mauri, S. Piscanec, D. Jiang, K. S. Novoselov, S. Roth, and A. K. Geim, "Raman spectrum of graphene and graphene layers," *Phys. Rev. Lett.*, vol. 97, p. 187401, Oct 2006.
- [42] C.-R. Wang, W.-S. Lu, L. Hao, W.-L. Lee, T.-K. Lee, F. Lin, I.-C. Cheng, and J.-Z. Chen, "Enhanced thermoelectric power in dual-gated bilayer graphene," *Phys. Rev. Lett.*, vol. 107, p. 186602, Oct 2011.
- [43] J. Yan, Kim M.-H., E. A., S. B., J. S., M. M., F. S., and D. D., "Dual-gated bilayer graphene hot-electron bolometer," *Nat Nano*, vol. 7, pp. 472–478, 07 2012.
- [44] H. Yan, X. Li, B. Chandra, G. Tulevski, Y. Wu, M. Freitag, W. Zhu, P. Avouris, and F. Xia, "Tunable infrared plasmonic devices using graphene/insulator stacks," *Nat Nano*, vol. 7, pp. 330–334, 05 2012.
- [45] F. Xia, D. B. Farmer, Y.-m. Lin, and P. Avouris, "Graphene field-effect transistors with high on/off current ratio and large transport band gap at room temperature," *Nano Letters*, vol. 10, no. 2, pp. 715–718, 2010. PMID: 20092332.
- [46] J. A. Leon, E. S. Alves, D. C. Elias, J. C. Brant, T. C. Barbosa, L. M. Malard, M. A. Pimenta, G. M. Ribeiro, and F. Plentz, "Rapid fabrication of bilayer graphene devices using direct laser writing photolithography," *Journal of Vacuum Science and Technology B*, vol. 29, no. 2, pp. –, 2011.
- [47] V. Carozo, C. M. Almeida, E. H. M. Ferreira, L. G. Cançado, C. A. Achete, and A. Jorio, "Raman signature of graphene superlattices," *Nano Letters*, vol. 11, no. 11, pp. 4527–4534, 2011. PMID: 21978182.
- [48] D.-H. Chae, D. Zhang, X. Huang, and K. von Klitzing, "Electronic transport in two stacked graphene monolayers," *Nano Letters*, vol. 12, no. 8, pp. 3905–3908, 2012. PMID: 22823447.
- [49] G.-X. Ni, Y. Zheng, S. Bae, H. R. Kim, A. Pachoud, Y. S. Kim, C.-L. Tan, D. Im, J.-H. Ahn, B. H. Hong, and B. Özyilmaz, "Quasi periodic nanoripples in graphene grown by chemical vapor deposition and its impact on charge transport," *ACS Nano*, vol. 6, no. 2, pp. 1158–1164, 2012. PMID: 22251076.
- [50] C.-C. Chen, W. Bao, J. Theiss, C. Dames, C. N. Lau, and S. B. Cronin, "Raman spectroscopy of ripple formation in suspended graphene," *Nano Letters*, vol. 9, no. 12, pp. 4172–4176, 2009. PMID: 19807131.
- [51] W. Bao, K. Myhro, Z. Zhao, Z. Chen, W. Jang, L. Jing, F. Miao, H. Zhang, C. Dames, and C. N. Lau, "In situ observation of electrostatic and thermal manipulation of



- suspended graphene membranes," *Nano Letters*, vol. 12, no. 11, pp. 5470–5474, 2012. PMID: 23043470.
- [52] H. Vandeparre, M. Piñeirua, F. Brau, B. Roman, J. Bico, C. Gay, W. Bao, C. N. Lau, P. M. Reis, and P. Damman, "Wrinkling hierarchy in constrained thin sheets from suspended graphene to curtains," *Phys. Rev. Lett.*, vol. 106, p. 224301, Jun 2011.
- [53] N. Tombros, A. Veligura, J. Junesch, J. Jasper van den Berg, P. J. Zomer, M. Wojtaszek, I. J. Vera Marun, H. T. Jonkman, and B. J. van Wees, "Large yield production of high mobility freely suspended graphene electronic devices on a polydimethylglutarimide based organic polymer," *Journal of Applied Physics*, vol. 109, no. 9, pp. –, 2011.
- [54] W. Bao, F. Miao, Z. Chen, H. Zhang, W. Jang, C. Dames, and C. N. Lau, "Controlled ripple texturing of suspended graphene and ultrathin graphite membranes," *Nat Nano*, vol. 4, pp. 562–566, 09 2009.
- [55] Z. Wang and M. Devel, "Periodic ripples in suspended graphene," *Phys. Rev. B*, vol. 83, p. 125422, Mar 2011.
- [56] W. L. Wang, S. Bhandari, W. Yi, D. C. Bell, R. Westervelt, and E. Kaxiras, "Direct imaging of atomic-scale ripples in few-layer graphene," *Nano Letters*, vol. 12, no. 5, pp. 2278–2282, 2012. PMID: 22468740.
- [57] K. Bolotin, K. Sikes, Z. Jiang, M. Klima, G. Fudenberg, J. Hone, P. Kim, and H. Stormer, "Ultrahigh electron mobility in suspended graphene," *Solid State Communications*, vol. 146, no. 9-10, pp. 351 – 355, 2008.
- [58] S. Berciaud, S. Ryu, L. E. Brus, and T. F. Heinz, "Probing the intrinsic properties of exfoliated graphene: Raman spectroscopy of free-standing monolayers," *Nano Letters*, vol. 9, no. 1, pp. 346–352, 2009. PMID: 19099462.
- [59] J.-U. Lee, D. Yoon, and H. Cheong, "Estimation of young's modulus of graphene by raman spectroscopy," *Nano Letters*, vol. 12, no. 9, pp. 4444–4448, 2012. PMID: 22866776.
- [60] A. Reserbat-Plantey, D. Kalita, Z. Han, L. Ferlazzo, S. Autier-Laurent, K. Komatsu, C. Li, R. Weil, A. Ralko, L. Marty, S. Guéron, N. Bendiab, H. Bouchiat, and V. Bouchiat, "Strain superlattices and macroscale suspension of graphene induced by corrugated substrates," *Nano Letters*, vol. 14, no. 9, pp. 5044–5051, 2014. PMID: 25119792.
- [61] C. Lee, B.-J. Kim, F. Ren, S. J. Pearton, and J. Kim, "Large area suspended graphene on gan nanopillars," *Journal of Vacuum Science and Technology B*, vol. 29, no. 6, pp. –, 2011.

- [62] H. Tomori, A. Kanda, H. Goto, Y. Ootuka, K. Tsukagoshi, S. Moriyama, E. Watanabe, and D. Tsuya, "Introducing nonuniform strain to graphene using dielectric nanopillars," *Applied Physics Express*, vol. 4, no. 7, p. 075102, 2011.
- [63] I. Vlassiouk, S. Smirnov, I. Ivanov, P. F. Fulvio, S. Dai, H. Meyer, M. Chi, D. Hensley, P. Datskos, and N. V. Lavrik, "Electrical and thermal conductivity of low temperature cvd graphene: the effect of disorder," *Nanotechnology*, vol. 22, no. 27, p. 275716, 2011.
- [64] M. Yamamoto, "the princess and the pea" at the nanoscale: Wrinkling and delamination of graphene on nanoparticles," *Physical Review X*, vol. 2, no. 4, 2012.
- [65] D. Yoon, H. Moon, Y.-W. Son, J. S. Choi, B. H. Park, Y. H. Cha, Y. D. Kim, and H. Cheong, "Interference effect on raman spectrum of graphene on  $\text{SiO}_2/\text{Si}$ ," *Phys. Rev. B*, vol. 80, p. 125422, Sep 2009.
- [66] T. Mohiuddin, A. Lombardo, R. Nair, A. Bonetti, G. Savini, R. Jalil, N. Bonini, D. Basko, C. Galiotis, N. Marzari, K. Novoselov, A. Geim, and A. Ferrari, "Uniaxial strain in graphene by raman spectroscopy: g peak splitting, Grüneisen parameters, and sample orientation," *Phys. Rev. B*, vol. 79, p. 205433, May 2009.
- [67] V. N. Popov and P. Lambin, "Theoretical raman intensity of the g and 2d bands of strained graphene," *Carbon*, vol. 54, no. 0, pp. 86 – 93, 2013.
- [68] Das A., Pisana S., Chakraborty B., Piscanec S., S. K., W. V., N. S., K. R., G. K., F. C., and S. K., "Monitoring dopants by raman scattering in an electrochemically top-gated graphene transistor," *Nat Nano*, vol. 3, pp. 210–215, 04 2008.
- [69] Hergé, *Les 7 boules de cristal*. Casterman, 1948.
- [70] J. Yan, Y. Zhang, P. Kim, and A. Pinczuk, "Electric field effect tuning of electron-phonon coupling in graphene," *Phys. Rev. Lett.*, vol. 98, p. 166802, Apr 2007.
- [71] J. E. Lee, G. Ahn, J. Shim, Y. S. Lee, and S. Ryu, "Optical separation of mechanical strain from charge doping in graphene," *Nat Commun*, vol. 3, p. 1024, 08 2012.
- [72] X. Song, M. Oksanen, M. A. Sillanpää, H. G. Craighead, J. M. Parpia, and P. J. Hakonen, "Stamp transferred suspended graphene mechanical resonators for radio frequency electrical readout," *Nano Letters*, vol. 12, no. 1, pp. 198–202, 2012. PMID: 22141577.
- [73] F. Schedin, A. K. Geim, S. V. Morozov, E. W. Hill, P. Blake, M. I. Katsnelson, and K. S. Novoselov, "Detection of individual gas molecules adsorbed on graphene," *Nat Mater*, vol. 6, pp. 652–655, 09 2007.

- [74] W. Wu, Z. Liu, L. A. Jauregui, Q. Yu, R. Pillai, H. Cao, J. Bao, Y. P. Chen, and S.-S. Pei, "Wafer-scale synthesis of graphene by chemical vapor deposition and its application in hydrogen sensing," *Sensors and Actuators B: Chemical*, vol. 150, no. 1, pp. 296 – 300, 2010.
- [75] H. J. Yoon, D. H. Jun, J. H. Yang, Z. Zhou, S. S. Yang, and M. M.-C. Cheng, "Carbon dioxide gas sensor using a graphene sheet," *Sensors and Actuators B: Chemical*, vol. 157, no. 1, pp. 310 – 313, 2011.
- [76] G. Chen, T. M. Paronyan, and A. R. Harutyunyan, "Sub-ppt gas detection with pristine graphene," *Applied Physics Letters*, vol. 101, no. 5, pp. –, 2012.
- [77] C. P. Tan and H. G. Craighead, "Surface engineering and patterning using parylene for biological applications," *Materials*, vol. 3, no. 3, pp. 1803–1832, 2010.
- [78] S. Selvarasah, S. Chao, C.-L. Chen, S. Sridhar, A. Busnaina, A. Khademhosseini, and M. Dokmeci, "A reusable high aspect ratio parylene-c shadow mask technology for diverse micropatterning applications," *Sensors and Actuators A: Physical*, vol. 145-146, no. 0, pp. 306 – 315, 2008.
- [79] J. C. G. Vincent Bouchiat, "Highlights: Graphene in grenoble," p. 21, 2013.
- [80] S. S. Sabri, P. L. Lévesque, C. M. Aguirre, J. Guillemette, R. Martel, and T. Szkopek, "Graphene field effect transistors with parylene gate dielectric," *Applied Physics Letters*, vol. 95, no. 24, pp. –, 2009.
- [81] D. R., Y. F., MericI., LeeC., WangL., SorgenfreiS., WatanabeK., TaniguchiT., KimP., S. L., and HoneJ., "Boron nitride substrates for high-quality graphene electronics," *Nat Nano*, vol. 5, pp. 722–726, 10 2010.
- [82] L. Wang, I. Meric, P. Y. Huang, Q. Gao, Y. Gao, H. Tran, T. Taniguchi, K. Watanabe, L. M. Campos, D. A. Muller, J. Guo, P. Kim, J. Hone, K. L. Shepard, and C. R. Dean, "One-dimensional electrical contact to a two-dimensional material," *Science*, vol. 342, no. 6158, pp. 614–617, 2013.
- [83] S. J. Haigh, A. Gholinia, R. Jalil, S. Romani, L. Britnell, D. C. Elias, K. S. Novoselov, L. A. Ponomarenko, A. K. Geim, and R. Gorbachev, "Cross-sectional imaging of individual layers and buried interfaces of graphene-based heterostructures and superlattices," *Nat Mater*, vol. 11, pp. 764–767, 09 2012.
- [84] A. Mukhtarova, S. Valdueza-Felip, C. Durand, Q. Pan, L. Grenet, D. Peyrade, C. Bougerol, W. Chikhaoui, E. Monroy, and J. Eymery, "Ingan/gan multiple-quantum well heterostructures for solar cells grown by movpe: case studies," *physica status solidi (c)*, vol. 10, no. 3, pp. 350–354, 2013.

- [85] T.-H. Han, Y. Lee, M.-R. Choi, S.-H. Woo, S.-H. Bae, B. H. Hong, J.-H. Ahn, and T.-W. Lee, "Extremely efficient flexible organic light-emitting diodes with modified graphene anode," *Nat Photon*, vol. 6, pp. 105–110, 02 2012.
- [86] K. Kim, S.-H. Bae, C. T. Toh, H. Kim, J. H. Cho, D. Whang, T.-W. Lee, B. Özyilmaz, and J.-H. Ahn, "Ultrathin organic solar cells with graphene doped by ferroelectric polarization," *ACS Applied Materials & Interfaces*, vol. 6, no. 5, pp. 3299–3304, 2014. PMID: 24521002.
- [87] "Things you could do with graphene," *Nat Nano*, vol. 9, pp. 737–737, 10 2014.
- [88] J. Wu, L. Xie, Y. Li, H. Wang, Y. Ouyang, J. Guo, and H. Dai, "Controlled chlorine plasma reaction for noninvasive graphene doping," *Journal of the American Chemical Society*, vol. 133, no. 49, pp. 19668–19671, 2011. PMID: 22082226.
- [89] M. Jaiswal, C. H. Yi Xuan Lim, Q. Bao, C. T. Toh, K. P. Loh, and B. Özyilmaz, "Controlled hydrogenation of graphene sheets and nanoribbons," *ACS Nano*, vol. 5, no. 2, pp. 888–896, 2011. PMID: 21275382.
- [90] M. Wojtaszek, N. Tombros, A. Caretta, P. H. M. van Loosdrecht, and B. J. van Wees, "A road to hydrogenating graphene by a reactive ion etching plasma," *Journal of Applied Physics*, vol. 110, no. 6, pp. –, 2011.
- [91] Z. Luo, T. Yu, Z. Ni, S. Lim, H. Hu, J. Shang, L. Liu, Z. Shen, and J. Lin, "Electronic structures and structural evolution of hydrogenated graphene probed by raman spectroscopy," *The Journal of Physical Chemistry C*, vol. 115, no. 5, pp. 1422–1427, 2011.
- [92] W. H. Lee, J. W. Suk, H. Chou, J. Lee, Y. Hao, Y. Wu, R. Piner, D. Akinwande, K. S. Kim, and R. S. Ruoff, "Selective-area fluorination of graphene with fluoropolymer and laser irradiation," *Nano Letters*, vol. 12, no. 5, pp. 2374–2378, 2012. PMID: 22482878.
- [93] D. C. Elias, R. R. Nair, T. M. G. Mohiuddin, S. V. Morozov, P. Blake, M. P. Halsall, A. C. Ferrari, D. W. Boukhvalov, M. I. Katsnelson, A. K. Geim, and K. S. Novoselov, "Control of graphene's properties by reversible hydrogenation: Evidence for graphane," *Science*, vol. 323, no. 5914, pp. 610–613, 2009.
- [94] Z. Luo, T. Yu, K.-j. Kim, Z. Ni, Y. You, S. Lim, Z. Shen, S. Wang, and J. Lin, "Thickness-dependent reversible hydrogenation of graphene layers," *ACS Nano*, vol. 3, no. 7, pp. 1781–1788, 2009. PMID: 19492823.

- [95] R. R. Nair, W. Ren, R. Jalil, I. Riaz, V. G. Kravets, L. Britnell, P. Blake, F. Schedin, A. S. Mayorov, S. Yuan, M. I. Katsnelson, H.-M. Cheng, W. Strupinski, L. G. Bulusheva, A. V. Okotrub, I. V. Grigorieva, A. N. Grigorenko, K. S. Novoselov, and A. K. Geim, "Fluorographene: A two-dimensional counterpart of teflon," *Small*, vol. 6, no. 24, pp. 2877–2884, 2010.
- [96] F. Withers, M. Dubois, and A. Savchenko, "Electron properties of fluorinated single-layer graphene transistors," *Phys. Rev. B*, vol. 82, p. 073403, Aug 2010.
- [97] H. L. Poh, P. Šimek, Z. Sofer, and M. Pumera, "Halogenation of graphene with chlorine, bromine, or iodine by exfoliation in a halogen atmosphere," *Chemistry – A European Journal*, vol. 19, no. 8, pp. 2655–2662, 2013.
- [98] Z. Jin, T. P. McNicholas, C.-J. Shih, Q. H. Wang, G. L. C. Paulus, A. J. Hilmer, S. Shimizu, and M. S. Strano, "Click chemistry on solution-dispersed graphene and monolayer cvd graphene," *Chemistry of Materials*, vol. 23, no. 14, pp. 3362–3370, 2011.
- [99] E. Bekyarova, M. E. Itkis, P. Ramesh, C. Berger, M. Sprinkle, W. A. de Heer, and R. C. Haddon, "Chemical modification of epitaxial graphene: Spontaneous grafting of aryl groups," *Journal of the American Chemical Society*, vol. 131, no. 4, pp. 1336–1337, 2009. PMID: 19173656.
- [100] S. Niyogi, E. Bekyarova, M. E. Itkis, H. Zhang, K. Shepperd, J. Hicks, M. Sprinkle, C. Berger, C. N. Lau, W. A. deHeer, E. H. Conrad, and R. C. Haddon, "Spectroscopy of covalently functionalized graphene," *Nano Letters*, vol. 10, no. 10, pp. 4061–4066, 2010. PMID: 20738114.
- [101] R. Sharma, J. H. Baik, C. J. Perera, and M. S. Strano, "Anomalously large reactivity of single graphene layers and edges toward electron transfer chemistries," *Nano Letters*, vol. 10, no. 2, pp. 398–405, 2010. PMID: 20055430.
- [102] F. Sols, F. Guinea, and A. Neto, "Coulomb blockade in graphene nanoribbons," *Phys. Rev. Lett.*, vol. 99, p. 166803, Oct 2007.
- [103] J. Lahiri, Y. Lin, P. Bozkurt, I. I. Oleynik, and M. Batzill, "An extended defect in graphene as a metallic wire," *Nat Nano*, vol. 5, pp. 326–329, 05 2010.
- [104] A. Felten, B. S. Flavel, L. Britnell, A. Eckmann, P. Louette, J.-J. Pireaux, M. Hirtz, R. Krupke, and C. Casiraghi, "Single- and double-sided chemical functionalization of bilayer graphene," *Small*, vol. 9, no. 4, pp. 631–639, 2013.

- [105] D. C. Kim, D.-Y. Jeon, H.-J. Chung, Y. Woo, J. K. Shin, and S. Seo, "The structural and electrical evolution of graphene by oxygen plasma-induced disorder," *Nanotechnology*, vol. 20, no. 37, p. 375703, 2009.
- [106] A. Nourbakhsh, M. Cantoro, T. Vosch, G. Pourtois, F. Clemente, M. H. van der Veen, J. Hofkens, M. M. Heyns, S. D. Gendt, and B. F. Sels, "Bandgap opening in oxygen plasma-treated graphene," *Nanotechnology*, vol. 21, no. 43, p. 435203, 2010.
- [107] D. Teweldebrhan and A. A. Balandin, "Modification of graphene properties due to electron-beam irradiation," *Applied Physics Letters*, vol. 94, no. 1, pp. –, 2009.
- [108] G. Liu, D. Teweldebrhan, and A. Balandin, "Tuning of graphene properties via controlled exposure to electron beams," *Nanotechnology, IEEE Transactions on*, vol. 10, pp. 865–870, July 2011.
- [109] S. Zhou, i. m. c. Girit, A. Scholl, C. Jozwiak, D. Siegel, P. Yu, J. Robinson, F. Wang, A. Zettl, and A. Lanzara, "Instability of two-dimensional graphene: Breaking  $sp^2$  bonds with soft x rays," *Phys. Rev. B*, vol. 80, p. 121409, Sep 2009.
- [110] E. Martins Ferreira, M. Moutinho, F. Stavale, M. Lucchese, R. Capaz, C. Achete, and A. Jorio, "Evolution of the raman spectra from single-, few-, and many-layer graphene with increasing disorder," *Phys. Rev. B*, vol. 82, p. 125429, Sep 2010.
- [111] L. G. Cançado, A. Jorio, E. H. M. Ferreira, F. Stavale, C. A. Achete, R. B. Capaz, M. V. O. Moutinho, A. Lombardo, T. S. Kulmala, and A. C. Ferrari, "Quantifying defects in graphene via raman spectroscopy at different excitation energies," *Nano Letters*, vol. 11, no. 8, pp. 3190–3196, 2011. PMID: 21696186.
- [112] M. Lucchese, F. Stavale, E. M. Ferreira, C. Vilani, M. Moutinho, R. B. Capaz, C. Achete, and A. Jorio, "Quantifying ion-induced defects and raman relaxation length in graphene," *Carbon*, vol. 48, no. 5, pp. 1592 – 1597, 2010.
- [113] A. Jorio, E. H. M. Ferreira, M. V. O. Moutinho, F. Stavale, C. A. Achete, and R. B. Capaz, "Measuring disorder in graphene with the g and d bands," *physica status solidi (b)*, vol. 247, no. 11-12, pp. 2980–2982, 2010.
- [114] H. Wang, Q. Wang, Y. Cheng, K. Li, Y. Yao, Q. Zhang, C. Dong, P. Wang, U. Schwingenschlögl, W. Yang, and X. X. Zhang, "Doping monolayer graphene with single atom substitutions," *Nano Letters*, vol. 12, no. 1, pp. 141–144, 2012. PMID: 22136503.
- [115] J. J. Lopez, F. Greer, and J. R. Greer, "Enhanced resistance of single-layer graphene to ion bombardment," *Journal of Applied Physics*, vol. 107, no. 10, pp. –, 2010.

- [116] F. Tuinstra and J. L. Koenig, "Raman spectrum of graphite," *The Journal of Chemical Physics*, vol. 53, no. 3, pp. 1126–1130, 1970.
- [117] R. Nemanich and S. Solin, "Observation of an anomalously sharp feature in the 2nd order raman spectrum of graphite," *Solid State Communications*, vol. 23, no. 7, pp. 417 – 420, 1977.
- [118] R. Tsu, J. G. H., and I. H. C., "Observation of splitting of the  $\{E_{2g}\}$  mode and two-phonon spectrum in graphites," *Solid State Communications*, vol. 27, no. 5, pp. 507 – 510, 1978.
- [119] R. Nemanich and S. Solin, "First- and second-order raman scattering from finite-size crystals of graphite," *Phys. Rev. B*, vol. 20, pp. 392–401, Jul 1979.
- [120] P. Lespade, A. Marchand, M. Couzi, and F. Cruege, "Caracterisation de materiaux carbonés par microspectrometrie raman," *Carbon*, vol. 22, no. 4, pp. 375 – 385, 1984.
- [121] P. Lespade, R. Al-Jishi, and M. Dresselhaus, "Model for raman scattering from incompletely graphitized carbons," *Carbon*, vol. 20, no. 5, pp. 427 – 431, 1982.
- [122] R. Vidano, D. Fischbach, L. Willis, and T. Loehr, "Observation of raman band shifting with excitation wavelength for carbons and graphites," *Solid State Communications*, vol. 39, no. 2, pp. 341 – 344, 1981.
- [123] L. G. Cançado, K. Takai, T. Enoki, M. Endo, Y. A. Kim, H. Mizusaki, A. Jorio, L. N. Coelho, R. Magalhães-Paniago, and M. A. Pimenta, "General equation for the determination of the crystallite size  $l_a$  of nanographite by raman spectroscopy," *Applied Physics Letters*, vol. 88, no. 16, pp. –, 2006.
- [124] K. Sato, R. Saito, Y. Oyama, J. Jiang, L. Canado, M. Pimenta, A. Jorio, G. Samsonidze, G. Dresselhaus, and M. Dresselhaus, "D-band raman intensity of graphitic materials as a function of laser energy and crystallite size," *Chemical Physics Letters*, vol. 427, no. 1-3, pp. 117 – 121, 2006.
- [125] A. Ferrari and J. Robertson, "Interpretation of raman spectra of disordered and amorphous carbon," *Phys. Rev. B*, vol. 61, pp. 14095–14107, May 2000.
- [126] A. Ferrari and J. Robertson, "Resonant raman spectroscopy of disordered, amorphous, and diamondlike carbon," *Phys. Rev. B*, vol. 64, p. 075414, Jul 2001.
- [127] C. Casiraghi, A. Ferrari, and J. Robertson, "Raman spectroscopy of hydrogenated amorphous carbons," *Phys. Rev. B*, vol. 72, p. 085401, Aug 2005.

- [128] M. Dresselhaus, G. Dresselhaus, R. Saito, and A. Jorio, "Raman spectroscopy of carbon nanotubes," *Physics Reports*, vol. 409, no. 2, pp. 47 – 99, 2005.
- [129] S. Reich, C. Thomsen, and J. Maultzsch, *Carbon Nanotubes: Basic Concepts and Physical Properties*. Wiley-VCH, 2004.
- [130] A. Jorio, M. Dresselhaus, and G. Dresselhaus, *Carbon Nanotubes: Advanced Topics in the Synthesis, Structure, Properties and Applications*. Springer, 2008.
- [131] A. Eckmann, A. Felten, A. Mishchenko, L. Britnell, R. Krupke, K. S. Novoselov, and C. Casiraghi, "Probing the nature of defects in graphene by raman spectroscopy," *Nano Letters*, vol. 12, no. 8, pp. 3925–3930, 2012. PMID: 22764888.
- [132] A. Eckmann, A. Felten, I. Verzhbitskiy, R. Davey, and C. Casiraghi, "Raman study on defective graphene: Effect of the excitation energy, type, and amount of defects," *Phys. Rev. B*, vol. 88, p. 035426, Jul 2013.
- [133] K. N. Kudin, B. Ozbas, H. C. Schniepp, R. K. Prud'homme, I. A. Aksay, and R. Car, "Raman spectra of graphite oxide and functionalized graphene sheets," *Nano Letters*, vol. 8, no. 1, pp. 36–41, 2008. PMID: 18154315.
- [134] C. Wang, Y. Liu, L. Lan, and H. Tan, "Graphene wrinkling: formation, evolution and collapse," *Nanoscale*, vol. 5, pp. 4454–4461, 2013.
- [135] L. Cançado, A. Jorio, and M. Pimenta, "Measuring the absolute raman cross section of nanographites as a function of laser energy and crystallite size," *Phys. Rev. B*, vol. 76, p. 064304, Aug 2007.
- [136] C. Pardanaud, C. Martin, and P. Roubin, "Multiwavelength raman spectroscopy analysis of a large sampling of disordered carbons extracted from the tore supra tokamak," *Vibrational Spectroscopy*, vol. 70, no. 0, pp. 187 – 192, 2014.
- [137] P. Tan, "Temperature-dependent raman spectra and anomalous raman phenomenon of highly oriented pyrolytic graphite," *Physical Review B*, vol. 58, no. 9, pp. 5435–5439, 1998.
- [138] P. Tan, C. Hu, J. Dong, W. Shen, and B. Zhang, "Polarization properties, high-order raman spectra, and frequency asymmetry between stokes and anti-stokes scattering of raman modes in a graphite whisker," *Phys. Rev. B*, vol. 64, p. 214301, Nov 2001.
- [139] D. Mafra, G. Samsonidze, L. Malard, D. Elias, J. Brant, F. Plentz, E. Alves, and M. Pimenta, "Determination of  $\Gamma$  and  $\Lambda$  phonon dispersion relations of graphene



- near the dirac point by double resonance raman scattering," *Phys. Rev. B*, vol. 76, p. 233407, Dec 2007.
- [140] P. May, M. Lazzeri, P. Venezuela, F. Herziger, G. Callsen, J. Reparaz, A. Hoffmann, F. Mauri, and J. Maultzsch, "Signature of the two-dimensional phonon dispersion in graphene probed by double-resonant raman scattering," *Phys. Rev. B*, vol. 87, p. 075402, Feb 2013.
- [141] R. Narula and S. Reich, "Probing lo phonons of graphene under tension via the 2d' raman mode," *Phys. Rev. B*, vol. 87, p. 115424, Mar 2013.
- [142] C. Thomsen and S. Reich, "Double resonant raman scattering in graphite," *Phys. Rev. Lett.*, vol. 85, pp. 5214–5217, Dec 2000.
- [143] J. Zabel, R. R. Nair, A. Ott, T. Georgiou, A. K. Geim, K. S. Novoselov, and C. Casiraghi, "Raman spectroscopy of graphene and bilayer under biaxial strain: Bubbles and balloons," *Nano Letters*, vol. 12, no. 2, pp. 617–621, 2012. PMID: 22149458.
- [144] F. Ding, H. Ji, Y. Chen, A. Herklotz, K. Dörr, Y. Mei, A. Rastelli, and O. G. Schmidt, "Stretchable graphene: A close look at fundamental parameters through biaxial straining," *Nano Letters*, vol. 10, no. 9, pp. 3453–3458, 2010. PMID: 20695450.
- [145] B. Elman, M. Shayegan, M. Dresselhaus, H. Mazurek, and G. Dresselhaus, "Structural characterization of ion-implanted graphite," *Phys. Rev. B*, vol. 25, pp. 4142–4156, Mar 1982.
- [146] B. Elman, M. Dresselhaus, G. Dresselhaus, E. Maby, and H. Mazurek, "Raman scattering from ion-implanted graphite," *Phys. Rev. B*, vol. 24, pp. 1027–1034, Jul 1981.
- [147] J. H. Chen, C. Jang, S. Adam, M. S. Fuhrer, E. D. Williams, and M. Ishigami, "Charged-impurity scattering in graphene," *Nat Phys*, vol. 4, pp. 377–381, 05 2008.
- [148] N. Petrone, C. R. Dean, I. Meric, A. M. van der Zande, P. Y. Huang, L. Wang, D. Muller, K. L. Shepard, and J. Hone, "Chemical vapor deposition-derived graphene with electrical performance of exfoliated graphene," *Nano Letters*, vol. 12, no. 6, pp. 2751–2756, 2012. PMID: 22582828.
- [149] D. A. Siegel, W. Regan, A. V. Fedorov, A. Zettl, and A. Lanzara, "Charge-carrier screening in single-layer graphene," *Phys. Rev. Lett.*, vol. 110, p. 146802, Apr 2013.
- [150] K. T. Chan, J. B. Neaton, and M. L. Cohen, "First-principles study of metal adatom adsorption on graphene," *Phys. Rev. B*, vol. 77, p. 235430, Jun 2008.

- [151] P. Wei, N. Liu, H. R. Lee, E. Adijanto, L. Ci, B. D. Naab, J. Q. Zhong, J. Park, W. Chen, Y. Cui, and Z. Bao, "Tuning the dirac point in cvd-grown graphene through solution processed n-type doping with 2-(2-methoxyphenyl)-1,3-dimethyl-2,3-dihydro-1h-benzoimidazole," *Nano Letters*, vol. 13, no. 5, pp. 1890–1897, 2013. PMID: 23537351.
- [152] M. Lopes, A. Candini, M. Urdampilleta, A. Reserbat-Plantey, V. Bellini, S. Klyatskaya, L. Marty, M. Ruben, M. Affronte, W. Wernsdorfer, and N. Bendiab, "Surface-enhanced raman signal for terbium single-molecule magnets grafted on graphene," *ACS Nano*, vol. 4, no. 12, pp. 7531–7537, 2010. PMID: 21067149.
- [153] P. Venezuela, M. Lazzeri, and F. Mauri, "Theory of double-resonant raman spectra in graphene: Intensity and line shape of defect-induced and two-phonon bands," *Phys. Rev. B*, vol. 84, p. 035433, Jul 2011.
- [154] H. Zhou, W. J. Yu, L. Liu, R. Cheng, Y. Chen, X. Huang, Y. Liu, Y. Wang, Y. Huang, and X. Duan, "Chemical vapour deposition growth of large single crystals of mono-layer and bilayer graphene," *Nat Commun*, vol. 4, 06 2013.
- [155] J. D. Jones, P. A. Ecton, Y. Mo, and J. M. Perez, "Comment on "modification of graphene properties due to electron-beam irradiation" [appl. phys. lett.94, 013101 (2009)]," *Applied Physics Letters*, vol. 95, no. 24, pp. –, 2009.
- [156] J. C. Meyer, F. Eder, S. Kurasch, V. Skakalova, J. Kotakoski, H. J. Park, S. Roth, A. Chuvilin, S. Eychusen, G. Benner, A. V. Krasheninnikov, and U. Kaiser, "Accurate measurement of electron beam induced displacement cross sections for single-layer graphene," *Phys. Rev. Lett.*, vol. 108, p. 196102, May 2012.
- [157] L. Tao, C. Qiu, F. Yu, H. Yang, M. Chen, G. Wang, and L. Sun, "Modification on single-layer graphene induced by low-energy electron-beam irradiation," *The Journal of Physical Chemistry C*, vol. 117, no. 19, pp. 10079–10085, 2013.
- [158] I. Pocsik, M. Hundhausen, M. Koos, and L. Ley, "Origin of the d peak in the raman spectrum of microcrystalline graphite," *Journal of Non-Crystalline Solids*, vol. 227–230, Part 2, no. 0, pp. 1083 – 1086, 1998.
- [159] J. Maultzsch, S. Reich, and C. Thomsen, "Double-resonant raman scattering in graphite: Interference effects, selection rules, and phonon dispersion," *Phys. Rev. B*, vol. 70, p. 155403, Oct 2004.
- [160] D. T. Schwartz, "Raman spectroscopy: Introductory tutorial,"

- [161] A. H. Castro Neto, F. Guinea, N. M. R. Peres, K. S. Novoselov, and A. K. Geim, "The electronic properties of graphene," *Rev. Mod. Phys.*, vol. 81, pp. 109–162, Jan 2009.
- [162] M. Lazzeri, C. Attaccalite, L. Wirtz, and F. Mauri, "Impact of the electron-electron correlation on phonon dispersion: Failure of lda and gga dft functionals in graphene and graphite," *Phys. Rev. B*, vol. 78, p. 081406, Aug 2008.
- [163] D. M. Basko, "Calculation of the raman g peak intensity in monolayer graphene: role of ward identities," *New Journal of Physics*, vol. 11, no. 9, p. 095011, 2009.
- [164] P. Venezuela, M. Lazzeri, and F. Mauri, "Theory of double-resonant raman spectra in graphene: Intensity and line shape of defect-induced and two-phonon bands," *Phys. Rev. B*, vol. 84, p. 035433, Jul 2011.
- [165] R. Beams, L. G. Cançado, and L. Novotny, "Raman characterization of defects and dopants in graphene," *Journal of Physics: Condensed Matter*, vol. 27, no. 8, p. 083002, 2015.

## ACKNOWLEDGEMENTS

---

The journey towards my PhD in Grenoble started from my M.Tech course in India where I got the opportunity to study in dual degree course from University of Delhi and University of Joseph Fourier. During the Masters I was fortunate to work in a research lab during my internship which ignited my will to make a thesis. Here I would like to thank the people involved during this journey until the end of the thesis.

The complexity of starting a dual degree course would not be possible without the hard of people from France and India. Though I don't know many involved in this process, I would like to thank Dr. S Annapoorni, Dr. Vinay Gupta from University of Delhi and Dr. Phillippe Peyla from UJF who put in a lot of effort for this programme to materialise. It was during this course that I was introduced to Dr. Vincent Bouchiat in the molecular electronics class. After some memorable events, he offered me do my thesis under his tutelage during which I met Dr. Nedjma Bendiab and Dr. Laëtitia Marty.

Nedjma has been very patient with me in showing different directions to understand the data of Raman spectroscopy and corrections for the chapters. Most of the experiments would not have been possible without noble directions shown by Laëtitia. Some of the experiments went on till mid-night while others required innovation like the parylene transparent mask. Here I would like to thank Antoine Reserbat-plantey for his help in Raman spectroscopy during the initial days of my PhD. Later, it was the ever-patient Vitto (Zheng Han) who taught me to use CVD machine and transfer of graphene. The transfer of know-how from these two gentle men helped me immensely for experiments. Towards the end of the thesis, Alexandre Artaud helped a lot of with analysis and theory of Raman spectroscopy.

I would also to thank people from the Nanofab team, Richard Haettel, Jean- Francois Motte, Valerie Reita , Emmanuel Andre, David Barral who have been very helpful during various stages of experimentation. I have been also lucky to have been to work with different collaborators: Christophe Durand, Anna Mukhtarova, Gardenia Pinheiro, Gilles Cunge, Alfonso San-Miguel, Abraao Torres, Joel Eymery, H el ene Bouchiat, Sophie Gu eron, Michele Lazzeri, Denis Basco, Hanako Okuno.

There are also lot of people who contributed in different aspects of my life. My deepest appreciation to Cornelia Schwarz, Fabien Jean, Yani Chen, Farida Veliev, Franck Dahlem, Shelender Kumar, Edgar Bonet, Oksana Gaier, Sergio Vlaic, John Landers, Liu Jinxing, Hadi A-T, Mitsuki Ito, Olivier Duigou, Adrien Allain, Amina Kimouche, Dr. De-Traversay, Hanno Flentje, Tobius Bautze, Sven Rohr, Rudeesun Songmuang, Sayanti Sammadar, Oriane Avezou.